ISSN 2523-6865

Volume 9, Issue 20 — e20250920 January — December — 2025

Journal Computational Simulation

ECORFAN®

Journal Computational Simulation, Volume 9, Issue 20: e20250920 January – December 2025, is a Continuous publication – Journal edited by ECORFAN-Taiwan. Taiwan, Taipei. YongHe district, Zhong Xin, Street 69. Postcode: 23445. WEB: www.ecorfan.org/taiwan, revista@ecorfan.org. Editor in Chief: Quintanilla - Cóndor, Cerapio. PhD. ISSN: 2523-6865. Responsible for the last update of this issue of the ECORFAN Informatics Unit. Escamilla-Bouchán, Imelda, Luna-Soto, Vladimir, updated December 30, 2025.

Journal Computational Simulation

Definition of Journal

Scientific Objectives

Support the international scientific community in its written production Science, Technology and Innovation in the Field of Engineering and Technology, in Subdisciplines of telemetry, diffuse interval, electrical stimulation, diffuse controller, mobile application, communications network, web platform, production control, computer technology, computer electronics, control devices, programming languages and automated production systems.

ECORFAN-Mexico, S.C. is a Scientific and Technological Company in contribution to the Human Resource training focused on the continuity in the critical analysis of International Research and is attached to SECITHI-RENIECYT number 1702902, its commitment is to disseminate research and contributions of the International Scientific Community, academic institutions, agencies and entities of the public and private sectors and contribute to the linking of researchers who carry out scientific activities, technological developments and training of specialized human resources with governments, companies and social organizations.

Encourage the interlocution of the International Scientific Community with other Study Centers in Mexico and abroad and promote a wide incorporation of academics, specialists and researchers to the publication in Science Structures of Autonomous Universities - State Public Universities - Federal IES - Polytechnic Universities - Technological Universities - Federal Technological Institutes - Normal Schools - Decentralized Technological Institutes - Intercultural Universities - S & T Councils - SECITHI Research Centers.

Scope, Coverage and Audience

Journal Computational Simulation is a Journal edited by ECORFAN-Mexico S.C in its Holding with repository in Taiwan, is a scientific publication arbitrated and indexed with semester periods. It supports a wide range of contents that are evaluated by academic peers by the Double-Blind method, around subjects related to the theory and practice of telemetry, diffuse interval, electrical stimulation, diffuse controller, mobile application, communications network, web platform, production control, computer technology, computer electronics, control devices, programming languages and automated production systems with diverse approaches and perspectives, that contribute to the diffusion of the development of Science Technology and Innovation that allow the arguments related to the decision making and influence in the formulation of international policies in the Field of Engineering and Technology. The editorial horizon of ECORFAN-Mexico® extends beyond the academy and integrates other segments of research and analysis outside the scope, as long as they meet the requirements of rigorous argumentative and scientific, as well as addressing issues of general and current interest of the International Scientific Society.

Editorial Board

Arbitration Committee

Loaeza - Valerio, Roberto. PhD
Tecnológico Nacional de México Campus Uruapan

Perez - Ornelas, Felicitas. PhD
Universidad Autónoma de Baja California • 0000-0001-7117-2318

Antolino - Hernandez, Anastacio. PhD
Instituto Tecnológico de Morelia • 0000-0001-6150-2934 • 210830

Hernández - Morales, Daniel Eduardo. PhD
Tecnológico Nacional de México - Instituto Tecnológico de Tijuana • 0000-0003-2563-9129 • 267339

Ayala - Figueroa, Rafael. PhD
Instituto Tecnologico Nacional de Mexico /Mexicali • LCD-3310-2024 • 0000-0001-9988-1626

Gaxiola - Pacheco, Carelia Guadalupe. PhD
Universidad Autónoma de Baja California • 0000-0001-9408-8784 • 228485

Gonzalez - Berrelleza, Claudia Ibeth. PhD
Instituto Tecnológico de Tijuana • 0000-0003-3312-3376 • 44524

Castro - Rodríguez, Juan Ramón. PhD
Universidad Autónoma de Baja California • K-9962-2014 • 0000-0003-2523-0681 • 75506

Arroyo - Díaz, Salvador Antonio. PhD
Universidad Politécnica de Puebla • 0000-0003-4970-5450 • 104369

Morales - Carbajal, Carlos. PhD
Universidad Politécnica de Baja California • LFS-7503-2024 • 0000-0001-6837-2482 • 203389

Rodríguez - Díaz, Antonio. PhD
Universidad Autónoma de Baja California • KVX-8229-2024 • 0000-0003-3920-6834 • 32876

Assignment of Rights

The sending of an Article to Journal Computational Simulation emanates the commitment of the author not to submit it simultaneously to the consideration of other series publications for it must complement the Originality Format for its Article.

The authors sign the Authorization Format for their Article to be disseminated by means that ECORFAN-Mexico, S.C. In its Holding Taiwan considers pertinent for disclosure and diffusion of its Article its Rights of Work.

Declaration of Authorship

Indicate the Name of Author and Coauthors at most in the participation of the Article and indicate in extensive the Institutional Affiliation indicating the Department.

Identify the Name of Author and Coauthors at most with the CVU Scholarship Number-PNPC or SNI-SECITHI- Indicating the Researcher Level and their Google Scholar Profile to verify their Citation Level and H index.

Identify the Name of Author and Coauthors at most in the Science and Technology Profiles widely accepted by the International Scientific Community ORC ID - Researcher ID Thomson - arXiv Author ID - PubMed Author ID - Open ID respectively.

Indicate the contact for correspondence to the Author (Mail and Telephone) and indicate the Researcher who contributes as the first Author of the Article.

Plagiarism Detection

All Articles will be tested by plagiarism software PLAGSCAN if a plagiarism level is detected Positive will not be sent to arbitration and will be rescinded of the reception of the Article notifying the Authors responsible, claiming that academic plagiarism is criminalized in the Penal Code.

Arbitration Process

All Articles will be evaluated by academic peers by the Double-Blind method, the Arbitration Approval is a requirement for the Editorial Board to make a final decision that will be final in all cases. MARVID® is a derivative brand of ECORFAN® specialized in providing the expert evaluators all of them with Doctorate degree and distinction of International Researchers in the respective Councils of Science and Technology the counterpart of SECITHI for the chapters of America-Europe-Asia- Africa and Oceania. The identification of the authorship should only appear on a first removable page, in order to ensure that the Arbitration process is anonymous and covers the following stages: Identification of the Research Journal with its author occupation rate - Identification of Authors and Coauthors - Detection of plagiarism PLAGSCAN - Review of Formats of Authorization and Originality-Allocation to the Editorial Board-Allocation of the pair of Expert Arbitrators-Notification of Arbitration -Declaration of observations to the Author-Verification of Article Modified for Editing-Publication.

Instructions for Scientific, Technological and Innovation Publication

Knowledge Area

The works must be unpublished and refer to topics of telemetry, diffuse interval, electrical stimulation, diffuse controller, mobile application, communications network, web platform, production control, computer technology, computer electronics, control devices, programming languages and automated production systems and other topics related to Engineering and Technology.

Presentation of Content

The first article presents, *Mathematical and numeric analysis of a 4-DOF manipulator kinematics* by García-Trinidad, Enrique, Arcos-Hernández, Emmanuel, Torres-Valle, José and Hernández-Borja, Carlos, with adscription in the Universidad Tecnológica Fidel Velázquez, following article presents *Dynamic control analysis by simulation of the main components of a Hall Effect thruster* by Aburto–Policarpo Gethsi, Castillo-Sánchez Martín and López-Cárdenas Rodrigo, with adscription in the Instituto Politécnico Nacional, following article presents *Parametric analysis of dynamic wave-seabed interaction* by Peza-Ortiz, Edebaldo, Arcos-Hernández, Emmanuel, García-Trinidad, Enrique and Torres-Valle, José, with adscription in the Universidad Tecnológica Fidel Velázquez, following article presents *Nodal analysis of transtibial prostheses using the finite element method with Matlab* by Cortez-Solis, Reynaldo, Fuentes-Castañeda, Pilar, Betanzos-Castillo, Francisco, Jaramillo-Rodriguez, Eduardo, with adscription in the Tecnológico Nacional de México – TES Valle de Bravo.

Content

Journal Computational Simulation 9[20]1-11: e10920111
Article

Mathematical and numeric analysis of a 4-DOF manipulator kinematics

Análisis matemático y numérico de la cinemática de un manipulador de 4 GDL

García-Trinidad, Enrique*[a], Arcos-Hernández, Emmanuel[b], Torres-Valle, José[c] and Hernández-Borja, Carlos[d]

[a] Universidad Tecnológica Fidel Velázquez • 9353-2024 • 0000-0003-2875-0500 • 271440
[b] Universidad Tecnológica Fidel Velázquez • 1933-2025 • 0000-0002-3404-1375 • 349835
[c] Universidad Tecnológica Fidel Velázquez • 6499-2025 • 0000-0001-8258-9418 • 626539
[d] Universidad Tecnológica Fidel Velázquez • 1898-2025 • 0000-0002-8138-9016

SECIHTI classification:

Area: Engineering
Field: Engineering
Discipline: Electronic Engineering
Subdiscipline: Robotics

https://doi.org/10.35429/JCS.2025.9.20.1.11
Article History:
Received: June 30, 2025
Accepted: December 10, 2025

* ✉ [enrique.garcia@utfv.edu.mx]

Abstract

This paper analyzes the kinematics of a 4-DOF robotic manipulator. The Denavit-Hartenberg formulation for geometric modeling, which simplifies the description of the links, is detailed. Direct kinematics maps the joint variables to the end-effector pose in a unique way. Inverse kinematics, more complex, determines the joint angles for a desired pose, facing multiple solutions and nonlinear equations. Analytical (geometric and algebraic) and numerical (Newton-Raphson, Levenberg-Marquardt) methods are explored. Practical implications include simulation and visualization in Python's Robotics Toolbox.

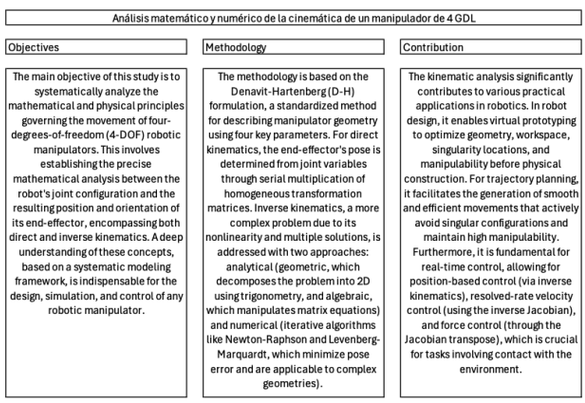

Robotics, Kinematics, Simulation

Resumen

Este artículo analiza la cinemática de un manipulador robótico de 4 GDL. Se detalla la formulación de Denavit-Hartenberg para el modelado geométrico, que simplifica la descripción de los eslabones. La cinemática directa mapea las variables articulares a la pose del efector final de forma única. La cinemática inversa, más compleja, determina los ángulos articulares para una pose deseada, enfrentando múltiples soluciones y ecuaciones no lineales. Se exploran métodos analíticos (geométricos y algebraicos) y numéricos (Newton-Raphson, Levenberg-Marquardt). Las implicaciones prácticas incluyen la simulación y visualización en la Robotics Toolbox de Python.

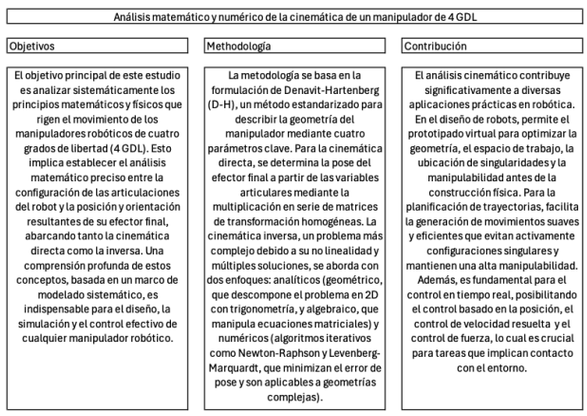

Robótica, Cinemática, Simulación

Area: Development of strategic leading-edge technologies and open innovation for social transformation

Citation: García-Trinidad, Enrique, Arcos-Hernández, Emmanuel, Torres-Valle, José and Hernández-Borja, Carlos. [2025]. Mathematical and numeric analysis of a 4-DOF manipulator kinematics. Journal Computational Simulation. 9[20] 1-11: e10920111.

Introducción

The study of a robot manipulator's movement, or kinematics, is the scientific foundation upon which the entire analysis, control, and application of robotic manipulators are built. Kinematics establishes the precise mathematical analysis between the robot's joint configuration and the resulting position and orientation of its end-effector (Manseur & Doty, 1988). This analysis is fundamentally divided into two problems: direct kinematics and inverse kinematics. This deep understanding, based on a systematic modeling framework, is indispensable for the design, simulation, and control of any robotic manipulator (Malik, Lischuk, Henderson, & Prazenica, 2022).

In general, a robotic manipulator can be described in two distinct but interconnected domains: the joint space and the Cartesian space. The selection of which domain to use depends on the task at hand, whether it is the direct control of the actuators or the interaction of the manipulator's end-effector with the physical world. The joint space is the n-dimensional space defined by the vector of all joint variables, denoted as q. For a 4-degree-of-freedom (DOF) manipulator with four rotational joints, the vector is $q = [q_0, q_1, q_2, q_3]^T$. Each element of this vector represents a single, directly controllable degree of freedom of the robot, such as the angle of a motor shaft. Control systems fundamentally operate in the joint space, as they send commands to the individual joint actuators.

The Cartesian space, also known as the operational space, is the space in which the robot's end-effector performs its tasks. It is typically a six-dimensional space that describes the pose of the end-effector, with three dimensions for its position (P_x, P_y, P_z) and three dimensions for its orientation, which can be represented by Euler angles (ϕ, θ, ψ). Robot programming and task planning are almost always performed in the Cartesian space because tasks like picking up an object, welding, or following a trajectory are naturally defined by the desired movement of the end-effector in the physical world (Guida, De Simone, Dasic, & Guida, 2019). The core of kinematic analysis is to define the mathematical mapping between these two spaces.

Direct and Inverse Kinematics

Direct Kinematics (DK) is the process of determining the Cartesian position and orientation (pose) of the end-effector from a known set of joint variables. This can be expressed as a function f, shown in Equation 1.

$$X = f(q) \quad [1]$$

where X is the end-effector pose vector $[P_x, P_y, P_z, \phi, \theta, \psi]^T$ and q is the vector of joint variables. The direct kinematics problem is considered straightforward because for any given set of joint angles, there is one and only one resulting pose of the end-effector. The mapping is unique and can be calculated directly through a series of matrix multiplications, as detailed later.

Inverse Kinematics (IK) is the reverse and significantly more challenging problem, as it determines the required set of joint variables q that places the end-effector at a desired Cartesian pose X. This inverse mapping is expressed in Equation 2 as:

$$q = f^{-1}(X) \quad [2]$$

The complexity of inverse kinematics arises from several factors (Bao, Liu, & Zhao, 2017), including the non-existence of solutions, since if the desired pose X is outside the manipulator's physical reach, no solution exists. Similarly, for a single desired end-effector pose within the workspace, there can be multiple, and sometimes even infinite, solutions. For example, a simple planar arm can often reach a point with an elbow-up or elbow-down posture (Mohammed & Sunar, 2015).

The control system must have a logical basis for selecting one solution from the set of possibilities. Another factor to consider is that the equations governing inverse kinematics are highly non-linear and trigonometric, making them difficult to solve.

Although analytical, or closed-form, solutions are preferable for their speed and completeness, they only exist for manipulators with specific geometric structures. For more complex robots, iterative numerical methods must be employed.

ISSN: 2523-6865
RENIECYT-SECIHTI: 1702902

García-Trinidad, Enrique, Arcos-Hernández, Emmanuel, Torres-Valle, José and Hernández-Borja, Carlos. [2025]. Mathematical and numeric analysis of a 4-DOF manipulator kinematics. Journal Computational Simulation. 9[20] 1-11: e10920111.
https://doi.org/10.35429/JCS.2025.9.20.1.1.11

Denavit-Hartenberg Formulation

To perform kinematic analysis, a consistent method for describing the manipulator's geometry is required. The Denavit-Hartenberg (D-H) formulation is the most widely adopted method for systematically assigning coordinate systems to the links of a manipulator. Its main advantage is that it describes the spatial relationship between consecutive links using a minimal set of four parameters, which greatly simplifies mathematical modeling (Corke, 2007).

The power of the D-H convention lies in its clever mathematical simplification. A general transformation describing the relative pose of one coordinate system with respect to another in 3D space requires six parameters, but D-H reduces this to just four by imposing strict rules on how the coordinate systems are placed. Specifically, the convention requires that the x_i axis of a coordinate system must be perpendicular to and intersect the z_{i-1} axis of the previous system. These two geometric constraints effectively eliminate two degrees of freedom from the general transformation, leaving exactly four.

The D-H procedure involves rigidly attaching a coordinate frame $\{i\}$ to each link i of the manipulator, from the fixed base (link 0) to the end-effector (link n). The procedure is as follows:

1. Identify the joint axes: The axis of actuation (rotation for a revolute joint, translation for a prismatic joint) for joint i is defined as the z_{i-1}axis. The axes are numbered $z_0, z_1, \dots, z_{n-1}$.

2. Establish the base coordinate system $\{0\}$: The origin is placed anywhere on the $z_0$axis. The x_0 and y_0 axes are chosen to form a right-handed coordinate system. This system is the global or inertial reference frame.

3. Iteratively assign frames $\{1\}$ to $\{n-1\}$: For each link i, the frame $\{i\}$ is established based on its relationship with frame $\{i-1\}$:

   The origin O_i is located at the intersection of the z_i y la normal común que se extiende desde el eje z_{i-1} axis. The common normal is the unique line segment that is mutually perpendicular to both z_i and z_{i-1}.

   The x_i axis is directed along this common normal, pointing from the z_{i-1} axis toward the z_i axis.

   The y_i axis is defined by the right-hand rule to complete the coordinate system ($y_i = z_i \times x_i$).

   If thez_{i-1} and z_i axes intersect, the common normal has zero length. The origin O_i is placed at the intersection point. The x_i axis is chosen to be normal to the plane containing z_{i-1} and z_i.

   If the z_{i-1} and z_i axes are parallel, there are infinite common normals. In this case, there is freedom to choose the location of the origin O_i along the z_i axis. A common practice is to place it in a convenient location, such as the center of the physical link.

   The final frame, $\{n\}$, is attached to the end-effector. Its origin O_n and orientation are typically chosen to align with a functionally important feature, such as the center or tip of the end-effector.

4. Once the coordinate frames are assigned, the geometric relationship between frame $\{i-1\}$ and frame $\{i\}$ can be described by four parameters:

   a_i is the distance from the z_{i-1} axis to the z_i axis, measured along the x_i axis.
   α_i is the angle between the z_{i-1} axis and the z_i axis, measured by a rotation about the x_i axis.
   d_i is the distance from the origin O_{i-1} to the intersection of the x_i axis with the z_{i-1} axis, measured along the z_{i-1} axis. For a prismatic joint, d_i is the joint variable.
   θ_i is the angle between the x_{i-1} axis and the x_i axis, measured by a rotation about the z_{i-1} axis. For a revolute joint, θ_i is the joint variable.

ISSN: 2523-6865
RENIECYT-SECIHTI: 1702902

García-Trinidad, Enrique, Arcos-Hernández, Emmanuel, Torres-Valle, José and Hernández-Borja, Carlos. [2025]. Mathematical and numeric analysis of a 4-DOF manipulator kinematics. Journal Computational Simulation. 9[20] 1-11: e10920111.
https://doi.org/10.35429/JCS.2025.9.20.1.1.11

For any given link in a kinematic chain, three of these four parameters are constant geometric properties of the link, while the fourth is the variable that describes the joint's motion.

Homogeneous Transformation Matrices

The four D-H parameters elegantly define the transformation from frame $\{i-1\}$ to frame $\{i\}$. This transformation, denoted by the homogeneous transformation matrix A_i, can be expressed as a product of four elementary rotations (Rot) and translations (Tras), as shown in Equation 3.

$$A_i = \text{Rot}_{x,\theta_i}\text{Tras}_{z,d_i}\text{Tras}_{x,a_i}\text{Rot}_{x,\alpha_i} \quad [3]$$

This sequence corresponds to the following operations to move frame $\{i-1\}$ to coincide with frame $\{i\}$:

1. Rotate about z_{i-1} by an angle θ_i.
2. Translate along z_{i-1} by a distance d_i.
3. Translate along the new x_i axis by a distance a_i.
4. Rotate about the new x_i axis by an angle α_i.

The resulting 4×4 matrix A_i, is a function of a single joint variable q_i and is given by:

$$A_i = \begin{bmatrix} cos\theta_i & -sin\theta_i cos\alpha_i & sin\theta_i sin\alpha_i & a_i cos\theta_i \\ sin\theta_i & cos\theta_i cos\alpha_i & -cos\theta_i sin\alpha_i & a_i sin\theta_i \\ 0 & sin\alpha_i & cos\alpha_i & d_i \\ 0 & 0 & 0 & 1 \end{bmatrix} \quad [4]$$

This matrix, shown in Equation 4, encapsulates both the rotation (the upper-left 3×3submatrix) and the translation (the upper-right 3×1 vector) that maps the coordinates of a point from frame $\{i\}$ to frame $\{i-1\}$.

Methodology

Applying the D-H formulation, the direct kinematics for any specific manipulator can be derived. This section details the derivation for a 4-DOF manipulator with revolute joints (Nugroho, Setiawan, & Munadi, 2024).

This is a common configuration for tasks such as pick and place, assembly, and material handling.

Direct Kinematics

The direct kinematic transformation, which describes the pose of the end-effector frame {4} with respect to the base frame {0}, is found by serially multiplying the transformation matrices of each individual link, A_i. The order of multiplication is critical and follows the chain from the base to the end-effector, as shown in Equation 5.

$$T_0^4 = A_1(q_0)A_2(q_1)A_3(q_2)A_4(q_3) \quad [5]$$

The resulting matrix T_0^4, is a 4×4 homogeneous transformation matrix that is a function of the four joint variables and takes the form shown in Equation 6.

$$T_0^4 = \begin{bmatrix} R & P \\ \mathbf{0} & 1 \end{bmatrix} = \begin{bmatrix} r_{11} & r_{12} & r_{13} & P_x \\ r_{21} & r_{22} & r_{23} & P_y \\ r_{31} & r_{32} & r_{33} & P_z \\ 0 & 0 & 0 & 1 \end{bmatrix} \quad [6]$$

The upper-left 3×3 submatrix is the rotation matrix describing the orientation of the end-effector frame relative to the base frame. The upper-right 3×1column vector P, gives the Cartesian coordinates (P_x, P_y, P_z) of the end-effector frame's origin with respect to the base frame's origin. Extracting these terms provides the final direct kinematics equations.

To provide a concrete mathematical derivation, a typical 4-DOF articulated arm with all revolute joints is considered. This robot consists of a waist (base) rotation, a shoulder joint, an elbow joint, and a wrist joint at the end-effector. All four joints are revolute. This architecture is characteristic of many educational and light industrial robots. A key feature of this design is that the axes for the shoulder, elbow, and wrist joints (joints 2, 3, and 4) are all parallel, which simplifies the kinematic analysis.

The first step is to translate the robot's physical geometry into a concise mathematical format by creating a table of D-H parameters. This table is the fundamental blueprint for the entire kinematic model.

ISSN: 2523-6865
RENIECYT-SECIHTI: 1702902

García-Trinidad, Enrique, Arcos-Hernández, Emmanuel, Torres-Valle, José and Hernández-Borja, Carlos. [2025]. Mathematical and numeric analysis of a 4-DOF manipulator kinematics. Journal Computational Simulation. 9[20] 1-11: e10920111.
https://doi.org/10.35429/JCS.2025.9.20.1.1.11

Box 1

Table 1
D-H Parameters

i	a_i	α_i	d_i	θ_i
1	0	$\pi/2$	d_1	q_0
2	a_2	0	0	q_1
3	a_3	0	0	q_2
4	a_4	0	0	q_3

Source: Own Elaboration

Table 1 is constructed based on a representative geometry shown in Figure 1, where d_1 is the base height, a_2 is the length of the upper arm (shoulder to elbow), a_3 is the length of the forearm (elbow to wrist), and a_4 is the length from the wrist joint to the end-effector tip. The twist angle $\alpha_1 = \pi/2$ is necessary to transition from the vertical rotation axis of the waist, z_0 to the horizontal rotation axis of the shoulder z_1.

Box 2

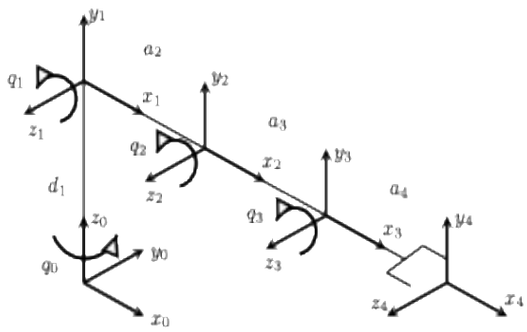

Figure 1
Axis assignment for the manipulator
Source: Own Elaboration

Substituting the parameters from Table 1 into Equation 4 for each link, we obtain the four individual transformation matrices, shown in Equations 7, 8, 9, and 10. Let $c_i = \cos(\theta_i)$ and $s_i = \sin(\theta_i)$.

For $j = 1$:

$$A_1 = \begin{bmatrix} c_1 & 0 & s_1 & 0 \\ s_1 & 0 & -c_1 & 0 \\ 0 & 1 & 0 & d_1 \\ 0 & 0 & 0 & 1 \end{bmatrix} \quad [7]$$

For $j = 2$:

$$A_2 = \begin{bmatrix} c_2 & -s_2 & 0 & a_2c_2 \\ s_2 & c_2 & 0 & a_2s_2 \\ 0 & 0 & 1 & 0 \\ 0 & 0 & 0 & 1 \end{bmatrix} \quad [8]$$

For $j = 3$:

$$A_3 = \begin{bmatrix} c_3 & -s_3 & 0 & a_3c_3 \\ s_3 & c_3 & 0 & a_3s_3 \\ 0 & 0 & 1 & 0 \\ 0 & 0 & 0 & 1 \end{bmatrix} \quad [9]$$

For $j = 4$:

$$A_4 = \begin{bmatrix} c_4 & -s_4 & 0 & a_4c_4 \\ s_4 & c_4 & 0 & a_4s_4 \\ 0 & 0 & 1 & 0 \\ 0 & 0 & 0 & 1 \end{bmatrix} \quad [10]$$

The total transformation matrix T_0^4 is the product of $A_1A_2A_3A_4$. The multiplication is performed sequentially. First, we find $T_0^2 = A_1A_2$, then $T_0^3 = T_0^2A_3$, and finally $T_0^4 = T_0^3A_4$.

Let $c_{23} = \cos(q_1 + q_2)$, $s_{23} = \sin(q_1 + q_2)$, $c_{234} = \cos(q_1 + q_2 + q_3)$, y $s_{234} = \sin(q_1 + q_2 + q_3)$.

After performing the symbolic matrix multiplication, the resulting matrix T_0^4 is:

$$T_0^4 = \begin{bmatrix} c_1c_{234} & -c_1s_{234} & s_1 & c_1(a_2c_2 + a_3c_{23} + a_4c_{234}) \\ s_1c_{234} & -s_1s_{234} & -c_1 & s_1(a_2c_2 + a_3c_{23} + a_4c_{234}) \\ s_{234} & c_{234} & 0 & d_1 + a_2s_2 + a_3s_{23} + a_4s_{234} \\ 0 & 0 & 0 & 1 \end{bmatrix} \quad [11]$$

From the last column of this matrix shown in Equation 11, we can extract the direct kinematics equations for the end-effector position (P_x, P_y, P_z):

$$\begin{aligned} P_x &= c_1(a_2c_2 + a_3c_{23} + a_4c_{234}) \\ P_y &= s_1(a_2c_2 + a_3c_{23} + a_4c_{234}) \\ P_z &= d_1 + a_2s_2 + a_3s_{23} + a_4s_{234} \end{aligned} \quad [12]$$

This set of terms present in Equation 12 provides the direct and unique mapping from any given set of joint angles (q_0, q_1, q_2, q_3) to the resulting 3D position of the end-effector.

Inverse Kinematics

Inverse kinematics (IK) addresses the problem of finding the necessary joint angles to position the end-effector at a desired location and orientation in Cartesian space. This is a fundamentally more complex task than direct kinematics and is essential for any practical manipulator control application (KuCuk& Bingul, 2004). The difficulty in solving the IK problem stems from the non-linear trigonometric equations derived from direct kinematics. For a general 4-DOF manipulator, several challenges must be addressed.

ISSN: 2523-6865
RENIECYT-SECIHTI: 1702902

García-Trinidad, Enrique, Arcos-Hernández, Emmanuel, Torres-Valle, José and Hernández-Borja, Carlos. [2025]. Mathematical and numeric analysis of a 4-DOF manipulator kinematics. Journal Computational Simulation. 9[20] 1-11: e10920111.
https://doi.org/10.35429/JCS.2025.9.20.1.1.11

For example, a solution to the IK problem is not guaranteed, as if the target pose is outside the robot's reachable workspace, no set of real-valued joint angles can satisfy the kinematic equations. Furthermore, a single reachable pose can often be achieved by multiple distinct configurations.

A classic example is the elbow-up and elbow-down ambiguity. For the manipulator in question, additional solutions can arise from the base rotation, such as a left-shoulder versus right-shoulder configuration to reach the same point. The existence of multiple solutions requires the control system to implement a strategy to choose a unique and consistent solution, often based on criteria such as proximity to the current configuration or avoiding joint limits.

IK solutions can be broadly classified into two types: analytical and numerical. Analytical or closed-form solutions provide an exact set of equations to solve for the joint variables. They are computationally very fast and efficient, making them ideal for real-time control. Additionally, they provide a complete characterization of all possible solutions. However, closed-form solutions only exist for manipulators that satisfy certain geometric conditions.

Numerical solutions use iterative algorithms to converge on a solution. They are more general and can be applied to any robot geometry, but they are computationally more expensive and may fail to converge to a solution.

Analytical Solution

A critical aspect of solving the IK for the 4-DOF manipulator is recognizing that it cannot independently achieve an arbitrary 6-DOF pose (3 for position, 3 for orientation). A system with 6 constraints and only 4 controllable variables is overdetermined. Therefore, any solvable IK problem for this manipulator must have an implicit constraint. The problem is usually framed as finding the joint angles for a 3D position (P_x, P_y, P_z) with a single orientation constraint. Two main analytical methods can be used for this solution: the geometric approach and the algebraic approach. The geometric approach is often more intuitive as it relies on decomposing the spatial problem into a series of simpler 2D problems using trigonometry.

The base rotation angle, q_0, determines the vertical plane in which the rest of the arm operates. By projecting the manipulator onto the base's $x_0 - y_0$ plane, q_0 can be found directly from the desired end-effector coordinates (P_x, P_y), as shown in Equation 13.

$$q_0 = \text{atan2}(P_y, P_x) \quad [13]$$

The two-argument arctangent function, atan2 is used to correctly determine the quadrant of the angle and handle the case where $P_x = 0$. A second solution for q_0 also exists, which is $q_0' = q_0 + \pi$. This corresponds to a rear-facing solution, which may require the other joints to hyperextend and is often discarded as impractical.

With q_0 known, the 3D problem reduces to a 2D problem within the vertical plane defined by q_0. If a new coordinate system is defined within this plane, the horizontal distance from the base axis to the end-effector is $r = \sqrt{P_x^2 + P_y^2}$. The position of its center, (P_{ex}, P_{ez}), relative to the origin of frame {1} is given in Equation 14.

$$\begin{aligned} P_{ex} &= r - a_4\cos(\phi) \\ P_{ez} &= P_z - d_1 - a_4\sin(\phi) \end{aligned} \quad [14]$$

Here, ϕ is the desired angle of the end-effector with respect to the horizontal, which is a required input for a fully constrained problem. Now that we have a planar manipulator with two revolute joints that must reach the point (P_{ex}, P_{ez}), the squared distance from the shoulder to the wrist is $D^2 = P_{ex}^2 + P_{ez}^2$. Applying the law of cosines to the triangle formed by links a_2, a_3, and the line segment D, we get $D^2 = a_2^2 + a_3^2 - 2a_2a_3\cos(\pi - q_2)$. Since $\cos(\pi - q_2) = -\cos(q_2)$, this simplifies to:

$$\cos(q_2) = \frac{P_{wx}^2 + P_{wz}^2 - a_2^2 - a_3^2}{2a_2a_3} \quad [15]$$

This Equation 15 can be solved for q_2. Since $\cos(q_2) = \cos(-q_2)$, there are two possible solutions for q_2, corresponding to the elbow-up and elbow-down configurations:

$$q_2 = \pm\text{acos}\left(\frac{P_{ex}^2 + P_{ez}^2 - a_2^2 - a_3^2}{2a_2a_3}\right) \quad [16]$$

ISSN: 2523-6865
RENIECYT-SECIHTI: 1702902

García-Trinidad, Enrique, Arcos-Hernández, Emmanuel, Torres-Valle, José and Hernández-Borja, Carlos. [2025]. Mathematical and numeric analysis of a 4-DOF manipulator kinematics. Journal Computational Simulation. 9[20] 1-11: e10920111.
https://doi.org/10.35429/JCS.2025.9.20.1.1.11

Once q_2 is known, as shown in Equation 16, q_1 can be found using trigonometric identities. Let $\beta = \text{atan2}(P_{wz}, P_{wx})$ and let γ be the angle inside the triangle at the shoulder joint, which can be found with another application of the law of cosines, as shown in Equation 17.

$$\cos(\gamma) = \frac{a_2^2 + D^2 - a_3^2}{2a_2 D} \quad [17]$$

Then, q_1 is the sum or difference of these angles, depending on the chosen elbow configuration:

$$q_1 = \beta \mp \gamma \quad [18]$$

The sign in Equation 18 depends on whether the elbow-up $(+q_2)$ or elbow-down $(-q_2)$ solution was chosen.

The final joint angle, q_3, is determined by the constraint that the sum of the joint angles must equal the desired absolute angle ϕ, i.e., $\phi = q_1 + q_2 + q_3$.

Therefore, q_3 can be solved directly in Equation 19.

$$q_3 = \phi - q_1 - q_2 \quad [19]$$

This geometric approach yields up to two distinct solutions for the set of joint angles (q_0, q_1, q_2, q_3) for a given reachable pose.

The algebraic approach is more systematic and relies on manipulating the matrix equations of direct kinematics. The goal is to isolate the joint variables one by one.

The process begins with Equation 20, where the desired end-effector pose T_{obj} is known:

$$T_0^4 = T_{obj} = \begin{bmatrix} n_x & s_x & a_x & P_x \\ n_y & s_y & a_y & P_y \\ n_z & s_z & a_z & P_z \\ 0 & 0 & 0 & 1 \end{bmatrix} \quad [20]$$

Here, we can pre-multiply both sides by the inverse of the first transformation matrix, A_1^{-1} to get Equation 21.

$$\begin{aligned} A_1^{-1}T_0^4 &= A_2A_3A_4 \\ A_1^{-1}T_{obj} &= A_2A_3A_4 \end{aligned} \quad [21]$$

The matrix A_1^{-1} is easy to compute. The product on the right side, $A_2A_3A_4$, results in a matrix whose elements are functions of q_1, q_2, q_3. The matrix on the left side, $A_1^{-1}T_{obj}$, has elements that are functions of q_0 and the known components of the target pose.

By equating the corresponding elements of the matrices on both sides of the equation, a system of twelve scalar equations is generated. These equations can be solved systematically. For example, in Equation 22, equating the $(1,4)$ and $(2,4)$ elements yields:

$$\begin{aligned} P_x c_1 + P_y s_1 &= a_2c_2 + a_3c_{23} + a_4c_{234} \\ P_z - d_1 &= a_2s_2 + a_3s_{23} + a_4s_{234} \end{aligned} \quad [22]$$

This algebraic method, though less intuitive, is more rigorous and less prone to geometric oversights. It leads to the same set of solutions as the geometric approach, confirming the results through a different mathematical pathway. The full derivation involves extensive use of trigonometric identities to isolate the unknown joint angles.

Numerical Solution

Numerical methods offer an alternative approach to analytical solutions and are characterized by iterative algorithms that progressively refine an initial guess to find the joint angles that minimize the error between the current and desired pose. This effectively transforms the IK problem into an optimization problem, where the objective is to minimize a cost function representing the pose error.

The main advantage of numerical methods lies in their generality and versatility. They are highly applicable to different types of manipulators with complex kinematic structures, such as redundant manipulators. All this without requiring mechanism-specific mathematical derivations beyond direct kinematics. This makes them a good choice when dealing with complex or redundant manipulators where analytical solutions are intractable. The most common numerical methods are:

ISSN: 2523-6865
RENIECYT-SECIHTI: 1702902

García-Trinidad, Enrique, Arcos-Hernández, Emmanuel, Torres-Valle, José and Hernández-Borja, Carlos. [2025]. Mathematical and numeric analysis of a 4-DOF manipulator kinematics. Journal Computational Simulation. 9[20] 1-11: e10920111.
https://doi.org/10.35429/JCS.2025.9.20.1.1.11

1. Newton-Raphson, without Jacobian pseudoinverse (NR pse=0) or with Jacobian pseudoinverse (NR pse=1), is a method that iteratively adjusts joint angles by solving for joint velocity changes using the Jacobian pseudoinverse to reduce the error. It is known for its quadratic convergence rate for non-linear functions.

2. Gauss-Newton, without Jacobian pseudoinverse (GN pse=0) or with Jacobian pseudoinverse (GN pse=1), is an extension of Newton's method that approximates the Hessian matrix using the Jacobian matrix.

3. Levenberg-Marquardt (LM), is a hybrid optimization algorithm that combines the strengths of Gauss-Newton and gradient descent. It employs a damping factor to control the step size, which significantly improves robustness, especially when approaching singularities. Some versions include Wampler's (LMW), which allows for dynamic handling of singularities by introducing a damping factor that can be 1×10^{-4} or 1×10^{-6}, considering that a larger damping factor leads to a more stable but slower solution. Another numerical method is Chan's (LMC), which uses a fixed damping factor of 1.0 or 0.1 and provides the method with the stability to resolve singularities and detect targets that the manipulator cannot physically reach. Finally, Sugihara introduces another LM variant (LMS) that allows the LM method to converge under different conditions through a specific factor or bias, which can be 0.001 or 0.0001 .

For the numerical solution of this manipulator, the solutions provided by the Robotics Toolbox (RTB) in Python by Peter Corke are used (Haviland & Corke, 2024).

Results

For the following poses $[P_x, P_y, P_z, \phi, \theta, \psi]$, shown in Table 2, the inverse kinematics of the manipulator is solved using the methods described above. Tables 3, 4, and 5 provide the solutions to the described poses. Figures 2, 3, and 4 show the manipulator's pose for each solution.

Box 3

Table 2
Different poses to be solved

Pose	P_x	P_y	P_z
1	-0.0789	-0.025	1.051
2	0.227	-0.118	0.853
3	-0.333	0.077	0.573
Pose	ϕ	θ	ψ
1	-89.997°	-49.375°	-162.429°
2	-90.000°	-8.911°	152.515°
3	89.977°	-73.462°	166.939°

Source: Own Elaboration

Box 4

Table 3
Solutions to pose 1

Method	q_0	q_1	q_2	q_3
Analítico	0.3067	1.352	0.6457	0.282
NR pse=0	0.3067	-4.418	-0.6478	-5.221
GN pse=0	0.3067	-4.419	-0.6464	-5.221
NR pse=1	0.3067	1.346	0.6605	0.2737
GN pse=1	0.3067	1.352	0.646	0.2818
LMW 1e-4	0.3067	1.869	-0.6589	-5.214
LMW 1e-6	0.3067	1.865	-6.931	1.062
LMC 1.0	0.3067	-4.934	0.6516	0.2785
LMC 0.1	0.3067	1.351	0.6479	0.2807
LMS 0.001	0.3067	1.87	-0.6602	1.07
LMS 0.0001	0.3067	1.349	0.6531	0.2776

Source: Own Elaboration

Box 5

Table 4
Solutions to pose 2

Method	q_0	q_1	q_2	q_3
Analítico	2.913	-0.7324	1.833	0.1816
NR pse=0	-3.37	-0.7327	-4.447	0.1787
GN pse=0	-3.37	-0.7321	1.834	0.1801
NR pse=1	2.913	-5.689	-1.835	-3.761
GN pse=1	2.913	-0.734	-4.449	0.182
LMW 1e-4	-3.37	0.5909	-8.117	2.525
LMW 1e-6	-3.37	-7.016	-4.45	0.1816
LMC 1.0	2.913	-5.693	-1.833	-3.759
LMC 0.1	2.913	0.5905	-1.833	2.525
LMS 0.001	-3.37	-0.7332	-4.447	0.1793
LMS 0.0001	2.913	-0.7329	1.834	0.181

Source: Own Elaboration

ISSN: 2523-6865
RENIECYT-SECIHTI: 1702902

García-Trinidad, Enrique, Arcos-Hernández, Emmanuel, Torres-Valle, José and Hernández-Borja, Carlos. [2025]. Mathematical and numeric analysis of a 4-DOF manipulator kinematics. Journal Computational Simulation. 9[20] 1-11: e10920111.
https://doi.org/10.35429/JCS.2025.9.20.1.1.11

Box 6

Table 5
Solutions to pose 3

Method	q_0	q_1	q_2	q_3
Analítico	-0.4797	0.9167	-0.3922	2.462
NR pse=0	-0.4797	0.5936	-5.866	1.975
GN pse=0	-0.4797	0.9232	-0.4082	2.471
NR pse=1	-0.4797	-5.682	-5.884	1.986
GN pse=1	-0.4797	-5.688	0.4133	-4.306
LMW 1e-4	-0.4797	0.6025	-5.888	1.988
LMW 1e-6	-0.4797	0.9207	-0.4022	2.468
LMC 1.0	-0.4797	0.9172	-0.3935	-3.821
LMC 0.1	-0.4797	-5.366	-0.3934	2.462
LMS 0.001	-0.4797	-5.359	-0.4115	-3.81

Source: Own elaboration

Box 7

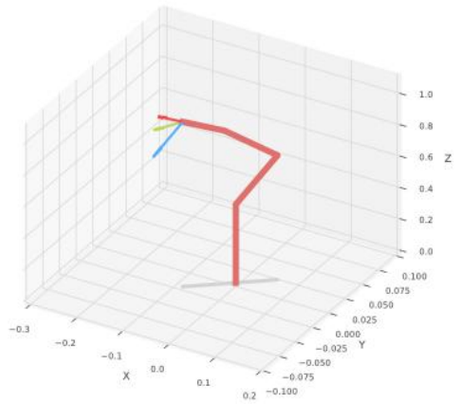

Figure 2
Pose 1 of the manipulator
Source: Own Elaboration

Box 9

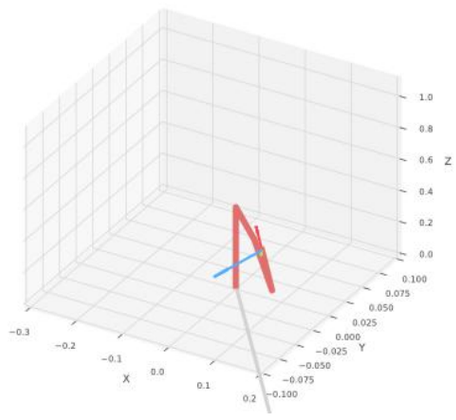

Figure 3
Pose 2 of the manipulator
Source: Own Elaboration

Box 10

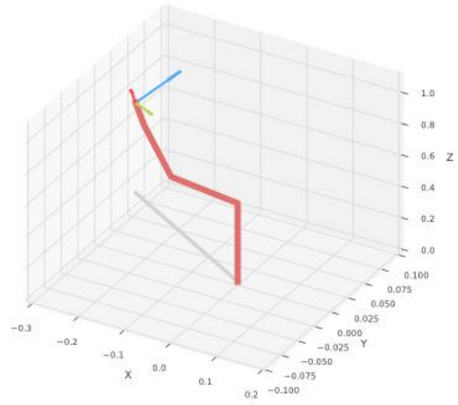

Figure 4
Pose 1 of the manipulator
Source: Own Elaboration

Conclusions

The variability observed in Tables 3, 4, and 5 underscores the problem of multiple solutions and highlights the significant influence of algorithm parameters, such as damping factors and initial conditions, on the convergence path and the resulting configuration. It also demonstrates that some numerical solutions may be less practical in terms of large joint angles or proximity to limits.

Numerical methods transform the IK problem into an optimization problem, representing a fundamental paradigm shift. Instead of seeking an exact closed-form inversion, the problem is reformulated as the minimization of an error function. This approach allows for a general solution that does not depend on the manipulator's specific geometric properties, making it applicable to any robot configuration.

The trade-off is the loss of an exactness guarantee and the introduction of challenges related to convergence and local minima. This shift in approach enables the development of highly versatile robotics software and control systems that can adapt to a wide diversity of robot designs without requiring the derivation of complex analytical solutions. However, the results from numerical methods require careful evaluation in a practical context.

ISSN: 2523-6865
RENIECYT-SECIHTI: 1702902

García-Trinidad, Enrique, Arcos-Hernández, Emmanuel, Torres-Valle, José and Hernández-Borja, Carlos. [2025]. Mathematical and numeric analysis of a 4-DOF manipulator kinematics. Journal Computational Simulation. 9[20] 1-11: e10920111.
https://doi.org/10.35429/JCS.2025.9.20.1.1.11

The exhaustive analysis of the 4-DOF manipulator reveals a tightly interconnected chain of mathematical and physical principles. This article has systematically detailed this chain, demonstrating how each concept builds upon the previous one to form a complete model of the robot's behavior. The synthesis of these topics provides an essential understanding for advanced robotics applications.

While the current analysis provides a comprehensive understanding of manipulator kinematics, the next logical step for future work is to extend this analytical framework to the realm of robot dynamics. This extension would involve the systematic incorporation of critical physical factors such as the mass distribution of each link, its moments of inertia, and the influence of external forces acting on the manipulator.

The overall purpose of this dynamic analysis is to accurately model the accelerations and torques required for the robot's motion. In doing so, the bridge from kinematic configuration analysis to a complete understanding and control of dynamic movement would be effectively completed.

Conflict of interest

The authors declare no interest conflict. They have no known competing financial interests or personal relationships that could have appeared to influence the article reported in this article.

Author contribution

García-Trinidad, Enrique: Contributed to the project idea, research method and technique.

Arcos-Hernández, Emmanuel: Contributed to the review and revision of the mathematical analysis.

Torres-Valle, José: Contributed to the derivation of the DH parameters.

Hernández-Borja, Carlos: Contributed to the Linux and ROS2 system configuration.

Availability of data and materials

The data that support the findings of this study are openly available in the main author's GitHub repository at https://github.com/enriGarcia.

References

Basics

Bao, G., Liu, S., & Zhao, H. (2017/05). Kinematics simulation of 4 dof manipulator. In Proceedings of the 2017 2nd international conference on materials science, machinery and energy engineering (msmee 2017) (p. 400-408). Atlantis Press. Retrieved from https://doi.org/10.2991/msmee-17.2017.81 doi: 10.2991/msmee-17.2017.81

Corke, P. I. (2007). A simple and systematic approach to assigning denavit–hartenberg parameters. IEEE Transactions on Robotics, 23 (3), 590-594. doi: 10.1109/TRO.2007.896765

Supports

Guida, R., De Simone, M. C., Daˇsi´c, P., & Guida, D. (2019, jul). Modeling techniques for kinematic analysis of a six-axis robotic arm. IOP Conference Series: Materials Science and Engineering, 568 (1), 012115. Retrieved from https://dx.doi.org/10.1088/1757899X/568/1/012115 doi: 10.1088/1757-899X/568/1/012115

Haviland, J., & Corke, P. (2024). Manipulator differential kinematics: Part i: Kinematics, velocity, and applications. IEEE Robotics and Automation Magazine, 31 (4), 149-158. doi:10.1109/MRA.2023.3270228

KuCuk, S., & Bingul, Z. (2004). The inverse kinematics solutions of industrial robot manipulators. In Proceedings of the ieee international conference on mechatronics, 2004. icm'04. (pp.274–279).

Malik, A., Lischuk, Y., Henderson, T., & Prazenica, R. (2022). A deep reinforcement-learning approach for inverse kinematics solution of a high degree of freedom robotic manipulator. Robotics, 11 (2). Retrieved from https://www.mdpi.com/2218-6581/11/2/44 doi: 10.3390/robotics11020044

Manseur, R., & Doty, K. L. (1988). A fast algorithm for inverse kinematic analysis of robot manipulators. The International Journal of Robotics Research, 7 (3), 52-63. Retrieved from https://doi.org/10.1177/027836498800700304 doi: 10.1177/027836498800700304

ISSN: 2523-6865
RENIECYT-SECIHTI: 1702902

García-Trinidad, Enrique, Arcos-Hernández, Emmanuel, Torres-Valle, José and Hernández-Borja, Carlos. [2025]. Mathematical and numeric analysis of a 4-DOF manipulator kinematics. Journal Computational Simulation. 9[20] 1-11: e10920111.
https://doi.org/10.35429/JCS.2025.9.20.1.1.11

Spong, M. (2022). Robot modeling and control, second edition. IEEE Control Systems, 42 (1), 126-128. doi: 10.1109/MCS.2021.3122271

Differences

Mohammed, A. A., & Sunar, M. (2015). Kinematics modeling of a 4-dof robotic arm. In 2015 international conference on control, automation and robotics (p. 87-91). doi: 10.1109/ICCAR.2015.7166008

Nugroho, E. A., Setiawan, J. D., & Munadi, M. (2024). Physical modeling of a 4-dof manipulator for learning purposes using cad and gui. International Journal of Mechanical Engineering and Robotics Research, 13 (3), 392–401.

ISSN: 2523-6865
RENIECYT-SECIHTI: 1702902

García-Trinidad, Enrique, Arcos-Hernández, Emmanuel, Torres-Valle, José and Hernández-Borja, Carlos. [2025]. Mathematical and numeric analysis of a 4-DOF manipulator kinematics. Journal Computational Simulation. 9[20] 1-11: e10920111.
https://doi.org/10.35429/JCS.2025.9.20.1.1.11

Journal Computational Simulation 9[20]1-17: e2092017
Article

Dynamic control analysis by simulation of the main components of a Hall Effect thruster

Análisis dinámico del control mediante simulación de los componentes principales un propulsor de efecto Hall

Aburto–Policarpo Gethsi[a], Castillo-Sánchez Martín*[b] and López-Cárdenas Rodrigo[c]

[a] Instituto Politécnico Nacional • 0009-0001-2050-720X
[b] Instituto Politécnico Nacional • 0000-0002-2563-3395 • 36671
[c] Instituto Politécnico Nacional • 0009-0007-2628-9147 • 162756

SECIHTI classification:

Area: Engineering
Field: Technological sciences
Discipline: Space technology
Subdiscipline: Spaceships

https://doi.org/10.35429/JCS.2025.9.20.2.1.17
Article History:
Received: June 30, 2025
Accepted: December 15, 2025

* ✉ [mcastillos@ipn.mx]

Abstract

The aim of this research work is to analyze, through the simulation of the controllers using Simulink ™, the behavior of the main components that make up a Hall effect electric thruster used in a spacecraft, these are: Magnetic field, Voltage and Injector, the simulated controls for the components were P, I, PI, PD, PID controls, it was found that the PI and PID controllers are the most suitable to regulate the magnetic field, due to the precise tracking of the reference, unlike the PD controller, whose abrupt changes make it physically unfeasible. Regarding voltage control, the PI controller stands out for its balance between efficiency and physical feasibility, while the PD and PID controllers, although acceptable, present excessively rapid variations that hinder their real implementation. Likewise, in scenarios where a faster adjustment is prioritized, the PID could be considered, as long as its practical limitations are evaluated.

Objectives	Methodology	Contribution
Controller simulation Hall effect electric thruster: Magnetic field Voltage Injector 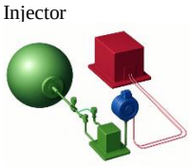 **Magnetic field** **Fuel** **Propellant**	Magnetic Field $H(s) = \frac{200}{s+1}$ Voltage $H(s) = \frac{2000}{s^2+s+1}$ Injector $H(s) = \frac{k}{s+1}$	PI and PID controllers are best suited for regulating magnetic fields, injector, and voltage control.

Controllers, Hall effect, spacecraft

Resumen

El objetivo de este trabajo de investigación es analizar mediante la simulación de los controladores mediante Simulink™, el comportamiento de los componentes principales que conforman un propulsor eléctrico de efecto Hall utilizado en una nave espacial, estos son: Campo magnético, Tensión e Inyector, los controles simulados para los componentes fueron controles P, I, PI, PD, PID, se encontró que los controladores PI y PID son los más adecuados para regular el campo magnético, debido a el seguimiento preciso de la referencia, a diferencia del controlador PD, cuyos cambios abruptos lo hacen físicamente inviable. En cuanto al control de tensión, el controlador PI destaca por su balance entre eficiencia y factibilidad física, mientras que los controladores PD y PID, aunque aceptables, presentan variaciones demasiado rápidas que dificultan su implementación real. Así mismo en escenarios donde se priorice un ajuste más rápido, el PID podría considerarse, siempre y cuando se evalúen sus limitaciones prácticas.

Objetivos	Metodología	Contribución
Simulación de controladores propulsor eléctrico de efecto Hall: Campo magnético Voltaje Inyector 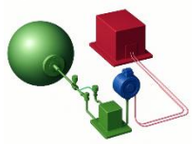 **Alimentación** **Propelente** **Propulsor**	Campo Magnético $H(s) = \frac{200}{s+1}$ Tensión $H(s) = \frac{2000}{s^2+s+1}$ Inyector $H(s) = \frac{k}{s+1}$	Los controladores PI y PID son los más adecuados para regular campos magnéticos, el inyector, y el control de voltaje.

Controladores, efecto Hall, nave espacial

Area: Promotion of frontier research and basic science in all fields of knowledge

Citation: Aburto–Policarpo Gethsi, Castillo-Sánchez Martín and López-Cárdenas Rodrigo [2025]. Dynamic control analysis by simulation of the main components of a Hall Effect thruster. Journal Computational Simulation. 9[20] 1-17: e20920117

Introduction

Electric propulsion is a technology designed to achieve thrust with high exhaust velocities, resulting in a reduction in the amount of propellant required for a given space mission or application compared to chemical propulsion. The reduced propellant mass can significantly decrease the launch mass of a spacecraft or satellite, leading to lower costs by using smaller launch vehicles to deliver a desired mass into a specific orbit or to a target in deep space. In general, electric propulsion (EP) encompasses any propulsion technology in which electricity is used to increase the propellant's exhaust velocity. There are many figures of merit for electric propellants, but mission and application planners are primarily interested in thrust, specific impulse, and overall efficiency when relating propellant performance to mass delivered and the change in spacecraft velocity during thrust periods. (Goebel, D. M. 2008. Merino, M. 2016. Hey, F. G. 2018).

There are various types of electric thrusters used by space agencies and research centers, each with specific characteristics in terms of thrust, specific impulse, and efficiency. However, there is a need to optimize these parameters based on the spacecraft's mass and the change in velocity during thrust periods. The main problem lies in the need for detailed characterization and simulation of this type of electric thruster in terms of its efficiency, power requirements, voltage, current intensity, and specific impulse.

This work analyzes, through the simulation of the controllers of a Hall effect thruster using mathematical software, the design and specific characteristics of an electric propulsion system in a spacecraft, considering thrust, power and specific impulse in different types of space missions (ESA. 2002. Lev, D. 2019).

Hall Effect Drivers (HET)

When a current flows in a conductor or semiconductor and a magnetic field is applied perpendicular to the current, a voltage is generated across the material in a direction perpendicular to the planes containing the current and the magnetic field, as shown in Figure 1. This voltage is known as the Hall voltage, and the phenomenon is known as the Hall effect. (Jiles, D. 2001).

Box 1

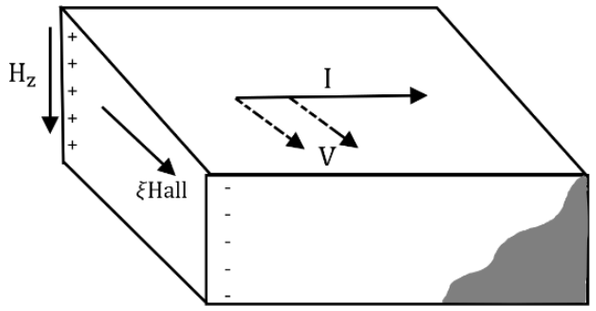

Figure 1

Hall electromagnetic field. H is the magnetic field, I, is the conventional current, ξHall is the Hall field, and v is the electron velocity. Adapted from (Jiles, D. 2001)

The Hall effect thruster is an electrostatic ion accelerator that uses a cross-field cycloidal ion discharge accelerated by an electrostatic field in the thrust stream to generate plasma. The plasma electrons interact with a magnetic field to produce the electrostatic field described by the Hall effect. Perpendicular fields electrostatically accelerate the ions to high speeds.

The magnetic coils are positioned perpendicular to the main discharge for simplicity, and some additional control can be implemented. This type of thruster is both an electrostatic and electromagnetic EP system. The electrons follow a particular closed drift path perpendicular to the current flow and the magnetic field (Hall effect). The structure of a Hall thruster consists of an annular discharge chamber with a radial magnetic field between a cylindrical ferromagnetic pole and an external ferromagnetic ring (Figure 2).

The chamber forms an outlet for the accelerated ions at one end. Electrons travel from the cathode to the anode in an externally applied electric field. The radial magnetic field generates a perpendicular force from both fields, causing them to drift in an azimuthal direction (hence the Hall current). When the electron moves toward the anode (accelerated), its spin radius increases compared to when it moves toward the cathode (decelerated), resulting in a net azimuthal drift (Hall effect). The electrons are efficiently trapped in an azimuthal orbit near the area of maximum field strength. The axial mobility of the electrons is eradicated, allowing the plasma to maintain a very high electric field along the axis of the discharge chamber.

ISSN: 2523-6865
RENIECYT-SECIHTI: 1702902

Aburto–Policarpo Gethsi, Castillo-Sánchez Martín and López-Cárdenas Rodrigo [2025]. Dynamic control analysis by simulation of the main components of a Hall Effect thruster. Journal Computational Simulation. 9[20] 1-17: e20920117
https://doi.org/10.35429/JCS.2025.9.20.2.1.17

There is an external cathode, which provides additional electrons to neutralize the accelerated ions in the discharge chamber. (Poonam T. 2020).

Hall thrusters require relatively simple power conditioning and provide a desirable specific impulse range, but xenon is the only propellant that can be used safely. These thrusters optimize performance at very low power. Exhaust velocities can reach over 65,000 m/s, and their power range extends from around 200 W to tens of kW. They have propellant efficiencies of over 50%, thrust efficiencies of around 45–55%, and thrust exceeding 70 mN. They also have a high specific impulse of 1,000–8,000 s. There is a 5% loss in specific impulse due to propellant flow in the hollow cathode.

Starting point parameters and scaling laws

The rocket equation reduces to a propellant weight problem: as propellant is added to a spacecraft, the mass of the system increases, and increasingly longer propellant burns are required to accelerate the increased mass of the system.

This establishes a practical upper limit on the amount of fuel carried, since at a certain point only marginal changes in velocity (Δv) can be achieved by adding more propellant. The momentum transfer efficiency of a propellant can be maximized by maximizing the propellant's exit velocity, vex; this, in turn, reduces the amount of propellant required to achieve a desired Δv. (Oh B. 2023).

Box 2

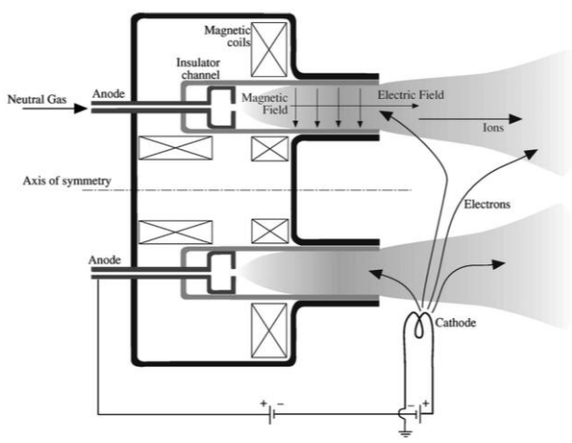

Figure 2
Physical diagram of a Hall effect thruster. (Adapted from Poonam T. 2020)

Two thrusters operating at a similar voltage will accelerate ions through a similar potential, resulting in similar escape velocities (neglecting specific design losses) and therefore similar specific impulse. These scaling laws are:

$$P \propto R^2 \quad [1]$$
$$T \propto R^2 \quad [2]$$
$$W \propto R \quad [3]$$

Where R represents the outer radius of the propeller channel and W represents the channel width (the difference between the outer and inner radii).

Concepts of Electric and Magnetic Fields

The propellant is ionized by bombarding it with electrons trapped in the main channel.

The electrons are trapped by a radial magnetic field. An axial electric field is then applied, causing the electrons to drift.$\vec{E} \times \vec{B}$, This results in an azimuthal velocity (a drift-enabled Hall current). The purpose of the device's electric field is to transport electrons from the cathode to the channel and accelerate the ionized propellant away from the propellant. (Oh B. 2023). In electric propulsion, especially in Hall-type thrusters and some magneto plasmic thrusters, the drift phenomenon $\vec{E} \times \vec{B}$ It is a determining factor in generating thrust.

In a Hall thruster, it is established that:

– An electric field $\vec{E}$ radial between the anode (interior) and the cathode (exterior).

– A magnetic field$\vec{B}$ axial (perpendicular to the electric field).

The combination of these two fields generates a drift velocity.

The principles of drift$\vec{E} \times \vec{B}$ They can be conceptualized as follows: Consider a region of space with a uniform magnetic field. A charge moving in this field will travel in endless circles. Now, consider the same configuration with a uniform electric field oriented perpendicular to the magnetic field. When the charge is at a point of higher electric potential, it will possess less kinetic energy and travel more slowly; conversely, at a point of lower electric potential, it will travel more quickly.

ISSN: 2523-6865
RENIECYT-SECIHTI: 1702902

Aburto–Policarpo Gethsi, Castillo-Sánchez Martín and López-Cárdenas Rodrigo [2025]. Dynamic control analysis by simulation of the main components of a Hall Effect thruster. Journal Computational Simulation. 9[20] 1-17: e20920117
https://doi.org/10.35429/JCS.2025.9.20.2.1.17

This causes the particle to alternate between a narrow orbit and a large orbit (in regions of lower and higher potential, respectively) and results in a drift perpendicular to both the electric and magnetic fields. Figure 3 shows a sample trajectory of a particle trapped within such a field. This phenomenon is known as drift $\vec{E} \times \vec{B}$ and it is the central mechanism that allows electrons to be trapped inside the thruster channel in an azimuthal flow (this is the Hall current that gives Hall thrusters their characteristic name) (Oh B. 2023).

Box 3

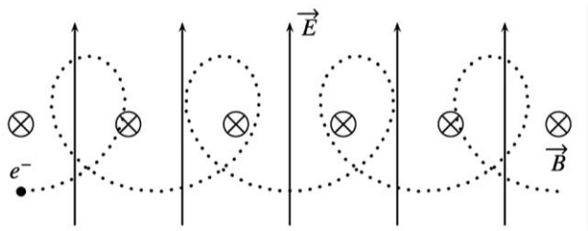

Figure 3

Cycloidal trajectory of an electron undergoing drift $\vec{E} \times \vec{B}$ in a uniform electric and magnetic field. (Taken from Oh B. 2023)

A useful way to characterize the magnetic field in a propellant is by the radii of gyration of the ions present in the system (this radius is known in the field as the Larmor radius). The Larmor radius for a generic charge in a magnetic field can be found as:

$$r_q = \frac{mv_\perp}{qB} \quad [4]$$

Where r_q is the Larmor radius for a particle of mass m and charge q, with velocity perpendicular to the field B of magnitude v⊥. The Larmor radius can be calculated by knowing the magnetic field strength along with the particle's velocity, mass, and charge. For particles in a Hall thruster, the Larmor radii are:

$$r_e = \frac{1}{B}\sqrt{\frac{8m_e kT_e}{\pi e}} \quad [5]$$

$$r_i = \frac{1}{B}\sqrt{\frac{2m_i V_b}{e}} \quad [6]$$

Where r_e and r_i are the Larmor radii of an electron and an ion, respectively; B is the radial magnetic field strength; me and mi are the masses of an electron and an ion, respectively; T_e is the temperature of the electron in units of eV; k is Boltzmann's constant; V_b is the propellant beam voltage; and e, is the fundamental load (Oh B. 2023).

Propellant Selection and Channel Length

Neutral propellant is dispensed from a diffuser at the bottom of the channel. As the neutrals diffuse through the channel, they come into contact with the cloud of high-energy electrons trapped in the ionization region. Maximizing the amount of ionized propellant maximizes propellant efficiency, dictating a channel length that must be significantly longer than the mean ionizing free path, but not so long as to cause performance losses due to interactions with a larger surface area. Generally, this length is chosen to be of the same order of magnitude as the mean free path length. One calculation method is:

$$\lambda = \frac{v_n}{n_e(\sigma_i v_e)} \quad [7]$$

Where v_n is the axial velocity of a neutral propellant atom, n_e is the electron density of the channel and $\langle \sigma_i v_e \rangle$ represents the ionization "cross-section" (which quantifies the probability of ionization) of the neutral propellant for collisions with electrons at a particular electron temperature. The amount v_n It can be calculated using Bernoulli's equation, given the parameters of a particular feed piping system and the propellant flow properties. The ionization cross-section, $\langle \sigma_i v_e \rangle$, It is an experimentally derived value that varies with the type of propellant and the energy level of the electrons. (Oh B. 2023).

Methodology

Modeling the Hall Effect Thruster

In the electric propulsion model, each main system component is represented by a transfer function in the Laplace domain. The constant appearing in the numerator of each function has a specific physical meaning depending on the block it corresponds to. (Sánchez, J. 2015).

ISSN: 2523-6865
RENIECYT-SECIHTI: 1702902

Aburto–Policarpo Gethsi, Castillo-Sánchez Martín and López-Cárdenas Rodrigo [2025]. Dynamic control analysis by simulation of the main components of a Hall Effect thruster. Journal Computational Simulation. 9[20] 1-17: e20920117
https://doi.org/10.35429/JCS.2025.9.20.2.1.17

Injector

Based on the propeller dynamics, a simplified differential equation is formulated to model the opening and closing of a propeller, considering only the valve size. The injector's transfer function is described as:

$$H(s) = \frac{k}{s+1} \quad [8]$$

In this context, *k* this represents the mass flow gain injected per unit of input signal. Physically, this means that, for a given control stimulus (electrical potential or current), the injector is able to transfer a proportional amount of mass to the propulsion system.

A higher value of *k* It increases the mass flow rate in response to the same input. A lower value reduces the injection capacity.

In a linear system described by the differential equation:

$$y'(t) + y(t) = kx(t) \quad [9]$$

and its corresponding transfer function in the frequency domain described above:

$$H(s) = \frac{k}{s+1} \quad [10]$$

The parameter k, this represents the system gain, a proportionality factor that directly affects the amplitude of the system's response to a given input.

When the input is a unit step, that is, $x(t) = u(t)$, The output in the time domain is expressed as:

$$y(t) = k(1 - e^{-t})u(t) \quad [11]$$

The response to the unit step input is an increasing exponential function that asymptotically approaches the value of *k*.

Magnetic Field

The magnetic field transfer function is expressed as:

$$H(s) = \frac{200}{s+1} \quad [12]$$

In this case, the constant value of 200 in the numerator reflects the strength of the magnetic field generated per unit of input signal (current applied to the electromagnet, for example). Physically, an increase in this value would indicate a stronger magnetic field, which would increase control over the flow of charged particles in the propellant. A higher value of *k* This would imply a higher field density for the same current.

A lower value would reduce the magnetic control over the particles.

The time output for equation (2.16) is:

$$y(t) = 200(1 - e^{-t})u(t) \quad [13]$$

Therefore, the effects of this change in the numerator of the transfer function are:

- The final amplitude of the system changes from *k* to 200.
- The system continues to reach 63% of its final value in approximately one second (time constant), since this constant depends on the denominator (s+1).
- It is an exponentially increasing response that asymptotically reaches 200.

Voltage

However, we now have a second-order transfer function that expresses the voltage given by:

$$H(s) = \frac{2000}{s^2 + s + 1} \quad [14]$$

The presence of s2 in the denominator significantly modifies the system's behavior compared to the previous case.

If we compare it to the standard model of a second-order system:

$$H(s) = \frac{K}{s^2 + 2\zeta\omega_n s + \omega_n^2} \quad [15]$$

Here, the constant of 2000 in the numerator represents the gain in particle acceleration when a control signal is applied.

ISSN: 2523-6865
RENIECYT-SECIHTI: 1702902

Aburto–Policarpo Gethsi, Castillo-Sánchez Martín and López-Cárdenas Rodrigo [2025]. Dynamic control analysis by simulation of the main components of a Hall Effect thruster. Journal Computational Simulation. 9[20] 1-17: e20920117
https://doi.org/10.35429/JCS.2025.9.20.2.1.17

This results in a higher ejection velocity, and therefore, greater thrust from the propellant. Increasing k implies a more powerful acceleration of the particles, increasing the thrust.

Reducing k would decrease acceleration effectiveness.

We can observe that:

- The profit is represented by the numerator, that is, k =2000.
- The denominator contains the terms corresponding to the damping coefficients (ζ) and the natural frequency (ω_n).

The parameter k in each block of the system defines the direct relationship between the input signal and the physical response of the component:

- In the injector: determines the mass flow.
- In the magnetic field: it regulates the field intensity.
- In tension: it controls the acceleration of particles.

Proper adjustment of this parameter allows for optimization of the performance of the electric propulsion system in terms of efficiency and thrust.

PID Control

The objective of any control system is, given a certain system and a certain amount of information available based on a series of measurements of some of its signals, to try to determine certain feasible control inputs so that the system variable to be controlled follows a certain reference signal as exactly as possible, despite the influence of possible disturbances, measurement errors, and variations in the system load. (Moreno, L. 2003).

Figure 4 shows a general process control scheme G_p (the process G_p refers to the transfer function that represents the dynamics of a physical system that is to be controlled), where:

r: is the control reference
u: is the control signal
y: is the output of the control system

Box 4

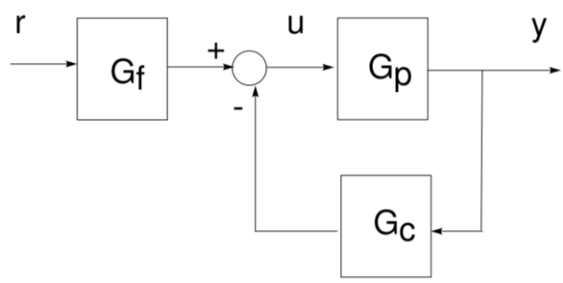

Figure 4
Block diagram of a general control scheme (Adapted from Moreno, L. 2003)

In this scheme, the control signal is:

$$U(s) = G_f(s)R(s) - G_C(s)Y(s) \quad [16]$$

A portion of the control signal formed by a controller can be seen.G_C located in the feedback loop and another by a filter G_f at the system entrance (García H. 2010). To obtain the transfer function, we have:

$$Y(s) = U(s)G_p(s)$$
$$U(s) = G_f(s)R(s)G_p(s) - G_C(s)Y(s)G_p(s)$$
$$Y(s)[1 + G_C(s)G_p(s)] = G_f(s)R(s)G_p(s)$$

The control scheme in Figure 4, has the following expression for the joint transfer function of the entire system: (Moreno, L. 2003)

$$\frac{Y(s)}{R(s)} = G_f(s)\frac{G_p(s)}{1 + G_p(s)G_c(s)} \quad [17]$$

In this expression, it can be observed that the filtering termG_f it directly affects the steady-state gain of the feedback system, as well as its poles and zeros, since it is located in the main chain before the feedback loop. However, it does not alter the positions of the poles and zeros of the feedback loop, except in the case of pole-zero cancellations between G_f and the feedback loop transfer function.

On the other hand, the termG_c, being located in the feedback loop significantly affects the positions of the poles in the closed-loop system, substantially altering the system's dynamics. To simplify somewhat, one can think that while with the design of G_f We seek to improve or adjust the steady-state response of the system, with G_c the aim is to adjust the transient response (Moreno, L. 2003).

ISSN: 2523-6865
RENIECYT-SECIHTI: 1702902

Aburto–Policarpo Gethsi, Castillo-Sánchez Martín and López-Cárdenas Rodrigo [2025]. Dynamic control analysis by simulation of the main components of a Hall Effect thruster. Journal Computational Simulation. 9[20] 1-17: e20920117
https://doi.org/10.35429/JCS.2025.9.20.2.1.17

A particular case of this control structure occurs when $G_f = G_c$. In this case, design freedom is reduced since only one transfer function is available. Therefore, the control scheme is simplified to that shown in diagram (a) of Figure 5, and can also be expressed using the equivalent diagram (b).

Box 5

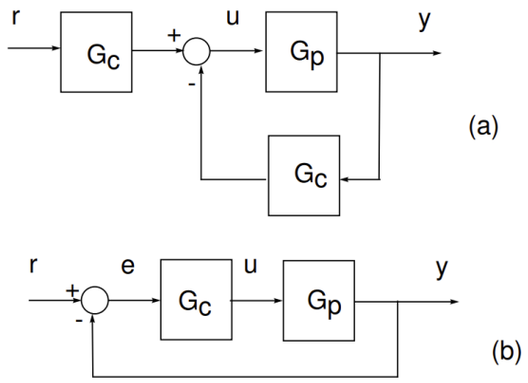

Figure 5
Controller in the main loop (Adapted from Moreno, L. 2003)

This equivalent scheme (b) is what can be called the classic control scheme. PID control is included within this group of controllers. (García H. 2010).

The PID (Proportional-Integral-Derivative) controller is the most widely implemented control algorithm in industry. The vast majority of feedback loops operate under this scheme or one of its adaptations. Its implementation can take various forms, either as a standalone unit or as an integral part of more complex systems, such as Direct Digital Control (DDC) or hierarchical distributed control architectures. (Åström K. 2009).

Despite advances in more complex control strategies, PID control remains fundamental in the basic stage of many industrial processes. In fact, in numerous cases, it is still the most widely used technique due to its effectiveness and versatility. (Moreno, L. 2003).

The PID algorithm

The PID algorithm can be written as:

$$u(t) = K\left[e(t) + \frac{1}{T_i}\int_0^t e(\tau)d\tau + T_d\frac{de(t)}{dt}\right] \quad [18]$$

Where u is the control signal and e is the control error ($e = y_{sp} - y$).

The control signal is thus a sum of three terms: the P-term (which is proportional to the error), the I-term (which is proportional to the integral of the error), and the D-term (which is proportional to the derivative of the error). The controller parameters are the proportional gain. K, the integral time T_i, and derivative time T_d. (Åström K. 2009).

It can be observed that if the integral time constant becomes infinite, the integral action disappears, and if the derivative time constant becomes zero, the derivative action disappears.

The transfer function of the PID controller is as follows: (Moreno, L. 2003).

$$\frac{U(s)}{E(s)} = K\left(1 + \frac{1}{T_i s} + T_d s\right) = \frac{K(1 + sT_i + s^2T_iT_d)}{sT_i} \quad [19]$$

In this controller, the adjustment aims to determine the positions of the two zeros of the transfer function and its static gain, so that the desired design specifications of the system are met as closely as possible (Moreno, L. 2003). A real PID controller will have the following form:

$$G_c(s) = K\frac{1 + sT_i + s^2T_iT_d}{(1 + sT_i)(1 + sT_d)} \quad [20]$$

The regulator parameters can be adjusted in two ways:

1. Empirically

This involves experimentally adjusting the values until the desired response is achieved. This method can be excessively slow in many systems, especially if the response time is long. To avoid this problem, Ziegler-Nichols methods are used. Based on very simple measurements observed in the system's response, these methods provide theoretical values for the controller parameters. These values are taken as a reference, and further fine-tuning is then performed from them. These methods, and others derived from them, are widely used in industry, both for purely manual tuning and in industrial PID controllers with self-tuning systems.

ISSN: 2523-6865
RENIECYT-SECIHTI: 1702902

Aburto–Policarpo Gethsi, Castillo-Sánchez Martín and López-Cárdenas Rodrigo [2025]. Dynamic control analysis by simulation of the main components of a Hall Effect thruster. Journal Computational Simulation. 9[20] 1-17: e20920117
https://doi.org/10.35429/JCS.2025.9.20.2.1.17

2. Theoretically

This involves analytically determining the regulator values. It requires explicit knowledge of the process transfer function (Moreno, L. 2003).

Proportional Action

In the case of pure proportional control, the control law given by Equation 9 reduces to:

$$u(t) = Ke(t) + u_b \quad [21]$$

The control action is simply proportional to the control error. The variableu_b It's a polarization or a reset. When the control error e is zero, the control signal takes the value u(t) = u_b. Polarization u_b often fixes on ($u_{max} + u_{min}$)/2, but it can sometimes be manually adjusted so that the steady-state control error is zero at a given setpoint (Åström K. 2009).

Integral Action

The primary function of integral action is to ensure that the process output matches the setpoint at steady state. With proportional control, there is normally a steady-state control error. With integral action, a small positive error will always lead to an increasing control signal, and a negative error will result in a decreasing control signal, regardless of the error's size. The following simple argument shows that the steady-state error will always be zero with integral action. Assume the system is at steady state with a constant control signal (u_0) and a constant error (e_0). It follows from Equation 22 that the control signal is then given by:

$$u_0 = K\left(e_0 + \frac{e_0}{T_i}t\right) \quad [22]$$

While $e_0 \neq 0$, this clearly contradicts the hypothesis that the control signal u_0 is constant. A controller with integral action will always give zero error in steady state (Åström K. 2009).

Derivative Action

The objective of derivative action is to improve closed-loop stability. The instability mechanism can be described as follows.

Due to the dynamics of the process, it will take some time before a change in the control variable is detectable at the process output. Thus, the control system will take time to correct an error. The action of a proportional-derivative controller can be interpreted as if the control were made proportional to the predicted process output, where the prediction is made by extrapolating the error along the tangent to the error curve. The basic structure of a PD controller is:

$$u(t) = K\left(e(t) + T_d\frac{de(t)}{dt}\right) \quad [23]$$

The control signal is thus proportional to an estimate of the control error at time T_d forward, where the estimate is obtained by linear extrapolation. (Åström K. 2009. Kuo B. 1996).

Simulation of the Hall effect propulsion system in Simulink®

To simulate the different types of controllers that can be used, we employ a tool provided by Simulink® called PID Tuner. The PID Tuner app automatically adjusts the gains of a PID controller for a SISO (Single-Input Single-Output) plant to achieve a balance between performance and robustness.

This tool allows you to specify the controller type, such as PI controllers, PID controllers with a derivative filter, or PID controllers with two degrees of freedom (2-DOF). The analysis graphs allow you to examine controller performance in both the time and frequency domains. You can interactively fine-tune controller performance by adjusting loop bandwidth and phase margin, or by improving setpoint tracking or disturbance suppression.

We use PID Tuner with a plant represented by a numerical LTI model, such as a transfer function (tf) or a state-space model (ss). With Simulink® Control Design™ software, we use PID Tuner to tune a PID Controller or PID Controller (2DOF) block in a Simulink model. Using System Identification Toolbox™ software, the app can be used to estimate a plant from measured or simulated data and design a controller for the estimated plant.

ISSN: 2523-6865
RENIECYT-SECIHTI: 1702902

Aburto–Policarpo Gethsi, Castillo-Sánchez Martín and López-Cárdenas Rodrigo [2025]. Dynamic control analysis by simulation of the main components of a Hall Effect thruster. Journal Computational Simulation. 9[20] 1-17: e20920117
https://doi.org/10.35429/JCS.2025.9.20.2.1.17

This tool simulates P, I, D, PI, PD, and PID controls in that order for each transfer function related to the components of the Hall effect impeller, with the first simulated component being the magnetic field generated by a coil, followed by the voltage, and finally the injector.

Simulink components and functions used in the test simulation

For each simulation, the PID controller is first tuned. To perform this tuning and test the different controllers, various functions and tools provided by Simulink are needed, such as input and disturbance components, transfer function, and scope (visualizer), among others, which are presented below.

Unit step function

A unit step function is a mathematical function that is activated at time t = 0 and is represented by the values 1 for $t \geq 0$ and 0 for $t < 0$. It is commonly used to represent an idealized switch and can be multiplied by other functions to activate them at t = 0.

PID controller

This tool is a tuner that automatically adjusts the gains of a PID controller.

Transfer Function

In MATLAB™, a transfer function is a mathematical representation that describes the relationship between the input and output of a linear time-invariant system, especially in the context of control system analysis. It is used to model and analyze the behavior of physical systems.

$$\frac{1}{s+1} \qquad [24]$$

Scope (displayer)

A scope (oscilloscope or signal viewer) is a visual tool that allows you to observe and analyze data, especially real-time signals, during the execution of a model or program.

Sum Block

In Simulink, a Sum block is a fundamental component that performs addition or subtraction operations on its input signals. This block can handle scalar, vector, or matrix inputs and allows the addition or subtraction of these inputs.

Signal editor

The signal editor is a tool that allows you to create, edit, and manage signal scenarios for use in simulation models. It allows you to define groups of signals with different configurations and apply them to models for various simulations or tests.

PID Control Tuning

Arrangement of components for tuning

Initially, we arranged the unit step, summing point, PID controller, transfer function, and scope blocks as shown in Figure 6.

Box 6

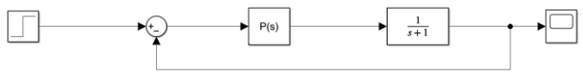

Figure 6
Control system for performing transfer function tuning

We click on our PID tuner block, which opens a window like the one shown, where we have the option to select the type of controller we want to tune. We select a P controller. Once the controller is selected, we select the "Apply" button to confirm the control, and then "Tune," which will tune the controller for the proposed transfer function (Figure 7).

Box 6

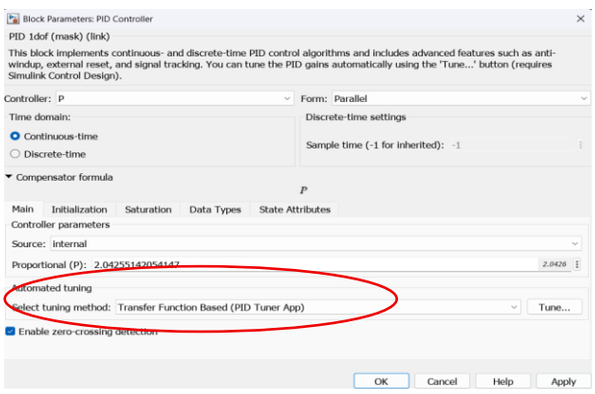

Figure 7
Controller selection, application, and tuning

ISSN: 2523-6865
RENIECYT-SECIHTI: 1702902

After selecting "Tune," a process will begin that, upon completion, will display a window where Simulink will have selected the appropriate signal response parameters. Next, select the "Update Blocks" button, which will update the P, I, and D parameters (depending on the selected control) in the controller. Once this is done, you can close this window, and you will see that the control parameters have been updated (Figures 8 and 9).

Box 8

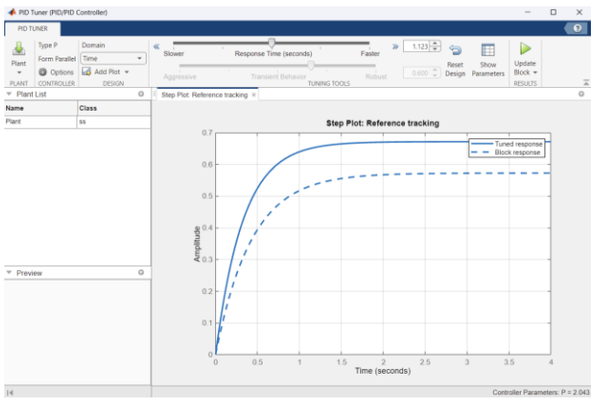

Figure 8
Tuning and application of tuning parameters

Once this process has been followed, our control block is ready to be tested with a reference signal and disturbances. (Moore H. 2007. Cubillos M. 2003).

Box 9

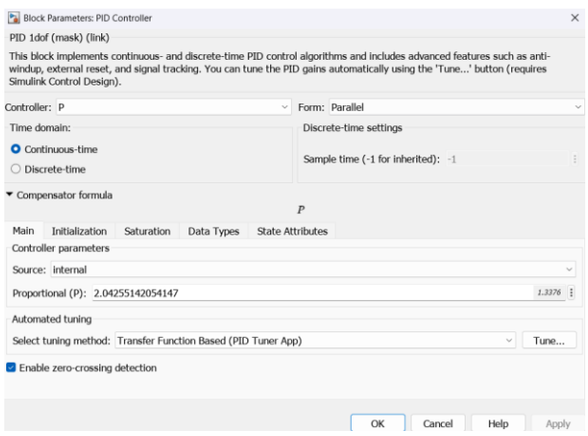

Figure 9
Definition of the Proportional, Integral and/or Derivative parameters

Results

Magnetic Field Simulation
P-Control for the Magnetic Field

Box 10

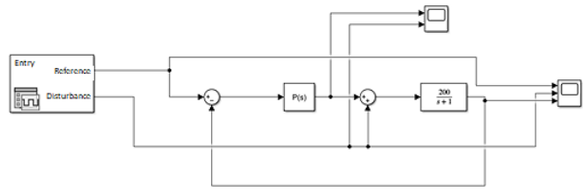

Figure 10
P control system for the magnetic field

Box 11

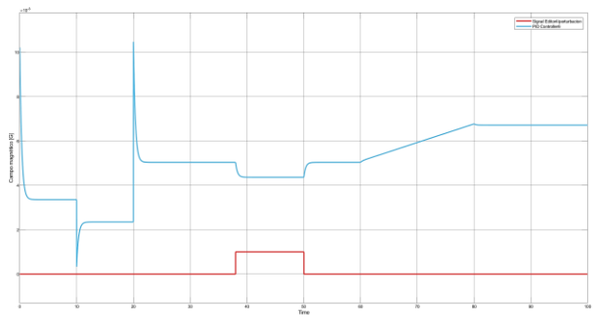

Figure 11
Graph of the perturbation response of the P controller tuned for the magnetic field

Box 12

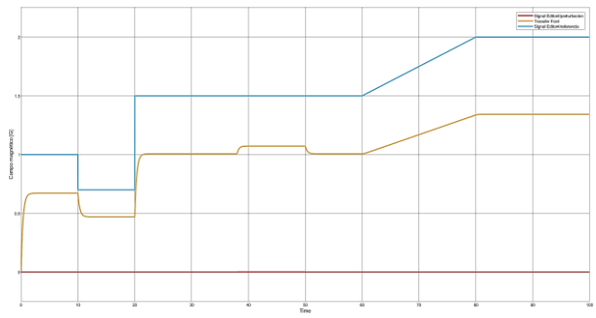

Figure 12
Graph of the magnetic field response with respect to the controller reference P

Control I for the magnetic field

Box 13

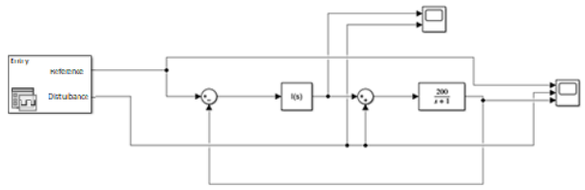

Figure 13
Control system I for the magnetic field

ISSN: 2523-6865
RENIECYT-SECIHTI: 1702902

Aburto–Policarpo Gethsi, Castillo-Sánchez Martín and López-Cárdenas Rodrigo [2025]. Dynamic control analysis by simulation of the main components of a Hall Effect thruster. Journal Computational Simulation. 9[20] 1-17: e20920117
https://doi.org/10.35429/JCS.2025.9.20.2.1.17

Box 14

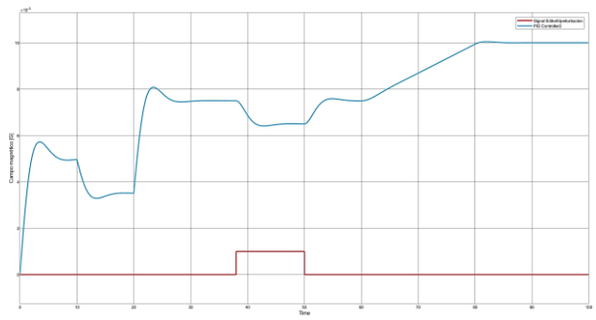

Figure 14

Graph of the disturbance response of the tuned controller I for the magnetic field

Box 15

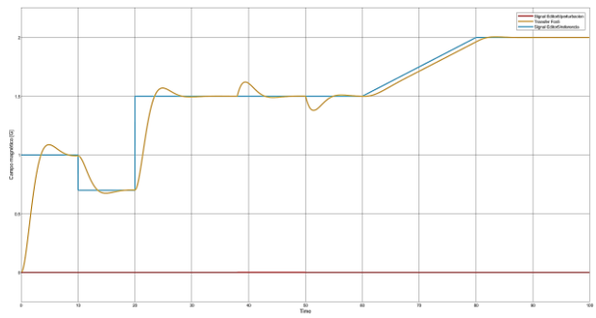

Figure 15

Graph of the magnetic field response with respect to the controller reference I.3.3.3 Control

PI for the magnetic field

Box 16

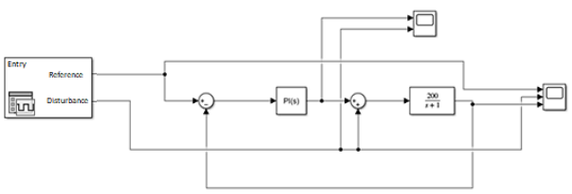

Figure 16

PI control system for the magnetic field

Box 17

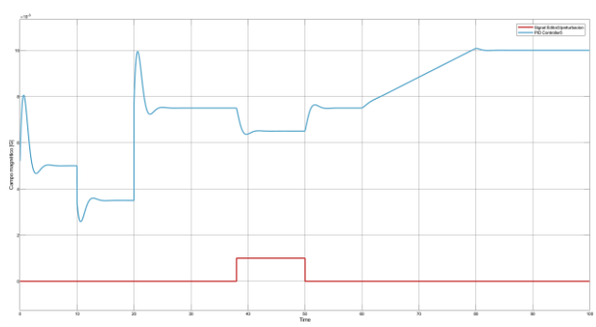

Figure 17

Graph of the disturbance response of the PI controller tuned for the magnetic field

Box 18

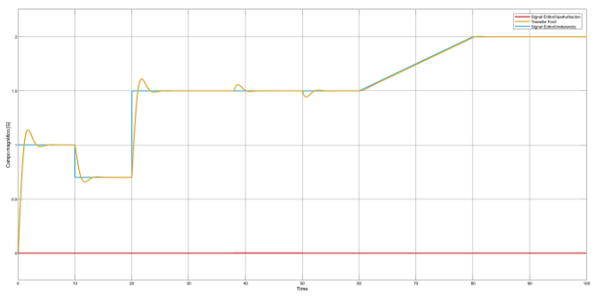

Figure 18

Graph of the magnetic field response with respect to the PI controller reference

Control for the Magnetic Field

Box 19

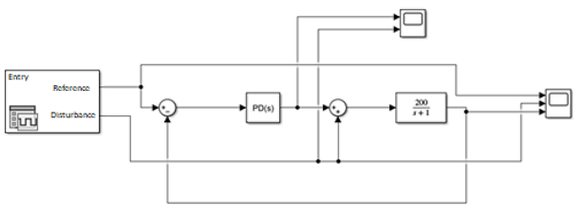

Figure 19

PD control system for the magnetic field

Box 20

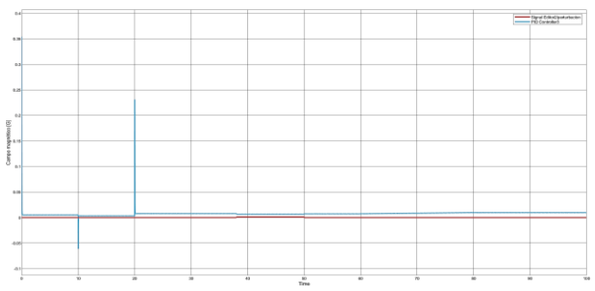

Figure 20

Graph of the disturbance response of the PD controller tuned for the magnetic field

Box 21

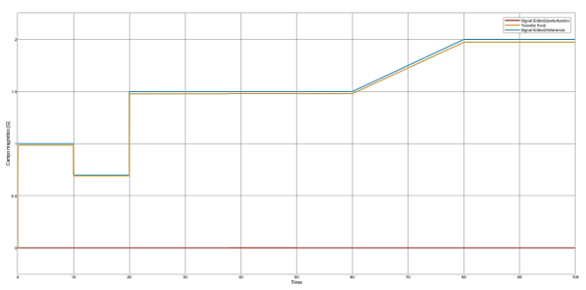

Figure 21

Graph of the magnetic field response with respect to the PD controller reference

ISSN: 2523-6865
RENIECYT-SECIHTI: 1702902

Aburto–Policarpo Gethsi, Castillo-Sánchez Martín and López-Cárdenas Rodrigo [2025]. Dynamic control analysis by simulation of the main components of a Hall Effect thruster. Journal Computational Simulation. 9[20] 1-17: e20920117
https://doi.org/10.35429/JCS.2025.9.20.2.1.17

PID control for the magnetic field

Box 22

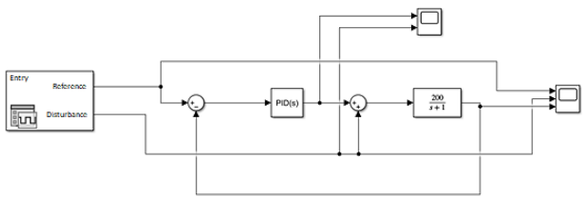

Figure 22
PID control system for the magnetic field

Box 23

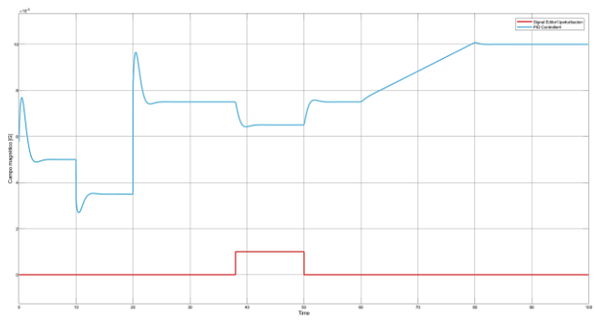

Figure 23
Graph of the disturbance response of the PID controller tuned for the magnetic field

Box 24

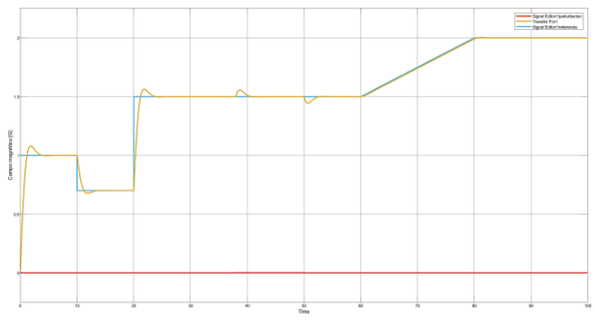

Figure 24
Graph of the magnetic field response with respect to the PID controller reference

Voltage Simulation
Voltage Control (P)

Box 25

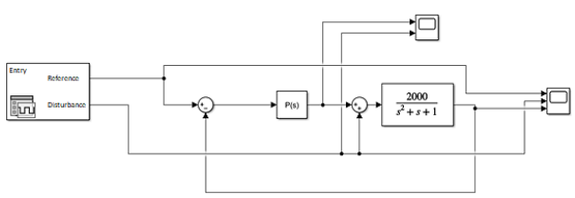

Figure 25
P control system for voltage

Box 26

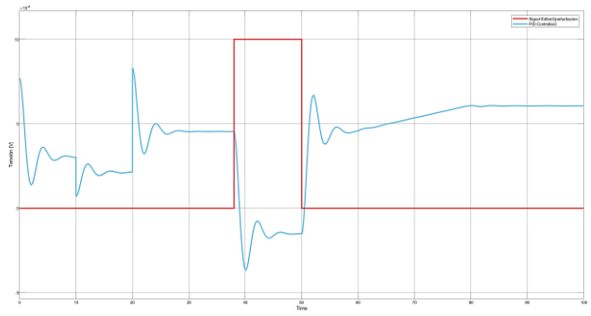

Figure 26
Graph of the disturbance response of the P controller tuned for voltage.

Box 27

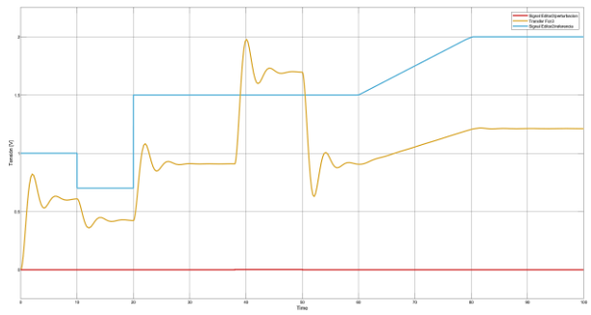

Figure 27
Graph of the voltage response with respect to the controller reference P

Voltage Control I

Box 28

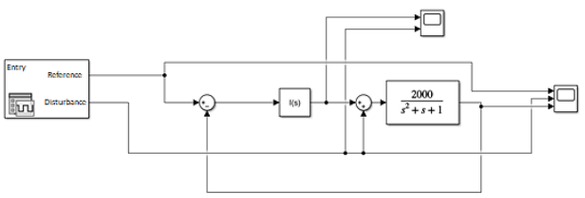

Figure 28
Control System I for voltage

Box 29

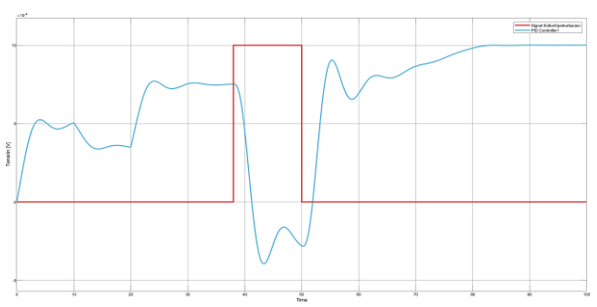

Figure 29
Graph of the disturbance response of the tuned I controller for voltage

ISSN: 2523-6865
RENIECYT-SECIHTI: 1702902

Box 30

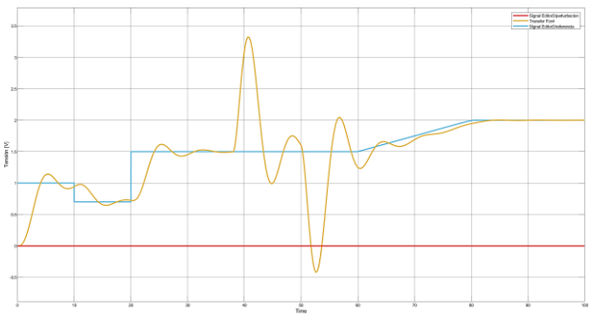

Figure 30
Graph of the voltage response with respect to the controller reference I

PI Voltage Control

Box 31

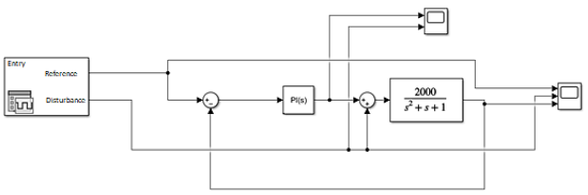

Figure 31
PI control system for voltage

Box 32

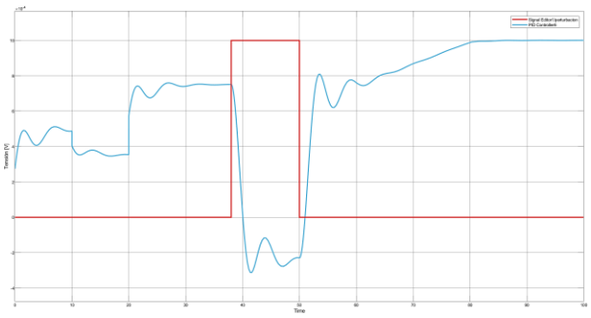

Figure 32
Graph of the disturbance response of the PI controller tuned for voltage.

Box 33

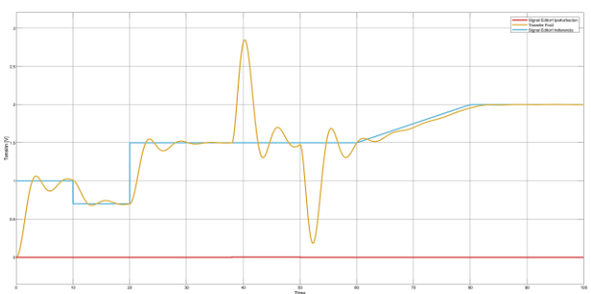

Figure 33
Graph of the voltage response with respect to the PI controller reference

PD Voltage Control

Box 34

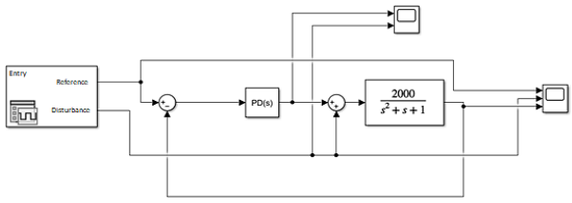

Figure 34
PD control system for voltage

Box 35

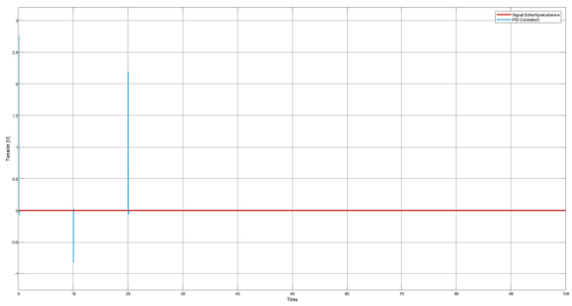

Figure 35
Graph of the disturbance response of the PD controller tuned for voltage

Box 36

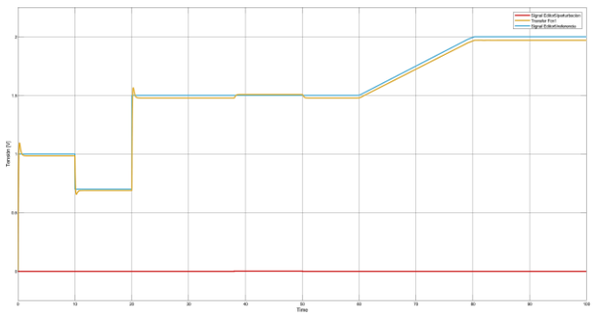

Figure 36
Graph of the voltage response with respect to the PD controller reference

PID Voltage Control

Box 37

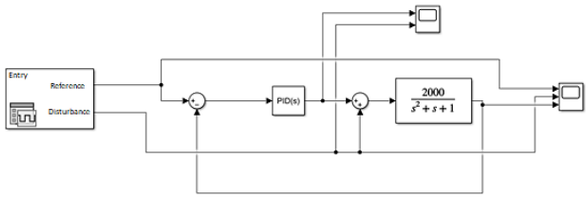

Figure 37
PID control system for voltage

ISSN: 2523-6865
RENIECYT-SECIHTI: 1702902

Aburto–Policarpo Gethsi, Castillo-Sánchez Martín and López-Cárdenas Rodrigo [2025]. Dynamic control analysis by simulation of the main components of a Hall Effect thruster. Journal Computational Simulation. 9[20] 1-17: e20920117
https://doi.org/10.35429/JCS.2025.9.20.2.1.17

Box 38

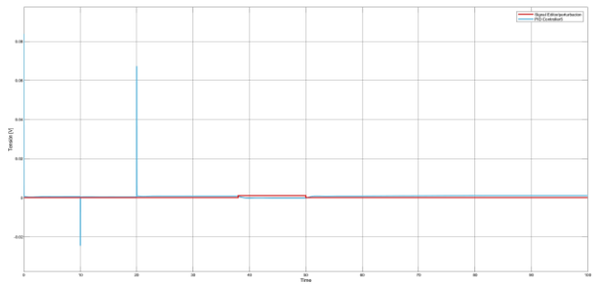

Figure 38
Graph of the disturbance response of the PID controller tuned for voltage

Box 39

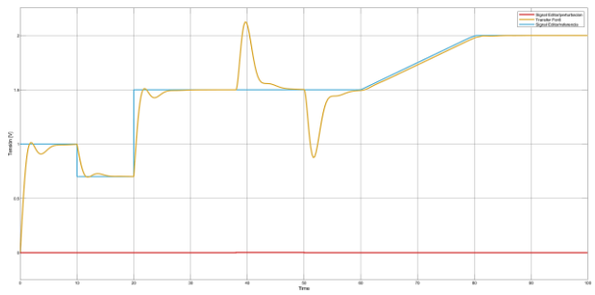

Figure 39
Graph of the voltage response with respect to the PID controller reference.

Injector Simulation

Injector P Control

Box 40

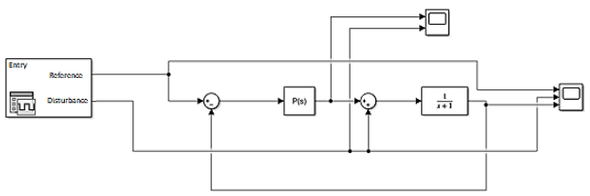

Figure 40
P control system for the injector

Box 41

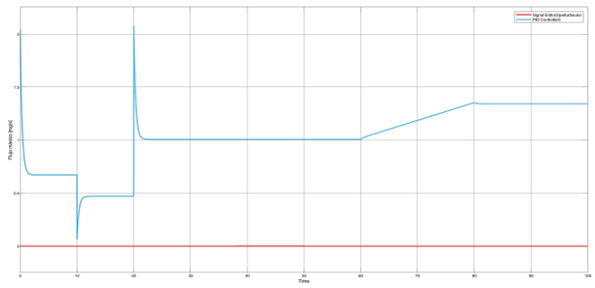

Figure 41
Graph of the disturbance response of the tuned P controller for the injector

Box 42

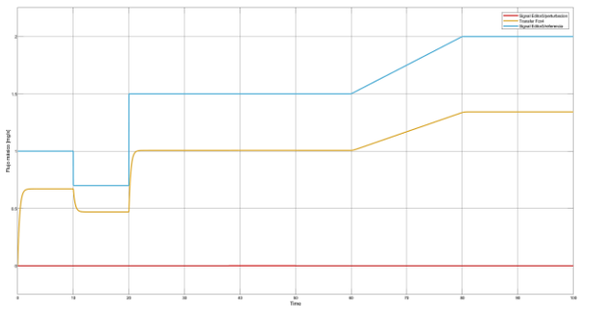

Figure 42
Graph of the injector response with respect to the controller reference P

Control I for the injector

Box 43

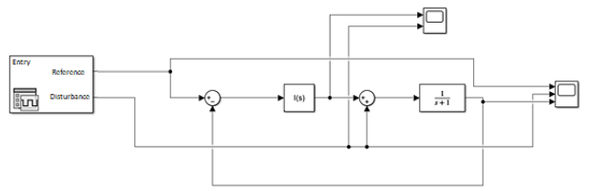

Figure 43
Control system I for the injector

Box 44

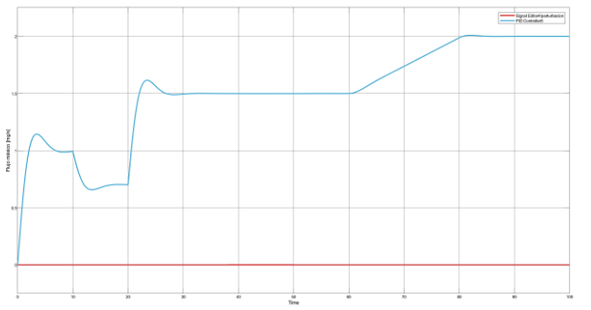

Figure 44
Graph of the disturbance response of the tuned controller I for the injector

Box 45

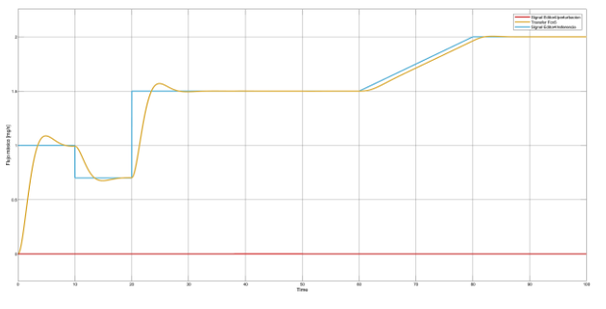

Figure 45
Graph of the injector response with respect to the controller reference I

ISSN: 2523-6865
RENIECYT-SECIHTI: 1702902

Aburto–Policarpo Gethsi, Castillo-Sánchez Martín and López-Cárdenas Rodrigo [2025]. Dynamic control analysis by simulation of the main components of a Hall Effect thruster. Journal Computational Simulation. 9[20] 1-17: e20920117
https://doi.org/10.35429/JCS.2025.9.20.2.1.17

PI Control for the Injector

Box 46

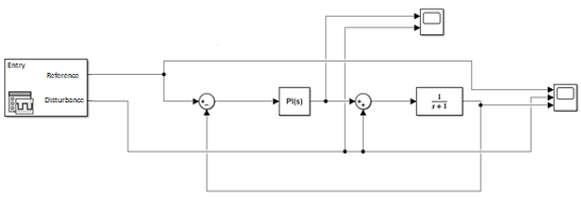

Figure 46
PI control system for the injector

Box 47

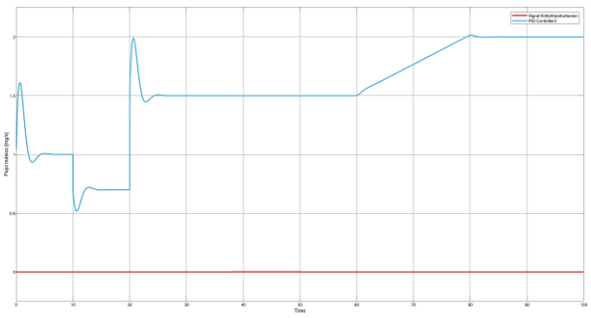

Figure 47
Graph of the disturbance response of the tuned PI controller for the injector

Box 48

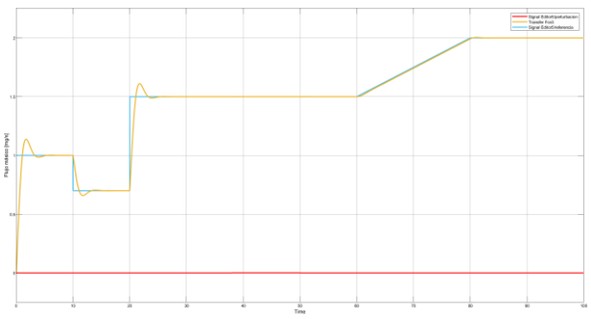

Figure 48
Graph of the injector response with respect to the PI controller reference

Control for the Injector

Box 49

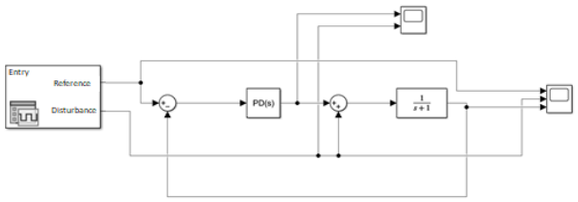

Figure 49
PD control system for the injector

Box 50

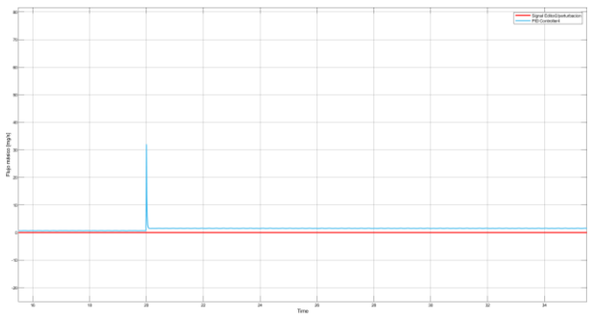

Figure 50
Graph of the disturbance response of the tuned PD controller for the injector

Box 51

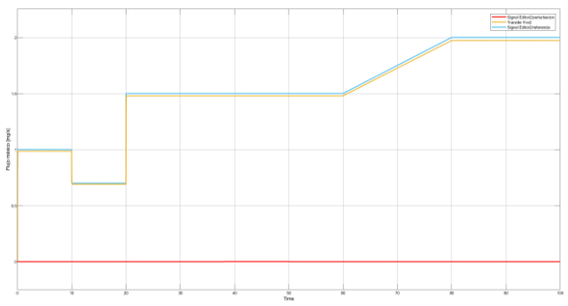

Figure 51
Graph of the injector response with respect to the PD controller reference

Control for the Injector

Box 52

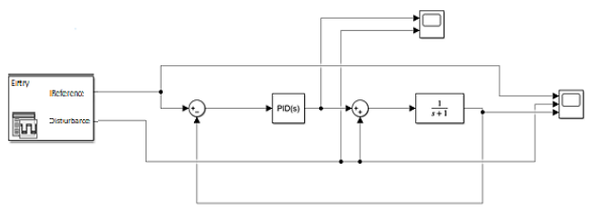

Figure 52
PID control system for the injector

Box 53

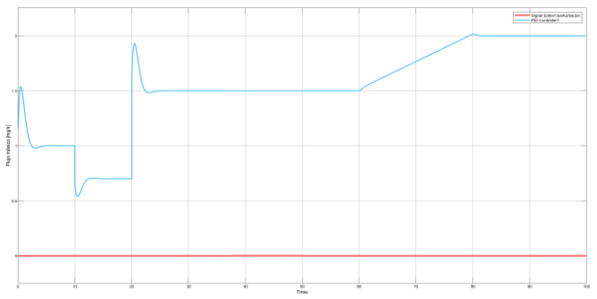

Figure 53
Graph of the disturbance response of the tuned PID controller for the injector

ISSN: 2523-6865
RENIECYT-SECIHTI: 1702902

Aburto–Policarpo Gethsi, Castillo-Sánchez Martín and López-Cárdenas Rodrigo [2025]. Dynamic control analysis by simulation of the main components of a Hall Effect thruster. Journal Computational Simulation. 9[20] 1-17: e20920117
https://doi.org/10.35429/JCS.2025.9.20.2.1.17

Box 54

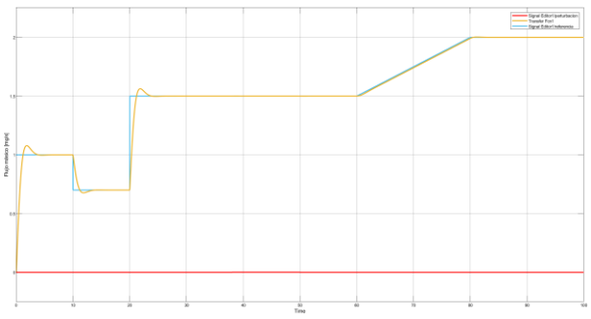

Figure 54
Graph of the injector response with respect to the PID controller reference

Results Analysis

Using the transfer equation developed by Sánchez J. (2015) in the simulation.

Based on the behavior shown in the graphs presented in the simulation for the magnetic field, we can highlight the PD, PI, and PID controllers, whose resulting behaviors most closely matched the reference signals proposed for testing the controller. However, it is also important to note that the PD controller, shown in Figure 20, exhibits a very abrupt change in its magnetic field levels within a very short time interval. Therefore, it can be deduced that this behavior is physically unachievable, and thus, attempting to implement this controller is not viable.

Regarding voltage, the simulations show efficient control in the PD and PID controllers, although they may present difficulties for physical implementation due to the sudden changes in voltage levels over a very short period of time. In contrast, the PI controller shown in Figure 32, although it exhibits irregular behavior, remains close to the reference, making physical implementation possible.

In the case of the injector, the I, D, PI, and PD controllers show behavior consistent with their respective references, making them acceptable. However, it should be noted that the PD controller cannot be implemented because it is physically impossible to make the injector re-enter the fuel. Therefore, only the I, D, and PI controllers are the most viable options for implementation.

Conclusions

Based on the simulation results, we can conclude that PI and PID controllers are best suited for regulating magnetic fields due to their precise reference tracking, unlike PD controllers, whose abrupt changes make them physically impractical. Regarding voltage control, PI controllers stand out for their balance between efficiency and physical feasibility, while PD and PID controllers, although acceptable, exhibit excessively rapid variations that hinder their practical implementation.

For the injector, the I, D, and PI controllers are the most viable, as they achieve good reference tracking without requiring physically unfeasible behaviors, such as fuel return in the case of the PD controller.

In summary, the PI controller emerges in this study as the most robust and realistic option for the three applications analyzed, combining accuracy, stability, and physical feasibility. However, in scenarios where faster tuning is prioritized, the PID controller could be considered, provided its practical limitations are evaluated.

Statements

Conflict of interest

The authors declare no conflict of interest. They have no competing financial interests or known personal relationships that could have influenced the article presented here.

Contribution per author

Aburto-Policarpo. Gethsi: Research; Writing - original draft.

Castillo-Sánchez, Martín: Conceptualization; Writing - revision and editing.

López-Cárdenas, Rodrigo: Methodology; Visualization; Data curation.

Acknowledgments

The authors thank the Instituto Politécnico Nacional and to the Escuela Superior de Ingeniería Mecánica y Eléctrica, Unidad Zacatenco the support provided for carrying out this research.

ISSN: 2523-6865
RENIECYT-SECIHTI: 1702902

Aburto–Policarpo Gethsi, Castillo-Sánchez Martín and López-Cárdenas Rodrigo [2025]. Dynamic control analysis by simulation of the main components of a Hall Effect thruster. Journal Computational Simulation. 9[20] 1-17: e20920117
https://doi.org/10.35429/JCS.2025.9.20.2.1.17

Abbreviations

DDC Direct Digital Control
DOF Degrees of Freedom
EP Electric Propulsion
HET Hall Effect Propulsion
PID Proportional-Integral-Derivative Control
SISO Single-Input Single-Output

References

Background

Goebel, D. M., & Katz, I. (2008). *Fundamentals of electric propulsion: Ion and Hall thrusters*. JPL Space and Technology Series.

Hey, F. G. (2018). Electric propulsion fundamentals. En *Micro Newton Thruster Development*. Springer Vieweg.

Moreno, L., & Castañeda, B. S. G. (2003). *Ingeniería de control: Modelado, análisis y control de sistemas* (1ª ed.). Ariel. México.

Basic

Lev, D., Kroes, R. L., Martinez-Sanchez, M., & Keidar, M. (2019). The technological and commercial expansion of electric propulsion. *Acta Astronautica, 159*, 213–227. https://doi.org/10.1016/j.actaastro.2019.03.043

ESA. (2002, julio). Electric propulsion systems programmes. Agencia Espacial Europea.

Hey, F. G. (2018). Electric propulsion fundamentals. En *Micro Newton Thruster Development*. Springer Vieweg.

Oh, B., & McAndrew, C. (2023). Design, fabrication, and testing of an undergraduate Hall effect thruster. *Journal of Electric Propulsion, 2*(6).

Poonam Tripathy (2020). Overview on electric propulsion systems. *International Journal of Scientific and Research Publications,* Volume 10, Issue 12, December 2020 422 ISSN 2250-3153.

Support

Åström, K. J., & Hägglund, T. (2009). *Control PID avanzado*. Pearson Educación.

Cubillos, M. F. (2003). *Apuntes: Introducción a Simulink. www.labcontrol.cl* DOI: 10.1002/9780470436448

García, H. M. S. (2010). *Sintonización del regulador automático de voltaje del sistema de control Basler DECS 125-15 en Micromáquinas Síncronas* [Tesis profesional, IPN, México].

Moore, H. (2007). *MATLAB para ingenieros* (1ª ed.). Pearson Educación.

Jiles, D. (2001). *Electronic properties of materials*. Nelson Thornes Ltd. https://doi.org/10.1201/9781315273365

Sánchez, J. E. M. (2015). *Diseño de un sistema de control para el propulsor Hall del microsatélite Quetzal* [Tesis de licenciatura, UNAM, México].

Differences

Sánchez, J. E. M. (2015). *Diseño de un sistema de control para el propulsor Hall del microsatélite Quetzal* [Tesis de licenciatura, UNAM, México].

ISSN: 2523-6865
RENIECYT-SECIHTI: 1702902

Aburto–Policarpo Gethsi, Castillo-Sánchez Martín and López-Cárdenas Rodrigo [2025]. Dynamic control analysis by simulation of the main components of a Hall Effect thruster. Journal Computational Simulation. 9[20] 1-17: e20920117
https://doi.org/10.35429/JCS.2025.9.20.2.1.17

Journal Computational Simulation 9[20]1-11: e30920111
Article

Parametric analysis of dynamic wave-seabed interaction

Análisis parámetrico de la interacción dinámica oleaje-suelo marino

Peza-Ortiz, Edebaldo[a], Arcos-Hernández, Emmanuel*[b], García-Trinidad, Enrique[c] and Torres-Valle, José[d]

[a] Universidad Tecnológica Fidel Velázquez • 3345-2022 • 0000-0003-0236-883X• 778771
[b] Universidad Tecnológica Fidel Velázquez • 1933-2025 • 0000-0002-3404-1375 • 349835
[c] Universidad Tecnológica Fidel Velázquez • 9353-2024 • 0000-0003-2875-0500 • 271440
[d] Universidad Tecnológica Fidel Velázquez • 6499-2025 • 0000-0001-8258-9418 • 626539

SECIHTI classification:

Area: Engineering
Field: Engineering
Discipline: Civil Engineering
Subdiscipline: Marine Engineering

https://doi.org/10.35429/JCS.2025.9.20.1.11
Article History:
Received: June 30, 2025
Accepted: December 20, 2025

* ✉ [earcosh361@hotmail.com]

Abstract

In this work is present an analysis of the response of the pore pressure induced by long waves of water. This phenomenon has been widely studied in the literature specialized in physical variables, being somewhat complicated to identify which are the dominant variables that significantly change the pore pressure, so the contribution of the present work is to do it in a dimensionless model to obtain dimensionless parameters that group the physical variables of the soil and the waves. The results show that long waves present greater pressure in the pore than short waves.

Parametric analysis of dynamic wave-seabed interaction		
Objetives	Methodology	Contribution
The main objective of this study is to establish a dimensionless mathematical model to determine the dynamic response of pore pressure in terms of dimensionless parameters. These parameters include various combinations of physical wave variables such as wavelength, water depth, wave frequency, and, for the seafloor, permeability, porosity, modulus of strength, and volumetric deformation of the soil.	The methodology is based on the formulation of Biot's quasi-static equation. Starting from the characteristic values identified by Arcos, Bautista, & Mendez, 2016, the system of equations was dimensionless, resulting in dimensionless parameters that group the physical variables of the waves and seafloor. The analytical solution was compared with solutions reported in the specialized literature.	The analytical solutions reported in the specialized literature are based on an analysis of physical variables, making the mathematical study difficult to identify the most representative variables in the pore pressure response. Creating a dimensionless model allows for the creation of dimensionless parameters that involve combinations of physical variables, achieving a better physical understanding of the soil deformation affected by water waves.

Water waves, poro-elastic seabed, Parametric analysis

Resumen

En este trabajo se presenta un análisis de la respuesta de la presión de poro inducida por ondas largas de agua. Este fenómeno ha sido estudiado ampliamente en la literatura especializada en variables físicas, siendo un tanto complicado identificar cuales son las variables dominantes y que cambian significativamente la presión de poro, por lo que la contribución del presente trabajo es hacerlo de forma adimensional para obtener parámetros adimensionales que agrupan las variables físicas del suelo y del oleaje. Los resultados muestran que las ondas largas presentan una mayor presión en el poro que ondas cortas.

Análisis parámetrico de la interacción dinámica oleaje-suelo marino		
Objetivos	Metodología	Contribución
El objetivo principal de este estudio es establecer un modelo matemático adimensional para determinar la respuesta dinámica de la presión de poro en términos de parámetros adimensionales. Los parámetros incluyen varias combinaciones de las variables físicas del oleaje como son la longitud de onda, profundidad del agua, frecuencia del oleaje y para el suelo marino corresponden la permeabilidad, porosidad, modulo de resistencia, deformación volumétrica del suelo.	La metodología se basa en la formulación de la ecuación cuasi-estática de Biot. Partiendo de los valores característicos identificados por Arcos, Bautista, & Mendez, 2016, se adimensionalizo el sistema de ecuaciones, surgiendo parámetros adimensionales que agrupan las variables físicas del oleaje y suelo marino. La solución analítica se comparó con soluciones reportadas en la literatura especializada.	La soluciones analíticas reportadas en la literatura especializada parten de un análisis variables físicas, haciendo que el estudio matemático sea difícil para identificar las variables más representativas en la respuesta de la presión de poro. Hacer un modelo adimensional permite formar parámetros adimensionales que involucran combinaciones de las variables físicas logrando en la solución una mejor comprensión fisica de la deformación del suelo afectado por el oleaje.

Oleaje, fondo marino poro-elástico, Análisis paramétrico

Area: Promotion of frontier research and basic science in all fields of knowledge

Citation: Peza-Ortiz, Edebaldo, Arcos-Hernández, Emmanuel, García-Trinidad, Enrique and Torres-Valle, José. [2025]. Parametric analysis of dynamic wave-seabed interaction. Journal Computational Simulation. 9[20] 1-11: e30920111.

Introduction

The phenomenon of wave interaction with the seabed has attracted the attention of maritime and geotechnical engineers in recent years. Understanding the mechanisms and processes of the wave-seabed interaction problem is particularly important for the design of foundations for maritime structures when they are subject to high-energy wave hydrodynamics. Flow conditions around structures not only affect the wave forces acting on them but can also lead to instabilities in the seabed soil generated by water waves, (Christian, Taylor, Yen, & Erali, 1974), (Lundgren, Lindhardt, & Romuld, 1989), (Smith & Gordon, 1983).

In past decades, considerable efforts have been made to study the phenomenon of wave-seabed-structure interaction. The reason for the increased interest in studying this phenomenon is that many coastal structures (such as vertical walls, marinas, oil platform columns, pipelines, breakwaters, among others) have suffered damage due to the seabed response induced by waves and not necessarily due to construction deficiencies.

Fundamentally, foundation failures of maritime structures due to seabed instabilities can be attributed to two mechanisms, which are known as liquefaction and shear failure (Silvester & Hsu, 1989). When waves propagate in the ocean, significant dynamic pressures are generated on the seabed. These pressure fields induce pore pressures and effective stresses. When the pore pressure increases and the vertical effective stresses decrease, a part of the bottom becomes unstable, leading to the generation of the liquefaction phenomenon, in which soil particles become susceptible to being transported by sea currents.

Seabed liquefaction. The seabed is considered a saturated or partially saturated porous medium (containing air bubbles) and can be cohesive or non-cohesive. From a formal perspective, the liquefaction of a non-cohesive soil is the transformation of the soil from a solid state to a liquefied state, as a consequence of the increase in pore pressure and the reduction of effective stresses. When this phenomenon occurs, the soil loses its structural strength, (Groot, Bolton, Foray, Meijers, Palmer, Sandven, Sawicki, & The, 2006), see Figure 1.

Box 1

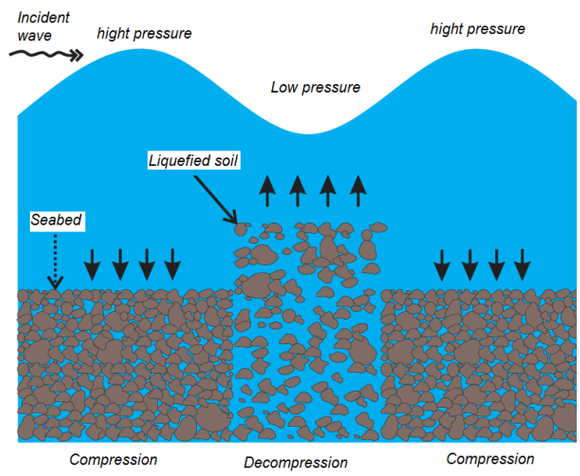

Figure 1
Description of liquefaction
Own source

The main factor causing the liquefaction phenomenon in granular media is due to the excessive increase in pore (P_s) and the reduction of shear stresses (τ) y effective stresses (σ_z'), (Marcuson, 1978). There are two mechanisms causing the accumulation of excessive pore pressure: 1) cyclic loads due to a seismic event and 2) dynamic oscillating loads from waves, (Seed & Rahman, 1978) & (Madsen, 1978).

The study of the liquefaction phenomenon is linked to the understanding of the following phenomena:

1. Soil mechanisms assuming it is dry.
2. The behavior of fully undrained, saturated soil, considering that there is no trapped air.
3. The condition of a partially saturated, undrained soil, taking into account the compressibility of the air-water mixture in the pore; this condition occurs when there are trapped air bubbles.

To determine the liquefaction potential (competition between normal effective stresses and pore pressure), the specialized literature suggests considering the influence of fluid compressibility, the solid material, and the permeability of the porous matrix. The compressibility of the water-air mixture in the pore generates a volume contraction of the mass, which causes a slight increase in pore pressure and, in turn, a slight decrease in effective stress and shear strength.

ISSN: 2523-6865
RENIECYT-SECIHTI: 1702902

Peza-Ortiz, Edebaldo, Arcos-Hernández, Emmanuel, García-Trinidad, Enrique and Torres-Valle, José. [2025]. Parametric analysis of dynamic wave-seabed interaction. Journal Computational Simulation. 9[20] 1-11: e30920111.
https://doi.org/10.35429/JCS.2025.9.20.3.1.11

In the case of soil dilation, the compressibility of the water-air mixture in the pore causes a slight decrease in pore pressure and a slight increase in effective stress and shear strength. The loss of soil load-bearing capacity, due to the type of pressure that occurs, can generate instabilities in the foundations of maritime structures. these can be of two types: by settlement and by settlement and sliding. The orders of magnitude of displacements in real structures are on the order of meters (Groot, Kudella, Meijers, & Oumeraci, 2006).

The pioneering works in the study of the mechanisms that occur in materials subjected to cyclic loads are Biot's poro-elastic theory, (Biot, 1941), and Verruijt's equation, (Verruijt, 1969), these researchers developed three mathematical models which are: 1) Quasi-Static (QS) Model, the fluid-soil mixture in the pore is considered compressible, but the relative accelerations between the fluid and the soil are ignored.

This hypothesis leads to Biot's consolidation equation, in which the inertial terms associated with the mass of the soil and the water of the porous medium are not taken into account. 2) Partially Dynamic Approximation (u-p), the coupled equations of flow and deformation consider the acceleration of the soil mass but not the relative acceleration of the water in the pore (Zienkiewicz, Chang, & Bettes, 1980) and Full Dynamic (FD), in this case, the coupled equations of flow and deformation are formulated in such a way that they involve the relative acceleration of the soil mass and the fluid in the poro-elastic medium.

From a maritime hydraulics perspective, starting in the 1970s, various formulations began to be proposed to characterize the instability of a seabed, (Yamamoto, Sellmeijers, &Hijum, 1978) and (Madsen, 1978) used linear wave theory to study the stability of isotropic, poro-elastic granular soil. Taking into account the obliquity of the incident wave, (Tsai, 1995), proposed an analytical solution to determine the liquefaction potential of a permeable and partially saturated seabed of finite thickness. In the specialized literature, various proposals related to wave-seabed interaction can be found; these studies have treated the phenomenon as a wave train.

As the waves propagate in a shallow flow region, the phenomenon becomes highly non-linear, and the complexity of its study may require computational fluid dynamics and advanced experimental methodologies. (Jeng, Cha, Lin, & Hu, 2001) developed a numerical model to determine the effect of water pressure in the porous medium, considering the wave-seabed-breakwater mechanisms. They demonstrated that the maximum pore pressure occurs around the wave mitigation structures and depends on the wave period, water depth, and the degree of soil saturation.

In turn, (Lee & Lan, 2002) obtained an analytical solution for the propagation of periodic waves over a poro-elastic seabed of infinite depth. Considering long waves of small amplitude, (Lee, Tsai, & Jeng, 2002) determined an analytical solution to describe the seabed response, taking into account seawater seepage through a parametric study (Jeng & Cha, 2003) studied the effect of wave non-linearity and the degree of saturation on the response of the poro-elastic matrix.

Subsequently, (Liu & Jeng, 2007); (Wang, Karim, & Lin, 2007), developed parametric studies to investigate the effects of wave length and period, compressibility of the pore fluid, soil permeability, and stiffness of the deformable granular medium; the results were compared with three different criteria for momentary liquefaction. (Liu & Jeng, 2007), presented an analytical and numerical solution to describe the seepage flow induced by long waves propagating through a permeable and partially saturated seabed.

These researchers concluded that the liquefaction potential is much greater for partially saturated flows. Based on the numerical solution they proposed, they demonstrated that a flow with a higher degree of saturation induces greater wave damping. Subsequently, (Ulker, Rahman, & Jeng, 2009) compared the different poro-elastic formulations and concluded that the (QS) formulation can be used mostly in clay soils and that it does not provide significant results when wave periods are very small. These same authors show that for silty soils (fine sand) with wave periods less than 10s, the (PD) formulation is sufficient, and for sandy soils, the appropriate formulation depends on the seabed permeability and wave period.

ISSN: 2523-6865
RENIECYT-SECIHTI: 1702902

Peza-Ortiz, Edebaldo, Arcos-Hernández, Emmanuel, García-Trinidad, Enrique and Torres-Valle, José. [2025]. Parametric analysis of dynamic wave-seabed interaction. Journal Computational Simulation. 9[20] 1-11: e30920111.
https://doi.org/10.35429/JCS.2025.9.20.3.1.11

When the soil is composed of gravel, the permeability is large, and therefore the (FD) formulation must be used. For their part, Xiao *et al* (2010) determined the liquefaction potential caused by the breaking of solitary waves propagating over a sloping bottom; they concluded that the maximum depth of liquefied sand depends on the wave amplitude and permeability of the saturated soil.

In parallel, (Jeng, Zhou, Luo, Wang, Zhang, & Gao, 2010) studied the seabed response (pore pressure, effective stress, and shear stress) affected by a combined wave-current load. The results show the effect of the sea current velocity on the response of the poro-elastic seabed. Subsequently, (Ye & Jeng, 2011) solved the partially dynamic u-p equations, including the shear stress at the seabed generated by the waves. The numerical results indicate the influence of the shear stress on the dynamic response of the seabed.

Using linear theory (Cha, Zhang, & Blumenstein, 2011) numerically obtained the liquefaction potential in a porous seabed. Other works focus on studying the seabed assuming it is formed by several layers with different physical characteristics. (Zhou, Xu, Wang, & Li, 2011), determined an analytical solution, taking into account a multi-layered poro-elastic soil.

They deduced that the soil characteristics (number of layers, permeability, and shear modulus) and the wave characteristics (water depth and wave steepness) have an influence on the soil response. Through an experimental model, (Sumer, Dixen, & Fredsoe, 2011) demonstrated that the rocks supporting submarine pipelines are stable under the effect of the hydrostatic load of very long waves but can be unstable when exposed to the movement of liquefied soil.

On the other hand, (Wen, Jeng, Wang, & Zhou, 2012) numerically modeled the seabed response, including the non-linear effect of waves and sea current. Their results concluded that the sea current affects the pressure distribution in the poro-elastic soil, and therefore, they suggest taking this effect into account in the study of the liquefaction potential of the seabed.

Based on the VARANS (Volume-Averaged Reynolds-Averaged Navier-Stokes) equations and the u-p approximation, (Zhang, Jeng, Liu, Zhang, & Zhang, 2012) developed a numerical model to study the response of granular soil affected by Bragg reflection, which is generated by a system of several breakwater structures.

Recently, (Zhang, Jeng, Gao, & Zhang, 2013) studied the effect of the non-linearity of waves combined with sea currents on the seabed response and determined that the pore pressure and effective stresses oscillate depending on the velocity and propagation direction of the sea currents. Other works focus their attention on the effect of seepage flow on wave deformation and the response of the porous medium. On the other hand, (Jianhonga, Jeng, Liu, Chan, Wang, & Zhu, 2014) numerically studied the interaction of wave breaking with a composite breakwater and its effect on the seabed. In addition, (Qibo, Hualing, Pandi, Shahoua, Lunlian, Linya, & Yifei, 2020) described an experimental study conducted to investigate how irregular waves affect pore pressures around a monopile on the seabed.

The monopile is a structure used in coastal engineering to support structures such as oil platforms or offshore wind farms. The researchers conducted tests in a wave flume using five different types of irregular waves. They discovered that as the wave height increased, so did the water pressure around the monopile. However, they found that the maximum water pressure inside the seabed decreases as the depth increases.

This suggests that how the water pressure is distributed changes depending on where the monopile is located and how deep it is in the seabed. These findings have important implications for the design of marine structures and coastal engineering. Understanding how irregular waves affect pore pressures can help design more resistant and safer structures, reducing the risks of damage caused by waves and improving the durability of marine facilities.

On the other hand, (Linya, Hualing, Pandi, Jeng, Qibo, Shaohua, Lunliang, & Yifei, 2020) described a detailed analysis of how waves and currents affect pore water pressures around a partially embedded monopile in the seabed.

ISSN: 2523-6865
RENIECYT-SECIHTI: 1702902

Peza-Ortiz, Edebaldo, Arcos-Hernández, Emmanuel, García-Trinidad, Enrique and Torres-Valle, José. [2025]. Parametric analysis of dynamic wave-seabed interaction. Journal Computational Simulation. 9[20] 1-11: e30920111.
https://doi.org/10.35429/JCS.2025.9.20.3.1.11

Unlike previous studies that focused solely on waves, this one examines how the interaction between waves and currents influences the monopile's response. To carry out the study, experiments were conducted in wave flumes to investigate how pore water pressures vary in time and space around the monopile. The results reveal a series of significant findings. For example, when currents are superimposed on waves, it is observed that the wave profile on the side of the monopile fluctuates first, rather than in front, and the shape of the incident wave is smoothed.

In addition, they identified that the amplitudes of the pore water pressures increase and the attenuation of these pressures occurs under the influence of large waves combined with a sea current. Ponce *et al*. (2022) developed research for the implementation of an offshore wind farm off the coast of the department of Colón, Honduras, with the aim of increasing energy generation through renewable sources in the country. Furthermore, Rivas *et al*. (2025) evaluated functional connectivity in different land uses of the Conchal Reserve, part of the Baulas-Conchal Coastal Marine Biological Corridor (CBC-BC).

The theoretical works mentioned above have allowed the scientific community to have a physical understanding of the influence of the various wave parameters on the dynamic response of the soil, which is characterized by pore pressure and soil deformations. In this article, a dimensionless analytical solution is proposed where dimensionless parameters arise that group the competition of the properties of the waves with the seabed. Solving the problems using this methodology will allow for an understanding of the most significant physical variables in the phenomenon of soil instability.

Problem statement

In this work, the incident wave is considered to be a long linear wave of length λ and amplitude A_I. The water waves propagates from left to right over a porous soil of semi-infinite depth. The mean and uniform water depth is h. In the selected Cartesian coordinate system, the positive direction of x-axis is to the right, with the origin at the junction between the porous soil and the impermeable rigid soil.

The z-axis points upward, normal to the soil. In the physical model, the porous medium and the impermeable soil are identified by brown and gray regions, respectively, as shown in Figure 2. It is assumed that the porous soil is a deformable porous medium composed of a three-phase mixture. A solid phase formed by the granular medium, a liquid phase that occupies most of the porous space, and a gaseous phase that sometimes occupies a small portion of the porous space. The granular medium and the pore fluid (including both liquid and gas) can be considered together as a compressible medium.

Box 1

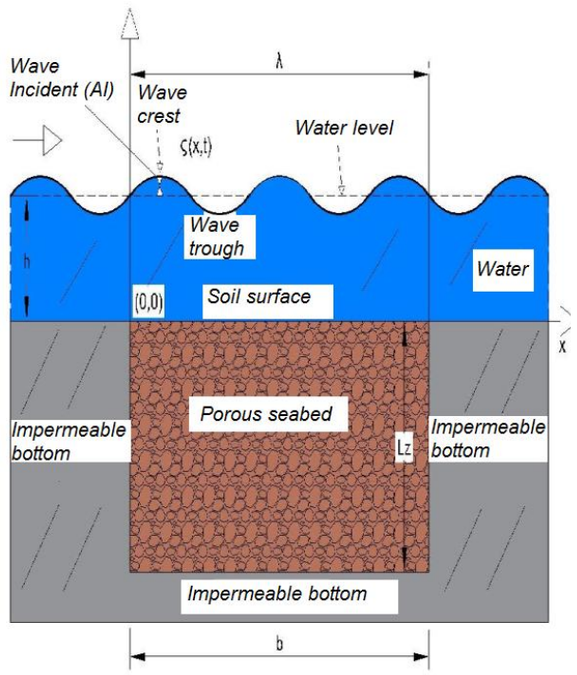

Figure 2
Profile view of the physical model under study
Own source

The physical model is divided into two different regions: 1) Wave field and 2) Poro-elastic medium. It is assumed that the seabed is composed of an assembly of fine, deformable sands, with small permeabilities and assuming that the seabed is impermeable. This condition allows for the decoupled solution of the wave field and the poro-elastic medium, from which the hydrostatic pressure at the bottom at is obtained P_b in $z = 0$

Governing equations in physical variables

The present mathematical model is based on Biot's consolidation theory, following these considerations:

ISSN: 2523-6865
RENIECYT-SECIHTI: 1702902

Peza-Ortiz, Edebaldo, Arcos-Hernández, Emmanuel, García-Trinidad, Enrique and Torres-Valle, José. [2025]. Parametric analysis of dynamic wave-seabed interaction. Journal Computational Simulation. 9[20] 1-11: e30920111.
https://doi.org/10.35429/JCS.2025.9.20.3.1.11

– Isotropic material.
– Linearity in the stress-strain relationship.
– Volumetric deformations are small.
– The water may contain trapped air.
– The water flow through the porous medium obeys Darcy's law.

Taking the above into account, the static equilibrium equations (Biot, 1941) are as follows:

$$G\nabla^2 u_s + \frac{G}{1-2\nu}\frac{\partial \varepsilon_s}{\partial x} = -\frac{\partial p_s}{\partial x} \quad [1]$$

$$G\nabla^2 w_s + \frac{G}{1-2\nu}\frac{\partial \varepsilon_s}{\partial z} = -\frac{\partial p_s}{\partial z} \quad [2]$$

$$k_s\nabla^2 P_s - \gamma_w n\beta\frac{\partial p_s}{\partial t} = \gamma_w\frac{\partial \varepsilon_s}{\partial t}. \quad [3]$$

With their respective boundary conditions: in $z = 0$

$$\sigma_z' = 0, \tau_{xz} = 0, p_s = P_b \quad [4]$$

and at $z = -L_z$

$$u_s, w_s, p_s \to 0. \quad [5]$$

Where G is the shear modulus, ν is the Poisson's ratio, u_s y w_s are soil displacements in the horizontal and vertical directions respectively. ε_s is the volumetric strain, p_s is the pore pressure, γ_w, is the specific weight of water, n is the porosity and β is the compressibility of the seabed. Equations 1-3 are the system of governing equations that will be solved along with their boundary conditions, Equation 4 and Equation 5, in this research.

Governing equations in dimensionless variables

A dimensionless mathematical model is one of the mathematical techniques used for a better appreciation of the physical variables that could be significant in the solution, and it is a contribution of the present work.

Using the characteristic variables identified by (Arcos, Bautista, & Mendez, 2016) Equations 1-3 in dimensionless variables are rewritten as:

$$\beta_0^2\frac{\partial^2 U_s}{\partial \chi^2} + \beta_0\frac{\partial^2 U_s}{\partial Z^2} + \beta_0^2\psi\frac{\partial^2 U_s}{\partial \chi^2} + \frac{\psi}{\Gamma}\frac{\partial^2 W_s}{\partial Z^2} = -\beta_0\frac{\partial P_s}{\partial \chi} \quad [6]$$

$$\beta_0^2\frac{\partial^2 W_s}{\partial \chi^2} + \frac{\partial^2 W_s}{\partial Z^2} + \beta_0^2\Gamma\psi\frac{\partial}{\partial Z}\frac{\partial U_s}{\partial \chi} + \psi\frac{\partial^2 W_s}{\partial Z^2} = -\beta_0\Gamma\frac{\partial P_s}{\partial Z} \quad [7]$$

$$\beta_0\frac{\partial^2 P_s}{\partial \chi^2} + \frac{\partial^2 P_s}{\partial Z^2} - \beta_0\alpha\frac{\partial P_s}{\partial \tau} = \beta_0\Gamma\frac{\partial^2 W_s}{\partial Z^2} = -\beta_0\Gamma\frac{\partial}{\partial \tau}\frac{\partial U_s}{\partial \chi} + \frac{\partial}{\partial \tau}\frac{\partial W_s}{\partial Z}. \quad [8]$$

and the boundary conditions are rewritten as follows, at , in $Z = 0$

$$\sigma_z' = 0, \tau_{xz} = 0, P_s = 1 \quad [9]$$

and at, $Z = -1$

$$U_s, W_s, P_s \to 0 \quad [10]$$

Where the dimensionless parameters are $\beta_0 = \left({}^{L_z}/_{\lambda}\right)^2, \psi = \left({}^{1}/_{1-2\upsilon}\right) \sim O(1), \Gamma = \left({}^{\omega\gamma_w\lambda^2}/_{Gk_s}\right) \gg 1, \alpha = \left({}^{\gamma_w n\beta\omega\lambda^2}/_{k_s}\right) \gg 1.$ Following the orders of magnitude of the dimensionless parameters in Equations 6-8, they reduce to the following terms:

$$\frac{\partial^2 P_s}{\partial Z^2} = -\frac{\partial P_s}{\partial x} \quad [11]$$

$$\frac{\partial^2 W_s}{\partial Z^2} + \beta_0^2\Gamma\psi\frac{\partial}{\partial Z}\frac{\partial U_s}{\partial \chi} + \psi\frac{\partial^2 W_s}{\partial Z^2} = -\beta_0\Gamma\frac{\partial P_s}{\partial Z} \quad [12]$$

$$\frac{\partial^2 P_s}{\partial Z^2} - \beta_0\alpha\frac{\partial P_s}{\partial \tau} = \beta_0^2\Gamma\frac{\partial}{\partial \tau}\frac{\partial U_s}{\partial \chi} + \frac{\partial}{\partial \tau}\frac{\partial W_s}{\partial Z}. \quad [13]$$

The u-p approximation for poro-elastic media can be reduced to a boundary value problem, assuming that the dependent variables have a harmonic oscillation with a frequency equal to that of the wave. Under these conditions, the transient governing equations of the seabed can be formulated as a linear boundary value problem. (Yamamoto, Sellmeijer, & Hijum, 1978). Following Yamamoto's model and combining Equations 11-13 the following relationship is obtained:

$$\frac{d^4\hat{P}_s}{d\bar{Z}^4} + \frac{i\beta_0[\Gamma-\psi\alpha-\alpha]}{[1+\psi]}\frac{d^2\hat{P}_s}{d\bar{Z}^2} - \frac{4i\pi^2\beta_0^2\Gamma}{[1+\psi]}\hat{P}_s = 0 \quad [14]$$

with its respective boundary conditions at: $\bar{Z} = 0$

$$\hat{P}_s = 1, \frac{d\hat{P}_s}{d\bar{Z}} = 0 \quad [15]$$

And at $\bar{Z} = -1$ we have

ISSN: 2523-6865
RENIECYT-SECIHTI: 1702902

Peza-Ortiz, Edebaldo, Arcos-Hernández, Emmanuel, García-Trinidad, Enrique and Torres-Valle, José. [2025]. Parametric analysis of dynamic wave-seabed interaction. Journal Computational Simulation. 9[20] 1-11: e30920111.
https://doi.org/10.35429/JCS.2025.9.20.3.1.11

$$\hat{P}_s = 0, \frac{d\hat{P}_s}{d\bar{Z}} = 0. \quad [16]$$

The derivation of the analytical solution of Equation 14 is based on the exact solution developed by (Polyanin & Zaitsev, 2003), transforming into the following solution of Equation 14 as follows:

$$\hat{P}_s = c_1 e^{(-a)^{1/2}\bar{Z}} + c_2 e^{-(-a)^{1/2}\bar{Z}} + c_3 \cos\left(b^{1/2}\bar{Z}\right) + c_4 \sin\left(b^{1/2}\bar{Z}\right). \quad [17]$$

Where the parameters and are given by the following values:

$$a = \frac{-8\beta_0\pi^2}{(1-\mu)\left(1+\sqrt{1+\frac{16\pi^2\mu}{i\alpha(1-\mu)^2}}\right)} \quad [18]$$

and

$$b = \frac{i\beta_0\alpha(1-\mu)\left(1+\sqrt{1+\frac{16\pi^2\mu}{i\alpha(1-\mu)^2}}\right)}{2\mu} \quad [19]$$

where

$$\mu = nG\beta\left(1+\frac{1}{1-2v}\right). \quad [20]$$

Using the boundary conditions from Equation 15 and Equation 16 the integration constants c_1, c_2, c_3, c_4 of term 17 are determined which in matrix form is expressed as:

$$\begin{bmatrix} 1 & 1 & 1 & 0 \\ ia^{\frac{1}{2}} & -ia^{\frac{1}{2}} & 0 & b^{\frac{1}{2}} \\ e^{-ia^{\frac{1}{2}}} & e^{ia^{\frac{1}{2}}} & \cos\left(-b^{\frac{1}{2}}\right) & \sin\left(-b^{\frac{1}{2}}\right) \\ ia^{\frac{1}{2}}e^{-ia^{\frac{1}{2}}} & ia^{\frac{1}{2}}e^{ia^{\frac{1}{2}}} & -b^{\frac{1}{2}}\sin\left(-b^{\frac{1}{2}}\right) & b^{\frac{1}{2}}\cos\left(-b^{\frac{1}{2}}\right) \end{bmatrix} \begin{bmatrix} c_1 \\ c_2 \\ c_3 \\ c_4 \end{bmatrix} = \begin{bmatrix} 1 \\ 0 \\ 0 \\ 0 \end{bmatrix}. \quad [21]$$

Next, the analysis of the results of the most representative parameters in the response of the seabed pore pressure is presented.

Results analysis

Figure 3 shows the comparison of the analytical solution in its dimensionless form (Yamamoto, Sellmeijer, & Hijum, 1978) which corresponds to Equation 22, and the present solution, Equation 17

$$P_s = \frac{\rho g h}{(\gamma_s - \gamma_w)L} e^{\left(\frac{-2\pi L}{\lambda}\right)Z}. \quad [22]$$

Box 2

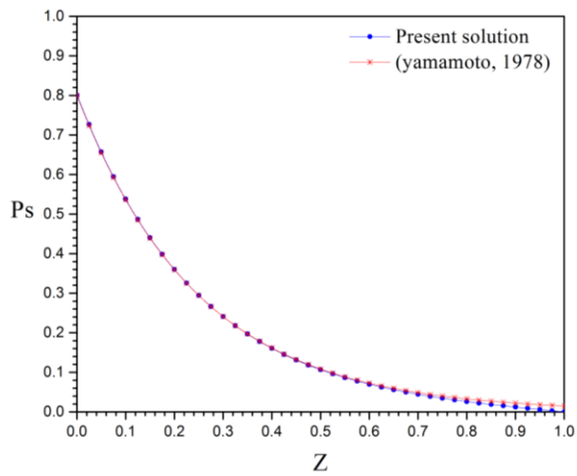

Figure 3

Comparison of the present solution with Yamamoto (1978)

Own source

Usando los valores físicos registrados en la Tabla 1, en ambas soluciones se observa que tienen muy buena aproximación, lo que significa que el modelo matemático está validado.

Box 3

Table 1

Physical values of the waves and the seabed

Water waves	
Water depth	h=0.8m
Wavelength	$\lambda = 1.57$m
Specific weight water	$\gamma_w = 9810 N/m^3$
Seabed	
Gravitational constant	$g = 9.81 m/s^2$
Specific weight of soil	$\gamma_s = 25996.5\ N/m^3$
Liquefaction Depth	$L_z = 1\ m$

Own source

The same figure shows the propagation of the pore pressure along the seabed, with its maximum value occurring at the wave-seabed interface where $Z = 0$, As the soil thickness increases, the pore pressure decreases as $Z \to 1$.

One of the main contributions of this research was to solve the mathematical model in dimensionless form to identify the dominant parameters in the pore pressure distribution. To carry out the analysis, real physical values for the waves and seabed were taken into account as shown in Table 2.

ISSN: 2523-6865
RENIECYT-SECIHTI: 1702902

Peza-Ortiz, Edebaldo, Arcos-Hernández, Emmanuel, García-Trinidad, Enrique and Torres-Valle, José. [2025]. Parametric analysis of dynamic wave-seabed interaction. Journal Computational Simulation. 9[20] 1-11: e30920111.
https://doi.org/10.35429/JCS.2025.9.20.3.1.11

Box 4

Table 2

Physical values of the waves and the seabed for the results analysis

Water waves	
Water depth	h=40 m
Wavelength	$\lambda = 100$ m
Wave period	$T = 5\ s$
Seabed	
Poisson's ratio	$\upsilon = 0.35$
Posity	$n = 0.3$
Degree of saturation	$S_r = 1$
Shear modulus	$G = 19999999\ Pa$
Specific weight of soil	$\gamma_s = 25996.5\ N/m^3$
Specific weight of water	$\gamma_w = 9810 N/m^3$
Darcy's permeability	$k_s = 0.0001\ m/s^2$
Bulk modulus of water	$K_f = 1900000000 Pa$
Liquefaction depth	$L_z = 30\ m$

Own source

Figure 4 shows the effect of the water depth of the ocean h on the pore pressure $\hat{P}_s$ along the bottom of the porous medium $\bar{Z}$.

Box 5

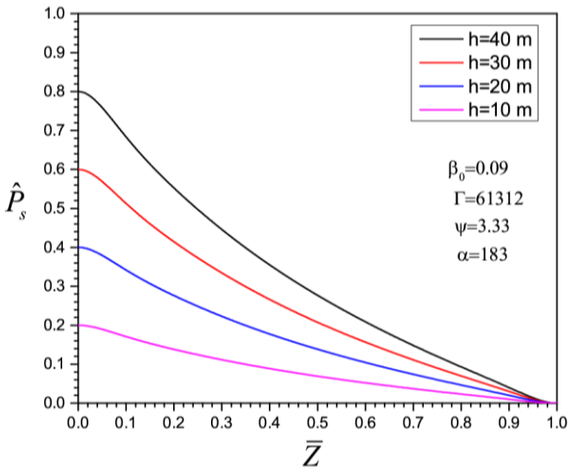

Figure 4

Pore pressure distribution for different sea water depths

Own Source

The same figure shows that as the water depth increases, the pore pressure also, for a depth $h = 40\ m$ there is a dimensionless pore pressure value of $\hat{P}_s = 0.8$ and for values of $h = 10\ m$ there is a pore pressure of $\hat{P}_s = 0.2$ both at $\bar{Z} = 0$.

Box 6

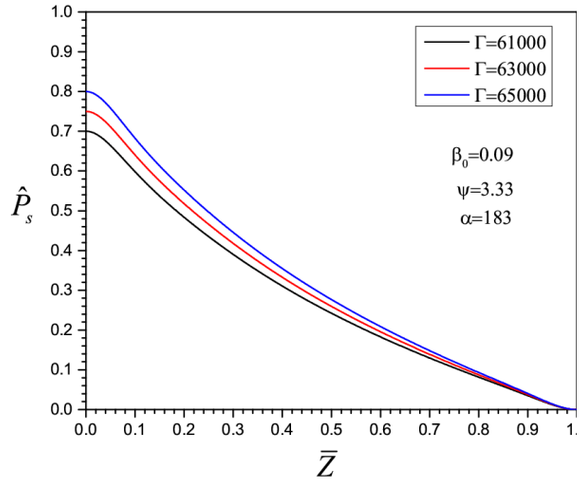

Figure 5

Pore pressure distribution for different values of the parameter Γ.

Own Source

On the other hand, Figure 5 shows the effect of the parameter $\Gamma = \omega\gamma_w\lambda^2/Gk_s$ on the behavior of the pore pressure $\hat{P}_s$. The results show that for increasing values of the parameter Γ, the pore pressure increases, This is because the permeability of the pore k_s is very small and there is a greater concentration of pressure or the wave is more frequent where the value of ω increases or the wavelength λ increases. Another possible cause is that the granular material over which the wave propagates has a decreasing shear strength, which is the case for loose sands.

Conclusions

In this work, an analytical solution of the dimensionless mathematical model (Equations 1-5) was determined to find the pore pressure along the seabed. The results indicate that the behavior of the pore pressure $\hat{P}_s$ is a function of the dimensionless parameters that group the properties of the waves and the seabed. Based on the analytical result obtained, it was identified that the propagation of pore pressure is strongly affected by the following properties:

For increasing wavelengths λ which is the case for long waves, the energy contained in the waves is greater than for short waves.

When the permeability k_s is small, there is a greater accumulation of energy in the pore pressure.

ISSN: 2523-6865
RENIECYT-SECIHTI: 1702902

Peza-Ortiz, Edebaldo, Arcos-Hernández, Emmanuel, García-Trinidad, Enrique and Torres-Valle, José. [2025]. Parametric analysis of dynamic wave-seabed interaction. Journal Computational Simulation. 9[20] 1-11: e30920111.
https://doi.org/10.35429/JCS.2025.9.20.3.1.11

For the case of an increasing fgrequency ω , it means that the wave train is more repetitive, causing greater fatigue on the seabed. Loose sands are more vulnerable to soil liquefaction due to the lower cohesion force between particles, which causes the shear strength to decrease.

The physical understanding of wave-seabed interaction is important to achieve safe foundations for ocean structures built on the seabed.

Conflict of interest

The authors declare no interest conflict. They have no known competing financial interests or personal relationships that could have appeared to influence the article reported in this article.

Acknowledgments

This work has been made possible thanks to the valuable support of the Secretariat of Science, Humanities, Technology, and Innovation (SECIHTI). We deeply appreciate their support, which demonstrates their commitment to promoting science and innovation.

Author contribution

Peza-Ortiz, Edebaldo. PhD: Contributed to the project idea, research method

Arcos-Hernández, Emmanuel. PhD: Contributed to the project idea, research method and technique.

Garcia-Trinidad, Enrique. PhD: Contributed to the project idea, research method

Torres-Valle, Jose. PhD: Contributed to the project idea, research method

References

Basics

Arcos, E., Bautista, E., & Mendez, F. (2016). Scaling Analysis for the Liquefaction Phenomena Induced by Water Waves. OMAE2016-54535, V007T06A034; 8 pages.

Biot, M. A. (1941). General theory of three-dimensional consolidation. Journal Applied. Physics, 12(155), 155-164.

Cha, D., Zhang, H., & Blumenstein, M. (2011). Prediction of maximum wave-induced liquefaction in porous seabed using multi-artificial neural network model. Ocean Engineering, 38(7), 878-887.

Christian, J. T., Taylor, P. K., Yen, J. K. C., & Erali, D. R. (1974). Large diameter underwater pipeline for nuclear power plant designed against soil liquefaction. Proceeding of Offshore Technology Conference, 597-606.

Groot, M. B., Bolton, M. D., Foray, P., Meijers, P., Palmer, A. C., Sandven, R., Sawicki, A., & The, T. C. (2006). Physics of liquefaction phenomena around marine structures. Journal of Waterway, Port, Coastal and Ocean Engineering, 132(4), 227-243.

Groot, M. B., Kudella, M., Meijers, P., & Oumeraci, H. (2006). Liquefaction phenomena underneath marine gravity structures subjected to wave loads. Journal of Waterway, Port, Coastal and Ocean Engineering, 132(4), 325-335.

Jeng, D. S., Cha, D. H., Lin, Y. S., & P. S. Hu, P. S. (2001). Wave-induced pore pressure around a composite breakwater. Ocean Engineering, 28(10),1413-1435.

Supports

Jeng, D. S., & Cha, D. H. (2003). Effects of dynamic soil behavior and wave nonlinearity on the wave-induced pore pressure and effective stresses in porous seabed. Ocean Engineering, 30(16), 2064-2089.

Jeng, D. S., Zhou, X. L., Luo, X. D., Wang, J. H., Zhang, Z., & Gao, F. P. (2010). Response of porous seabed to dynamic loadings. Geothecnical Engineering, 41(4), 205-214.

Jianhonga, Y., Jeng, D. S., Liu, P. L. F., Chan, A. H. C., Wang, R., & Zhu, C. (2014). Breaking wave-induced response of composite breakwater and liquefaction in seabed foundation. Coastal Engineering, 85, 72-86.

Lee, J. F., & Lan, Y. J. (2002). On waves propagation over poro-elastic seabed. Ocean Engineering, 29(8), 931-946.

ISSN: 2523-6865
RENIECYT-SECIHTI: 1702902

Peza-Ortiz, Edebaldo, Arcos-Hernández, Emmanuel, García-Trinidad, Enrique and Torres-Valle, José. [2025]. Parametric analysis of dynamic wave-seabed interaction. Journal Computational Simulation. 9[20] 1-11: e30920111.
https://doi.org/10.35429/JCS.2025.9.20.3.1.11

Lee, T. C., Tsai, C. P., & Jeng, D. S. (2002). Ocean waves propagating over a porous seabed of finite thickness. Ocean Engineering, 29(12), 1577-1601.

Liu, H., & Jeng, D. S. (2007). A semi-analytical for random wave-induced soil reponse and seabed liquefaction in marine sediments. J. Ocean Engineering, 34(8), 1211-1224.

Liu, P. L. F., Park, Y. S., & Lara, J. L. (2007). Long-wave-induced flows in an unsaturated permeable seabed. Journal of Fluid Mechanics, 586, 323-345.

Lundgren, H., Lindhardt, J. H. C., & Romold, C. J. (1989). Stability of breakwaters on porous foundation. Proceeding of 12th International Conference on Soil Mechanics and Foundation Engineering, 451-454.

Linya, C., Hualing, Z., Pandi, W., Jeng, D. S., Qibo, Z., Shaohua, W., Lunliang, D., & Yifei, L. (2020). Physical modeling of combined waves and current propagating around a partially embedded monopile in a porous seabed. Ocean Engineering, 205, 1-20.

Madsen, O. S. (1978). Wave-induced pore pressures and effective stress in a porous bed. Géotechnique. 28(4), 377-393.

Marcuson, W. F. (1978). Definition of terms related to liquefaction. Journal of the Geotechnical Engineering Division, 104(9), 1197-1200.

Polyanin, A. D., & Zaitzev, V. F. (2003). Handbook of exact solutions for ordinary differential equations. Chapman and Hall/CRC.

Ponce, R. R., Osorio, M. E., & Cruz. A. E. (2022). Análisis para la implementación de un parque eólico marino en la costa norte de Honduras. Facultad de Ingeniería Electrónica, Tesis.

Qibo, Z., Hualing, Z., Pandi, W., Shaohua, W., Lunliang, D., Linya, C., & Yifei. (2020). Experimental study on irregular wave-induced pore-water pressures in a porous seabed around a mono-pile. Applied Ocean Research, 95, 1-14.

Rivas, A. M., Montoya, C. S., Rodriguez, B. H., & Badilla, B. G. (2025). Conectividad funcional en la reserva conchal como parte del corredor biológico costero marino baulas-conchal costa rica. Revista Forestal Mesoamerica Kurú, 22.

Seed, H. B., & Rahman, M. S. (1978). Wave-induced pore pressure in relation to ocean floor stability of cohesionless soils. Marine Geotechnology, 3(2), 123-150.

Silvester, R., & Hsu, J. R. C. (1989). Sines revisited. Journal of Waterway, Port, Coastal, and Ocean Engineering, 115(3), 327-344.

Smith, A. W., & Gordon, A. D. (1983). Large breakwater toe failures. Journal of Waterway, Port, Coastal, and Ocean Engineering, 109(2), 253-255.

Sumer, B. M., Dixen, F. H., & Fredsoe, J. (2011). Stability of submerged rock berms exposed to motion of liquefied soil in waves. Ocean Engineering, 38(7), 849-859.

Tsai, C. P. (1995). Wave-induced liquefaction potential in a porous seabed in front of a breakwater. Ocean Engineering, 22(1), 1-18.

Differences

Ulker, M. B. C., Rahman, M. S., & Jeng, D. S. (2009). Wave-induced response of seabed: Various formulations and their applicability. Applied Ocean Research, 31(1), 12-24.

Verruijt, A. (1969). Elastic storage of aquifers. In flow through porous media. Academic Press.

Wang, J. G., Karim, M. R., & Lin, P. Z. (2007). Analysis of seabed instability using element free Galerkin method. Ocean Eng, 34(2), 247-260.

Wen, F., Jeng, D. S., Wang, J. H., & Zhou, X. L. (2012). Numerical modeling of response of a saturated porous seabed around an offshore pipeline considering non-linear wave and current interaction. Applied Ocean Research, 35, 25-37.

Xiao, H., Young, Y. L., & Prévost, J. H. (2010). Parametric study of breaking solitary wave induced liquefaction of coastal sandy slopes. Ocean Engineering, 37(17), 1546-1553.

ISSN: 2523-6865
RENIECYT-SECIHTI: 1702902

Peza-Ortiz, Edebaldo, Arcos-Hernández, Emmanuel, García-Trinidad, Enrique and Torres-Valle, José. [2025]. Parametric analysis of dynamic wave-seabed interaction. Journal Computational Simulation. 9[20] 1-11: e30920111.
https://doi.org/10.35429/JCS.2025.9.20.3.1.11

Yamamoto, T. H. L., Sellmeijer., & Hijum, E. V. (1978). On the response of a poro-elastic bed to water waves. Journal of Fluid Mechanics, 87, 193-206.

Ye, J., & Jeng, D. S. (2011). Effects of bottom shear stresses on the wave induced dynamic response in a porous seabed shear model. Acta Mechanica Sinica, 27(6), 898-910.

Zhang, J. S., Jeng, D. S., Liu, P. L. F., Zhang, C., & Zhang, Y. (2012). Response a porous seabed to water waves over permeable submerged breakwaters with Bragg reflection. Ocean Engineering, 43, 1-12.

Zhang, Y., Jeng, D. S., Gao, F. P., & Zhang, J. S. (2013). An analytical solution for response of a porous seabed to combined wave and current loading. Ocean Engineering, 57, 240-247.

Zienkiewicz, O. C., Chang, C. T., & Bettess, P. (1980). Drained, undrained, consolidating and dynamic behavior assumptions in soil. Géotechnique, 30(4), 385-395.

Zhou, X. L., Xu, B., Wang, J. H., & Li, Y. (2011). An analytical solution for wave-induced seabed response in a multi-layered poro-elastic seabed. Ocean Engineering, 38(1), 119-129.

ISSN: 2523-6865
RENIECYT-SECIHTI: 1702902

Peza-Ortiz, Edebaldo, Arcos-Hernández, Emmanuel, García-Trinidad, Enrique and Torres-Valle, José. [2025]. Parametric analysis of dynamic wave-seabed interaction. Journal Computational Simulation. 9[20] 1-11: e30920111.
https://doi.org/10.35429/JCS.2025.9.20.3.1.11

Journal Computational Simulation 9[20]1-10: e40920110
Article

Nodal analysis of transtibial prostheses using the finite element method with Matlab

Análisis nodal de prótesis transtibial por el Método de Elementos Finitos mediante el uso de Matlab

Cortez-Solis, Reynaldo*[a], Fuentes-Castañeda, Pilar[b], Betanzos-Castillo, Francisco[c], Jaramillo-Rodriguez, Eduardo[d]

[a] Tecnológico Nacional de México – TES Valle de Bravo • KUD-2900-2024 • 0000-0001-7519-1815 • 1113392
[b] Tecnológico Nacional de México – TES Valle de Bravo • KUD-2889-2024 • 0000-0001-6567-9614 • 428699
[c] Tecnológico Nacional de México – TES Valle de Bravo • AIE-1532-2022 • 0000-0002-7245-703X • 206209
[d] Tecnológico Nacional de México – TES Valle de Bravo • OIU-7288-2025 • 0009-0002-6448-7383 • 2139852

SECIHTI classification:

Area: Engineering.
Field: Engineering.
Discipline: Mechanical Engineering
Subdiscipline: Mechanical design

https://doi.org/10.35429/JCS.2025.9.20.4.1.10
Article History:
Received: June 30, 2025
Accepted: December 15, 2025

* ✉ [reynaldo.cs@vbravo.tecnm.mx]

Abstract

CAE analysis involves different solutions and methods for all 2D and 3D CAD models. Different methods are used to perform this type of analysis. One of the main methods used in this project was finite element analysis using software. The main focus was to analyze the meshing of a socket for a transtibial prosthesis, verifying the connection and discretization of the mesh throughout the model. We began with 3D modeling in Solidworks mechanical design software and mesh analysis in Matlab computational numerical analysis software. Different configurations and parameters were evaluated to discretize and verify the convergence of the mesh throughout the three-dimensional or wireframe model of the part.

Nodal analysis of transtibial prostheses using the finite element method with Matlab

Objetives	Methodology	Contribution
-3D modeling. -Mesh generation in Solidworks software. -Mesh generation in Matlab computational numerical software. -Nodal analysis.	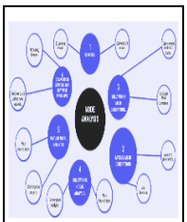	Mesh analysis and discretization using the finite element method with software, verifying convergence between nodal joints.

Mesh, nodal analysis, and 3D modeling

Resumen

El análisis CAE implica diferentes soluciones y métodos para todos los modelos CAD en 2D y 3D. Se utilizan diferentes métodos para realizar este tipo de análisis. Uno de los principales métodos utilizados en este proyecto fue el análisis de elementos finitos mediante software. El objetivo principal era analizar el mallado de un encaje para una prótesis transtibial, verificando la conexión y la discretización de la malla en todo el modelo. Se comenzó con el modelado 3D en el software de diseño mecánico Solidworks y el análisis de mallas en el software de análisis numérico computacional Matlab. Se evaluaron diferentes configuraciones y parámetros para discretizar y verificar la convergencia de la malla en todo el modelo tridimensional o de alambre de la pieza.

Análisis nodal de prótesis transtibial por el Método de Elementos Finitos mediante el uso de Matlab

Objetivos	Metodología	Contribución
-Modelado 3D. -Mallado en Software Solidworks. -Mallado en Software numérico computacional Matlab. -Análisis Nodal		Análisis de malla y discretización de esta por el método de elementos finitos mediante software, verificar convergencia entre la unión nodal.

Malla, análisis nodal y Modelado 3D

Area: Promotion of frontier research and basic science in all fields of knowledge

Citation: Cortez-Solis, Reynaldo, Fuentes-Castañeda, Pilar, Betanzos-Castillo, Francisco, Jaramillo-Rodriguez, Eduardo. [2025]. Nodal analysis of transtibial prostheses using the finite element method with Matlab. Journal Computational Simulation. 9[20] 1-10: e40920110.

Introduction

Structural analysis of mechanical components is fundamental in engineering design and validation, where obtaining accurate results based on load behavior is critical to ensuring safety, functionality, and durability. Traditional analytical methods are insufficient for complex geometries or boundary and contour conditions. In addition to this, the Finite Element Method (FEM) has been chosen as the predominant numerical technique for these purposes. This type of FEM method focuses on the discretization of the continuous domain of a part into a mesh of simpler subdomains (finite elements), interconnected at discrete points known as nodes. It is in this context that nodal analysis emerges as the fundamental stage, since the overall behavior of the structure is determined from the calculation of the displacements, stresses, and deformations at each of these nodes.

Mesh generation and analysis are therefore fundamental elements that directly define the accuracy and efficiency of the simulation. For all these analyses, there is powerful software available for finite element analysis (CAE). Therefore, for this article, numerical algorithms were implemented in environments such as MATLAB, as it offers flexibility and depth of understanding compared to other software. MATLAB, as computational domain software with all its specialized toolboxes and its capacity for intensive matrix handling, is ideal for developing and validating nodal analysis methodologies, allowing control over each phase of the process: from mesh generation and the application of boundary conditions to the assembly of the global stiffness matrix and the resolution of the system of equations.

Likewise, a methodology is presented for the nodal analysis of mechanical part meshing using MATLAB computational software and 3D modeling in Solidworks CAD software, comparing the meshes in both software programs and thus verifying the discretization and nodal union in each socket element. The main objective is to develop an analysis that allows the systematic evaluation of the influence of meshing parameters (such as element type, density, and regularity) on the results of the nodal analysis.

It also aims to highlight MATLAB's ability to perform sensitivity analysis and mesh optimization, key aspects for reducing discretization error without incurring prohibitive computational costs.

Antecedentes

In 3D modeling, according to (Bermejo, 2020), all the elements that make up a 3D scene are formed by polygons. These polygons have to be processed by the hardware in order to be displayed as we want them to be. The greater the number of polygons, the higher the resolution and the greater the calculation process. This can cause slowdowns in the display of views and even program crashes. In rendering, it is more of the same, including the textures and lighting created in the scene.

The analysis of mechanical parts using computer control software and the transfer of CAD models in SolidWorks in the CAE (Computer-Aided Engineering) section allow us to identify the development that technology has undergone. Therefore, a CAD model is taken as a reference in order to create an STL file. These three-dimensional files are first designed by a geometric modeler, which follows a construction algorithm to create a representation of simple boundaries that cover the surface of the solid using triangles. This triangle mesh is stored in an STL format, which is used to define the actual geometry of the solid with a wide variety of industrial applications, as well as rapid prototyping and manufacturing. (Gutiérrez Madrigal, 2018).

Finite element analysis (FEA), also known as the finite element method, is a numerical technique for solving field problems described by a set of partial differential equations. The finite element method is commonly used in many engineering disciplines, such as machine design, acoustics, electromagnetism, soil mechanics, fluid dynamics, among others. In mechanical engineering, FEA is widely used for structural, vibration, and thermal problems. However, it is not the only tool available for numerical analysis. Other numerical methods used in engineering include: the finite difference method, the limit state method, and the finite volume method.

ISSN: 2523-6865
RENIECYT-SECIHTI: 1702902

Cortez-Solis, Reynaldo, Fuentes-Castañeda, Pilar, Betanzos-Castillo, Francisco, Jaramillo-Rodriguez, Eduardo. [2025]. Nodal analysis of transtibial prostheses using the finite element method with Matlab. Journal Computational Simulation. 9[20] 1-10: e40920110.
https://doi.org/10.35429/JCS.2025.9.20.4.1.10

Nevertheless, due to its versatility and high numerical efficiency, FEA has come to dominate the market for engineering analysis software, while other methods have been relegated to niche applications. (González Woge, 2020).

Finite element (FE) methods are widely used in biomechanics and bioengineering due to their ability to simulate and analyze the behavior of complex systems under various loading conditions. In the context of biomechanics, FE analysis can provide valuable information about the distribution of stresses and strains within biological structures such as bones, muscles, ligaments, and tendons.

Numerous studies have been conducted in this field. The first model was presented by Zhang, who investigated the effect of friction and slippage at the interface between the stump and the socket. They found that the friction factor has a significant impact on pressures, shear loads, slippage, and bone movement. Jia investigated how inertial loading affected shear stress and interface pressure. L. Zhang used contact analysis to simulate friction conditions between the skin and the socket. Meng used finite element models to examine stress in the stump of transfemoral amputees with compression/release stabilised sockets (CRS). Sofia C. performed a finite element analysis (FEA) to estimate the interaction between the stump and the socket during the gait cycle of fourteen transfemoral amputees. (Messaad, 2025).

Mesh Generation

There are two distinct ways of working with three-dimensional objects in a CAD system: through solid modeling or surface modeling. In the first case, you work with a library of simple solids (sphere, cone, box, cylinder, etc.) and can perform all kinds of Boolean operations with them. Although the vast majority of mechanical components can be constructed in this way, there are cases where this methodology cannot be applied (aerodynamic vehicles, for example). The main advantages of this method are the simplicity with which the geometry is defined and the ease of automating the interface with the mesh generation system.

On the other hand, surface modeling allows for complete generality in the geometry to be constructed, but requires a precise description of each piece (patch) of the surface, which in many cases can be difficult to achieve. On the other hand, surface modeling allows for complete generality in the geometry to be constructed, but requires a precise description of each piece (patch) of the surface, which in many cases can be very cumbersome. (Vénere, 1996).

Methodology

The following shows the development and application of the methodology of this project as a starting point for this research. It should be noted that there is various literature on the web that discusses the generation of meshes and analysis of mechanical parts in SolidWorks and MATLAB, However, in this project presentation, nodal analysis was performed in both software programs, verifying the connection and polygonal behavior of the mesh, since each part of the discretization is essential for observing the structure of the transtibial prosthesis. Previously, CAE analysis of the same prosthesis was performed with two CAD design and modeling software programs. The main point is to verify the convergence of the nodes by transferring a 3D digital model and generating a code that allows the wireframe or mesh model of the prosthesis to be developed. A diagram showing the steps to follow for nodal analysis and obtaining results is shown.

Box 1

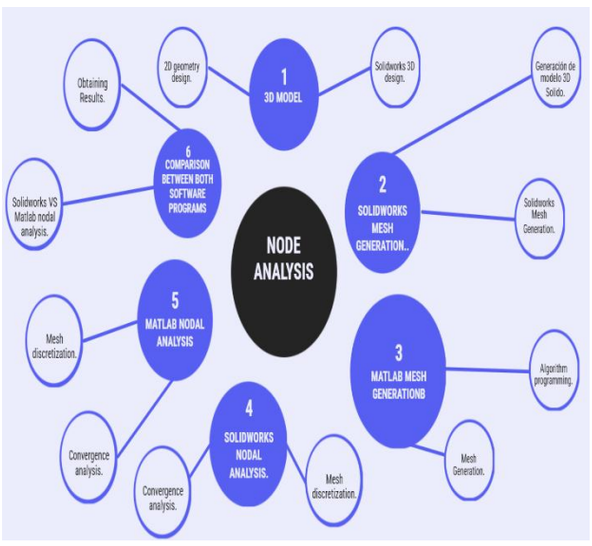

Figure 1
Stages of development and nodal analysis
Source: Own Elaboration

ISSN: 2523-6865
RENIECYT-SECIHTI: 1702902

Cortez-Solis, Reynaldo, Fuentes-Castañeda, Pilar, Betanzos-Castillo, Francisco, Jaramillo-Rodriguez, Eduardo. [2025]. Nodal analysis of transtibial prostheses using the finite element method with Matlab. Journal Computational Simulation. 9[20] 1-10: e40920110.
https://doi.org/10.35429/JCS.2025.9.20.4.1.10

1. 2D design and 3D modeling in software:

At this stage of the design process, a two-dimensional or three-dimensional digital model is used as a reference, depending on the case. This model must contain structured geometry so that it can be analyzed in CAD design software. Once the geometry or 2D model is available, this phase also focuses on the design of the model in two dimensions (2D) or three dimensions (3D) and its subsequent preparation for the generation of a file in STL (Standard Tessellation Language or Stereolithography) format, which is the universal standard for the interpretation of geometries by meshing and analysis software.

2. Solidworks Mesh Generation:

Once the discrete representation of the geometry in STL format has been obtained, the next critical step in the analysis is the generation of the finite element mesh. This step consists of discretizing the 2D and 3D geometric domain into a set of simpler and more regular subdomains called interconnected elements at discrete points or nodes. For this study, a fine mesh has been generated, characterized by a high density of elements, with the main objective of minimizing discretization error and capturing stress and strain gradients more accurately, especially in areas of stress concentration.

3. Matlab Mesh Generation:

Once the STL file has been generated, it is imported into the MATLAB environment for processing, as MATLAB has specific functions (such as stlread or importGeometry from the PDE Toolbox) for reading these files and storing the information on vertices and triangular faces in matrix arrays. This numerical representation of the geometry, typically using two matrices: Vertices (Nx3) and Faces (Mx3), is the basis on which the nodal analysis and finite element mesh generation algorithms will be implemented in the subsequent stages of this research.

It should be noted that the transition from an initial mesh to a fine mesh is controlled by defining specific refinement criteria. These criteria, implemented through functions and parameters in MATLAB, include:

Maximum Element Size (Hmax): Global parameter that defines the largest edge length allowed for any element in the mesh. For a fine mesh, this value is set significantly lower than for a coarse mesh.

Minimum Element Size (Hmin): Limits excessive refinement in regions where it is not necessary, controlling computational cost.

Geometry Gradient Refinement: The algorithm can automatically refine regions with high curvature (defined in the original STL) to better approximate the geometry.

Local Refinement Using Density Functions: Functions can be defined that specify a desired element size at specific spatial coordinates, allowing greater control to refine areas of particular interest, such as holes, corners, or areas where loads are applied.

4. Solidworks nodal analysis:

In order to validate the methodology implemented in MATLAB and the accuracy of the results obtained from the nodal analysis of the generated fine mesh, a comparative analysis was carried out using the SolidWorks Simulation module. This Finite Element Analysis (FEA) application software demonstrates the verification process as a fundamental part of ensuring the reliability of the code implemented in MATLAB and enabling a comparison of mesh generation to be made, taking as a reference: an identical and perfectly defined geometric representation, material properties (isotropic elastic linear model), including the Modulus of Elasticity (Young's Modulus), Poisson's ratio, and density. Identical constraints were also applied as boundary conditions (fixations, supports, inputs, outputs, forces) in the same geometric locations. All these configurations were designed to generate a finite element mesh of the same type as MATLAB, i.e., with a global element size comparable to that of the fine mesh used for the MATLAB analysis.

5. Matlab Nodal Analysis:

The implementation of nodal analysis in MATLAB was carried out explicitly considering the critical influence of discretization, complemented by a mesh convergence study to ensure the robustness and accuracy of the results.

ISSN: 2523-6865
RENIECYT-SECIHTI: 1702902

Cortez-Solis, Reynaldo, Fuentes-Castañeda, Pilar, Betanzos-Castillo, Francisco, Jaramillo-Rodriguez, Eduardo. [2025]. Nodal analysis of transtibial prostheses using the finite element method with Matlab. Journal Computational Simulation. 9[20] 1-10: e40920110.
https://doi.org/10.35429/JCS.2025.9.20.4.1.10

This systematic approach allowed us to determine an optimal mesh density that balances numerical accuracy with computational efficiency.

For the section on mesh convergence analysis, reference was made to to (Autodesk, 2023) states that this is an essential methodology for quantifying the influence of discretization and establishing objective criteria for selecting a sufficiently fine mesh. In this study, a Key Interest Variable was selected, such as maximum displacement in a critical direction or maximum von Mises stress.

6. Comparison between both software programs:

In this section, the main objective is to conduct a comprehensive comparison between the MATLAB and SolidWorks Simulation platforms, evaluating their distinctive features in the context of nodal analysis of mechanical parts. This comparison focuses not only on numerical accuracy, but also on operational aspects, control, flexibility, and applicability, which are crucial for selecting the appropriate tool depending on the application and method used.

Mathematical Modeling FEM

In order to perform the finite element analysis, different systems of linear equations were used as a reference, as well as differential equations that allowed the convergence of each of the nodes and the geometries of each 2D polygon to be visualized.

On the other hand, mesh discretization equations were used, as well as the dominant stiffness matrix and the application of boundary conditions.

Nodal matrix

Node Matrix (p or Nodes): A matrix of size n×dn×d, where nn is the total number of nodes and dd is the dimensionality (2 or 3). Each row contains the coordinates (x,y)(x,y) or (x,y,z)(x,y,z) of a node.

$$p=\begin{bmatrix} x1 & y1 & z1 \\ x2 & y2 & z2 \\ \vdots & \vdots & \vdots \\ \vdots & \vdots & \vdots \\ xn & yn & zn \end{bmatrix} \quad [1]$$

Node connectivity matrix.

$$t=\begin{bmatrix} x1,1 & y1,2 & z1,3 \\ x2,1 & y2,2 & z2,3 \\ \vdots & \vdots & \vdots \\ \vdots & \vdots & \vdots \\ xm,1 & ym,2 & zm,3 \end{bmatrix} \quad [2]$$

Where: an $m \times k$ matrix, where m is the number of elements and k is the number of nodes per element. Each row contains the indices of the nodes that make up the element.

Next, the Global Stiffness Matrix (K) assembly is analyzed for each element, and its elemental stiffness matrix [k]e is calculated based on the material properties and element geometry. These elemental matrices are then assembled into the global stiffness matrix K using a direct summation process based on nodal connectivity.

The following steps are also carried out:

Application of Boundary Conditions: The rows and columns of K corresponding to the restricted degrees of freedom (known displacements) are modified, imposing Dirichlet conditions.

– Assembly of the Nodal Force Vector (f): The applied loads are distributed to the corresponding nodes, forming the global force vector f.

– Solution of the System of Equations: The linear system of equations is solved to obtain the vector of unknown nodal displacements (U).

Where: stresses and strains in a structural element can be calculated using the following equation:

$$(K)\{U\} = \{F\} \quad [3]$$

Likewise, all of the analysis performed is based on the theory of the Finite Element Method (FEM) for linear elasticity. The mathematical fundamentals that govern the mechanical behavior of solids and their numerical discretization are also addressed.

The starting point is the theory of isotropic linear elasticity. For a continuous domain Ω, the boundary value problem is defined by [1, 2]:

ISSN: 2523-6865
RENIECYT-SECIHTI: 1702902

Cortez-Solis, Reynaldo, Fuentes-Castañeda, Pilar, Betanzos-Castillo, Francisco, Jaramillo-Rodriguez, Eduardo. [2025]. Nodal analysis of transtibial prostheses using the finite element method with Matlab. Journal Computational Simulation. 9[20] 1-10: e40920110.
https://doi.org/10.35429/JCS.2025.9.20.4.1.10

$$\nabla \cdot \sigma + f = 0 \; in \; \Omega \qquad [4]$$

where σ is the Cauchy stress tensor and f is the body force vector.

Kinematic relationships between displacement and deformation.

Where:
ε is the tensor of infinitesimal deformations and u = [u , v , w] ^{T} is the displacement vector.

Normal strains: Each normal component (εxx, εyy, εzz) corresponds to the derivative of the displacement in its own direction:

$$\mathcal{E}_{xx} = \frac{\partial u}{\partial x} \qquad [5]$$

$$\mathcal{E}_{yy} = \frac{\partial v}{\partial y} \qquad [6]$$

$$\mathcal{E}_{zz} = \frac{\partial w}{\partial z} \qquad [7]$$

A constitutive relationship can also be defined Constitutive Relationship (Generalized Hooke's Law):

$$\sigma = D\varepsilon \qquad [8]$$

where D is the elastic constitutive matrix. For an isotropic material, it depends on the modulus of elasticity E and Poisson's ratio . For a plane stress state:

$$D = \frac{E}{1-v^2}\begin{bmatrix} 1 & v & 0 \\ v & 1 & 0 \\ 0 & 0 & \frac{E}{1-v^2} \end{bmatrix} \qquad [9]$$

Boundary Conditions:
Essential (Dirichlet):

$$u = \bar{u} \text{ en } \Gamma u \qquad [10]$$

Natural (Neumann):

$$\sigma \cdot n = \bar{t} \text{ en } \Gamma t \qquad [11]$$

Finally, a nodal analysis can be performed using the finite element discretization method for each of the elements and nodes:

$$u^{(e)}(x,y,z) \approx \sum_{i=1}^{nn} Ni^{(e)}(x,y,z)u_i = N^{(e)}u^{(e)} \qquad [12]$$

where:
n_n is the number of nodes per element.
$Ni^{(e)}$ are the shape functions of the element.
u_i are the nodal displacements (unknowns).
$N^{(e)}$ is the shape function matrix.
$u^{(e)}$ is the vector of nodal displacements of the element. (Zienkiewicz, 2013)

Results

The model was designed in SolidWorks software to perform computational domain analysis, then the mesh type was created, using a fine mesh as a reference, in order to verify the polygons and the connection between them, as shown in Figure 2.

Box 2

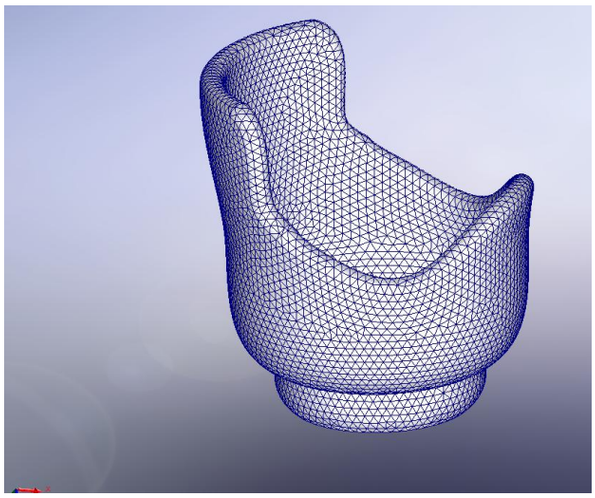

Figure 2
3D model and computer model.
Source: Own Elaboration.

Box 3

Property	Value	Units
elastic model	230-250	GPA
Poisson's ratio	0.20-0.30	N/D
shear modulus	5.0-6.0	GPA
mass density	1780	Kg/m^3
thermal conductivity	5 - 15	W/m·K

Source: Own Elaboration

Nodal analysis in SolidWorks and Matlab

Once the model was created in SolidWorks, a nodal analysis was performed, using 17,936 nodes as a reference. The file was then converted to an STL (stereolithography) extension, as shown in Figure 3.

ISSN: 2523-6865
RENIECYT-SECIHTI: 1702902

Box 3

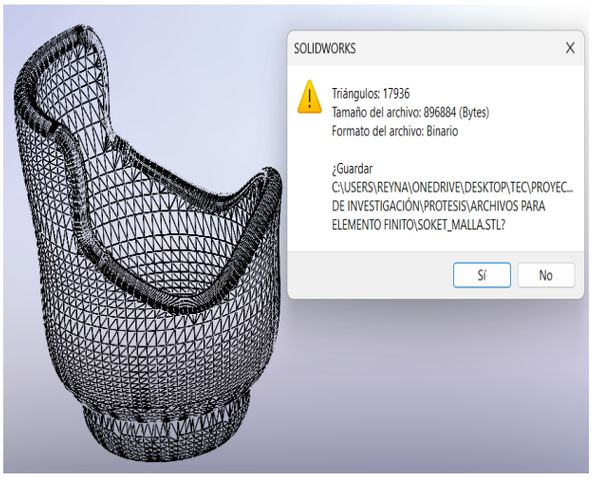

Figure 3
conversion of the STL file..
Source: Own elaboration.

For the mesh configuration, the element size values of 0.7982757cm, a minimum element size of 0.65684442cm, and a polygonal value of 8 were used, as shown in Figure 4.

Box 4

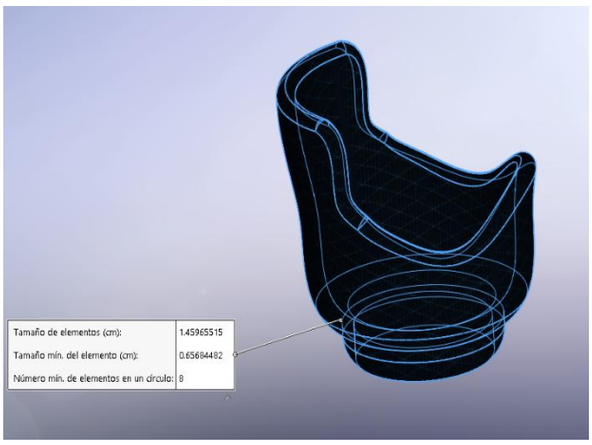

Figure 3
mesh element configuration
Source: Own Elaboration

Likewise, computational numerical domain was performed in Matalab with the same configurations of the material and the mechanical properties of the material (carbon fiber), where the command with the following nomenclature "stlread" was used (Mathwords, 2020).

This command allowed us to read the STL file generated by SolidWorks and view the mesh model in MATLAB with the same number of nodes, as shown in Figure 4.

Box 5

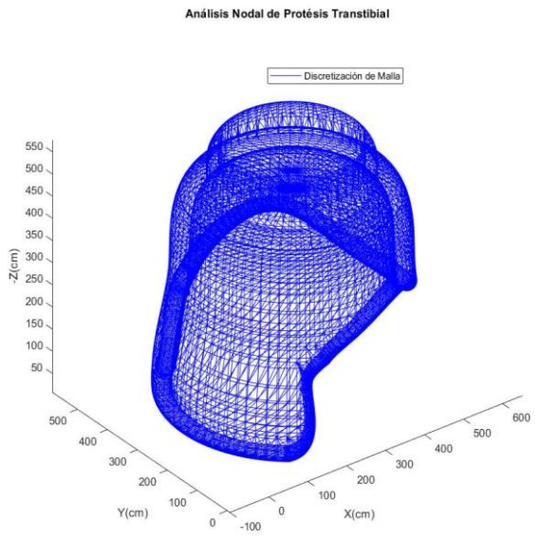

Figure 4
3D model and computer model.
Source: Own elaboration.

The graph was generated using a 3D coordinate system with X, Y, and Z axes. In the center of the graph, you can see the prosthesis model, consisting of a dense network of blue lines representing the elements of the mesh. The model was discretized using a total of 17,936 nodes, allowing for a detailed and accurate representation of the complex geometry of the prosthesis.

The mesh generated is a surface mesh with triangular elements, typical of an STL file, which facilitates its subsequent structural or dynamic analysis in MATLAB.

Therefore, a 2D analysis of the model was performed in MATLAB against SolidWorks, from which it was possible to obtain results showing that the mesh presents stable convergence in both nodes. the first in SolidWorks with that discretization of lines into polygons. Convergence is also shown in MATLAB, taking as a reference the union of each of the nodes and that there is no breakage of the polygons themselves, as shown in Figures 5 and 6.

ISSN: 2523-6865
RENIECYT-SECIHTI: 1702902

Box 6

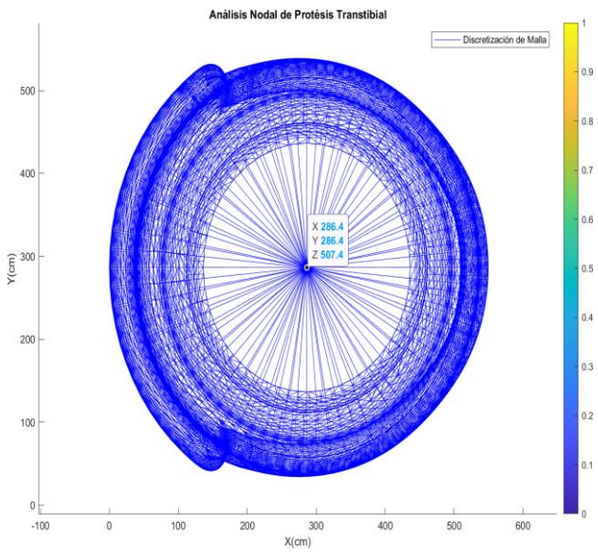

Figure 5
References for joining nodes in MATLAB with x, y, z coordinates.
Source: Own Elaboration

Box 7

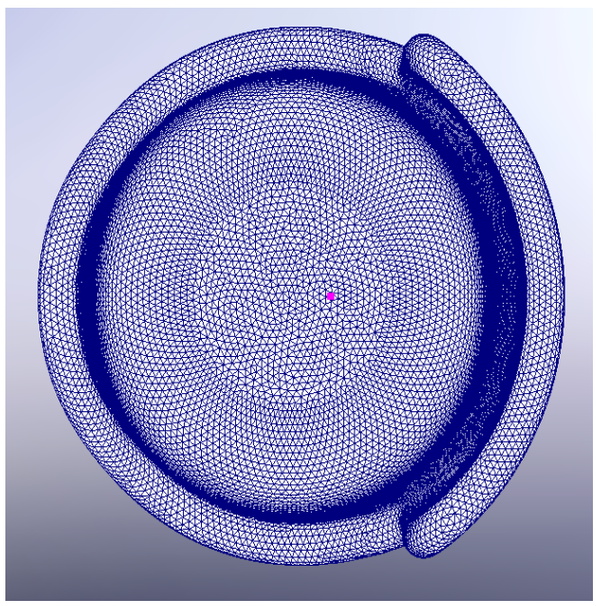

Figure 6
References for joining nodes in SolidWorks with x, y, z coordinates.
Source: Own elaboration.

Based on these results, it can be determined that a nodal analysis of a transtibial prosthesis was performed using two different approaches for the discretization of the fine mesh:

Model 2. Figure 5: Mesh generated in SolidWorks, exported as an STL file, and imported into MATLAB.

Model 1. Figure 6: Mesh generated directly in MATLAB, including a color map to visualize some nodal property (probably deformation, displacement, or distribution of modal analysis values).

Box 8

Table 2
comparison between both software programs

appearance	**model type**	*justification*
Geometric accuracy	**M**odel 1.	By using the original STL faithfully to the CAD design.
Nodal visualization.	Model 2.	Thanks to the color mapping and nodal values displayed.
Ease of analysis.	Model 2.	Already integrated into MATLAB with analysis tools.
Preparation.	Model 1.	Requires more steps (export, import, mesh conversion).
Modal interpretation.	Model 2.	llows you to visually see the most critical node.

Discussion of results

A nodal analysis of the mesh in a mechanical part (socket for transtibial prosthesis) was performed. Based on this, the transtibial prosthesis model was 3D modeled in Solidworks CAD software, taking the mechanical properties of carbon fiber as a reference. The finite element method was also used for this type of analysis, as it is one of the methods that allows the behavior of the nodes to be verified and the mesh to be visualized in wireframe mode, which allows convergence to be verified, and therefore the union of each node.

Two software programs were used as references: the first was Solidworks for 3D modeling and fine mesh generation, and the second was Matlab to transfer the stereolithography computational model to Matlab's stlread.

ISSN: 2523-6865
RENIECYT-SECIHTI: 1702902

Cortez-Solis, Reynaldo, Fuentes-Castañeda, Pilar, Betanzos-Castillo, Francisco, Jaramillo-Rodriguez, Eduardo. [2025]. Nodal analysis of transtibial prostheses using the finite element method with Matlab. Journal Computational Simulation. 9[20] 1-10: e40920110.
https://doi.org/10.35429/JCS.2025.9.20.4.1.10

In order to transfer the model to Matlab, it was necessary to program a pseudocode, which first required reading the file and then generating matrix arrays in the three dimensions x, y, and z.

Finally, the union of each node and the convergence of each line at each of the union points had to be checked, taking three nodes as a reference, in accordance with the triangular polygonal mesh type.

However, this analysis takes as a reference (Sadiq, 2025), where a study was conducted on a socket for transfemoral prostheses, whose materials (Perlon, carbon, glass, and laminating resin) can be used for future analysis in this work, since these authors have demonstrated the manufacture of different physical models, thus obtaining good results in terms of support and deformation both in software and in reality. Therefore, analyzing both results in the type of socket in this work, it can be seen that the use of these materials can be supported when physically manufacturing the proposed socket models.

Conclusions

For detailed structural analysis and geometric fidelity, the model generated from SolidWorks (Model 1) is more convenient, as it ensures that the geometry corresponds exactly to the prosthesis design. For the interpretation of nodal results and preliminary studies, the model generated directly in MATLAB (Model 2) is superior thanks to its integration with advanced visualizations, such as the color map and selection of critical nodes.

Declarations

Conflict of interest

The authors declare no interest conflict. They have no known competing financial interests or personal relationships that could have appeared to influence the article reported in this article.

Author contribution

The contribution of each of the participants in this project was significant and fundamental to the completion of this article. According to the authors, the contributions of each of them are listed below:

Cortez-Solis, Reynaldo: The contribution was the idea generated from the need of a person with limited resources to develop a transtibial prosthesis model, with the aim of creating a model for personal use with less expensive and more durable materials, 3D model design, and computational domain programming in Matlab.

Fuentes-Castañeda, Pilar: Her contribution was the analysis of the mechanical properties of the materials, as well as the mechanical analysis of the prosthesis, evaluation of different materials as a computational model, with the aim of manufacturing the physical prototype in the future and testing it correctly on the person who inspired this project.

Betanzos-Castillo, Francisco: My contribution was in the area of mathematical modeling, as well as the research and analysis of formulas related to the analysis of the mesh and behavior of each node in a matrix format, addressing a 2D computational domain.

Jaramillo-Rodriguez, Eduardo: The colleague modified and verified the 3D model.

Availability of data and materials

No data available.

Funding

The research does not currently receive funding from any external institution, as it has been supported by the National Technological Institute of Mexico, TES-Valle de Bravo, as well as personal acquisitions to carry out the project.

Acknowledgements

Special thanks to the National Technological Institute of Mexico TES-Valle de Bravo for allowing us to develop this project and for giving us access to its facilities when necessary to carry out tests or analyses related to the project.

Abbreviations

CAD Computer-Aided Design.
CAE Computer-Aided Engineering.
STL Stereolithography.
MATLAB MATLAB: Matrix Laboratory.

ISSN: 2523-6865
RENIECYT-SECIHTI: 1702902

Cortez-Solis, Reynaldo, Fuentes-Castañeda, Pilar, Betanzos-Castillo, Francisco, Jaramillo-Rodriguez, Eduardo. [2025]. Nodal analysis of transtibial prostheses using the finite element method with Matlab. Journal Computational Simulation. 9[20] 1-10: e40920110.
https://doi.org/10.35429/JCS.2025.9.20.4.1.10

References

Basics

Autodesk. (2023, 10 8). Como realizar un Estudio de Convergencia de malla.

Bermejo, P. J. (2020). Docta Ucm.

González Woge, O. G. (2020). Introducción al método del elemento finito: Solidworks y Matlab. Ideas en Ciencias de la Ingeniería, 1(1), 27-47.

Gutiérrez Madrigal, I. &. (2018, 11 26). Jóvenes en la Ciencia.

Supports

Mathwords. (20 de abril de 2020). *stlread returns different numbers of vertices/points*.

Zienkiewicz, O. C. (2013). *The Finite Element Method: Its Basis and Fundamentals*. Butterworth-Heinemann.

Vénere, M. J. (1996). Procedimientos para la generación de mallas tridimensionales de elementos finito. *Revista internacional de Métodos Numéricos para cálculo y diseno en ingenieria*, *12*(1), 3-16.

Messaad, T. B. (2025). Biomechanical analysis of prosthetic liners in transfemoral amputees using finite element. *Journal of the Brazilian Society of Mechanical Sciences and Engineering.*, *47*(2), 59.

Discussions

Sadiq, G. S. (2025). Optimal Mechanical Properties of Composite Material and Pressure Socket Analysis for Through-Knee Amputation. ELSEVIER, 28(107525).

ISSN: 2523-6865
RENIECYT-SECIHTI: 1702902

Cortez-Solis, Reynaldo, Fuentes-Castañeda, Pilar, Betanzos-Castillo, Francisco, Jaramillo-Rodriguez, Eduardo. [2025]. Nodal analysis of transtibial prostheses using the finite element method with Matlab. Journal Computational Simulation. 9[20] 1-10: e40920110.
https://doi.org/10.35429/JCS.2025.9.20.4.1.10

[[Title in TNRoman and Bold No. 14 in English and Spanish]

Surname, Name 1st Author*[a], Surname, Name 1st Co-author[b], Surname, Name 2nd Co-author[c] and Surname, Name 3rd Co-author[d] [No.12 TNRoman]

[a] Affiliation institution, Researcher ID, ORC ID, SNI-SECIHTI ID or CVU PNPC [No.10 TNRoman]
[b] Affiliation institution, Researcher ID, ORC ID, SNI-SECIHTI ID or CVU PNPC [No.10 TNRoman]
[c] Affiliation institution, Researcher ID, ORC ID, SNI-SECIHTI ID or CVU PNPC [No.10 TNRoman]
[d] Affiliation institution, Researcher ID, ORC ID, SNI-SECIHTI ID or CVU PNPC [No.10 TNRoman]

All ROR-Clarivate-ORCID and SECIHTI profiles must be hyperlinked to your website.
Prot- University of South Australia • 7038-2013• 0000-0001-6442-4409 • 416112

SECIHTI classification:
https://marvid.org/research_areas.php [No.10 TNRoman]
Area:
Field:
Discipline:
Subdiscipline:

DOI: https://doi.org/
Article History:
Received: [Use Only ECORFAN]
Accepted: [Use Only ECORFAN]
Contact e-mail address:
* ✉ [example@example.org]

Abstract [In English]
Must contain up to 150 words
Graphical abstract [In English]

Authors must provide an original image that clearly represents the article described in the article. Graphical abstracts should be submitted as a separate file. Please note that, as well as each article must be unique. File type: the file types are MS Office files.No additional text, outline or synopsis should be included. Any text or captions must be part of the image file. Do not use unnecessary white space or a "graphic abstract" header within the image file.

Keywords [In English]
Indicate 3 keywords in TNRoman and Bold No. 10

Abstract [In Spanish]
Must contain up to 150 words
Graphical abstract [In Spanish]

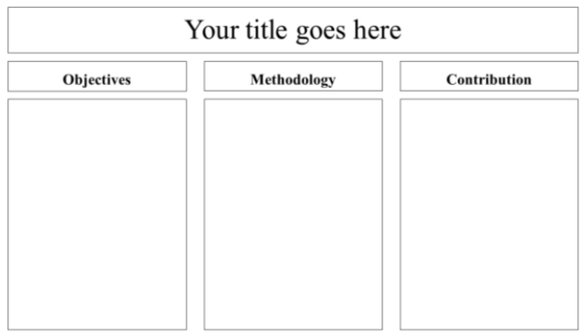

Authors must provide an original image that clearly represents the article described in the article. Graphical abstracts should be submitted as a separate file. Please note that, as well as each article must be unique. File type: the file types are MS Office files.No additional text, outline or synopsis should be included. Any text or captions must be part of the image file. Do not use unnecessary white space or a "graphic abstract" header within the image file.

Keywords [In Spanish]
Indicate 3 keywords in TNRoman and Bold No. 10

Citation: Surname, Name 1st Author, Surname, Name 1st Co-author, Surname, Name 2nd Co-author and Surname, Name 3rd Co-author. Article Title. Journal Computational Simulation. Year. V-N: Pages [TN Roman No.10].

Introduction

Text in TNRoman No.12, single space.

General explanation of the subject and explain why it is important.

What is your added value with respect to other techniques?

Clearly focus each of its features.

Clearly explain the problem to be solved and the central hypothesis.

Explanation of sections Article.

Development of headings and subheadings of the article with subsequent numbers

[Title No.12 in TNRoman, single spaced and bold]

Products in development No.12 TNRoman, single spaced.

Including figures and tables-Editable

In the article content any table and figure should be editable formats that can change size, type and number of letter, for the purposes of edition, these must be high quality, not pixelated and should be noticeable even reducing image scale.

[Indicating the title at the bottom with No.10 and Times New Roman Bold]

Box

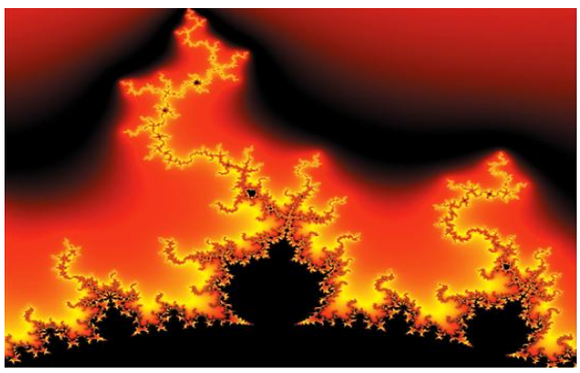

Figure 1

Title [Should not be images-everything must be editable]

Source [in italic]

Box

Table 1

Title [Should not be images-everything must be editable]

Source [in italic]

The maximum number of Boxes is 10 items

For the use of equations, noted as follows:

$$Y_{ij} = \alpha + \sum_{h=1}^{r} \beta_h X_{hij} + u_j + e_{ij} \quad [1]$$

Must be editable and number aligned on the right side.

Methodology

Develop give the meaning of the variables in linear writing and important is the comparison of the used criteria.

Results

The results shall be by section of the article.

Conclusions

Clearly explain the results and possibilities of improvement.

Annexes

Tables and adequate sources.

The international standard is 7 pages minimum and 14 pages maximum.

Declarations

Conflict of interest

The authors declare no interest conflict. They have no known competing financial interests or personal relationships that could have appeared to influence the article reported in this article.

ISSN: 2523-6865
RENIECYT-SECIHTI: 1702902

Surname, Name 1st Author, Surname, Name 1st Co-author, Surname, Name 2nd Co-author and Surname, Name 3rd Co-author. Article Title. Journal Computational Simulation. Year. V-N: Pages [Times New Roman No. 8].
https://doi.org/10.35429/

Author contribution

Specify the contribution of each researcher in each of the points developed in this research.

Prot-
Benoit-Pauleter, Gerard: Contributed to the project idea, research method and technique.

Availability of data and materials

Indicate the availability of the data obtained in this research.

Funding

Indicate if the research received some financing.

Acknowledgements

Indicate if they were financed by any institution, University or company.

Abbreviations

List abbreviations in alphabetical order.

Prot-

ANN	Artificial Neural Network

References

Use APA system. Should not be numbered, nor with bullets, however if necessary numbering will be because reference or mention is made somewhere in the Article.

Use the Roman alphabet, all references you have used should be in Roman alphabet, even if you have cited an article, book in any of the official languages of the United Nations [English, French, German, Chinese, Russian, Portuguese, Italian, Spanish, Arabic], you should write the reference in Roman alphabet and not in any of the official languages.

Citations are classified the following categories:

Antecedents. The citation is due to previously published research and orients the citing document within a particular scholarly area.

Basics. The citation is intended to report data sets, methods, concepts and ideas on which the authors of the citing document base their work.

Supports. The citing article reports similar results. It may also refer to similarities in methodology or, in some cases, to the reproduction of results.

Differences. The citing document reports by means of a citation that it has obtained different results to those obtained in the cited document. This may also refer to differences in methodology or differences in sample sizes that affect the results.

Discussions. The citing article cites another study because it is providing a more detailed discussion of the subject matter.

The URL of the resource is activated in the DOI or in the title of the resource.

Prot-
Mandelbrot, B. B. [2020]. Negative dimensions and Hölders, multifractals and their Hölder spectra, and the role of lateral preasymptotics in science. Journal of Fourier Analysis and Applications Special. 409-432.

Intellectual Property Requirements for editing:

– Authentic Signature in Color of Originality Format Author and Coauthors.

– Authentic Signature in Color of the Acceptance Format of Author and Coauthors.

– Authentic Signature in blue color of the Conflict of Interest Format of Author and Co-author

ISSN: 2523-6865
RENIECYT-SECIHTI: 1702902

Reservation to Editorial Policy

Journal Computational Simulation reserves the right to make editorial changes required to adapt the Articles to the Editorial Policy of the Research Journal. Once the Article is accepted in its final version, the Research Journal will send the author the proofs for review. ECORFAN® will only accept the correction of errata and errors or omissions arising from the editing process of the Research Journal, reserving in full the copyrights and content dissemination. No deletions, substitutions or additions that alter the formation of the Article will be accepted.

Code of Ethics - Good Practices and Declaration of Solution to Editorial Conflicts

Declaration of Originality and unpublished character of the Article, of Authors, on the obtaining of data and interpretation of results, Acknowledgments, Conflict of interests, Assignment of rights and Distribution.

The ECORFAN-Mexico, S.C Management claims to Authors of Articles that its content must be original, unpublished and of Scientific, Technological and Innovation content to be submitted for evaluation.

The Authors signing the Article must be the same that have contributed to its conception, realization and development, as well as obtaining the data, interpreting the results, drafting and reviewing it. The Corresponding Author of the proposed Article will request the form that follows.

Article title:

– The sending of an Article to Journal Computational Simulation emanates the commitment of the author not to submit it simultaneously to the consideration of other series publications for it must complement the Format of Originality for its Article, unless it is rejected by the Arbitration Committee, it may be withdrawn.

– None of the data presented in this article has been plagiarized or invented. The original data are clearly distinguished from those already published. And it is known of the test in PLAGSCAN if a level of plagiarism is detected Positive will not proceed to arbitrate.

– References are cited on which the information contained in the Article is based, as well as theories and data from other previously published Articles.

– The authors sign the Format of Authorization for their Article to be disseminated by means that ECORFAN-Mexico, S.C. In its Holding Taiwan considers pertinent for disclosure and diffusion of its Article its Rights of Work.

– Consent has been obtained from those who have contributed unpublished data obtained through verbal or written communication, and such communication and Authorship are adequately identified.

– The Author and Co-Authors who sign this work have participated in its planning, design and execution, as well as in the interpretation of the results. They also critically reviewed the paper, approved its final version and agreed with its publication.

– No signature responsible for the work has been omitted and the criteria of Scientific Authorization are satisfied.

– The results of this Article have been interpreted objectively. Any results contrary to the point of view of those who sign are exposed and discussed in the Article.

Copyright and Access

The publication of this Article supposes the transfer of the copyright to ECORFAN-Mexico, S.C. in its Holding Taiwan for its Journal Computational Simulation, which reserves the right to distribute on the Web the published version of the Article and the making available of the Article in This format supposes for its Authors the fulfilment of what is established in the Law of Science and Technology of the United Mexican States, regarding the obligation to allow access to the results of Scientific Research.

Article Title:

Name and Surnames of the Contact Author and the Co-authors	Signature
1.	
2.	
3.	
4.	

Principles of Ethics and Declaration of Solution to Editorial Conflicts

Editor Responsibilities

The Publisher undertakes to guarantee the confidentiality of the evaluation process, it may not disclose to the Arbitrators the identity of the Authors, nor may it reveal the identity of the Arbitrators at any time.

The Editor assumes the responsibility to properly inform the Author of the stage of the editorial process in which the text is sent, as well as the resolutions of Double-Blind Review.

The Editor should evaluate manuscripts and their intellectual content without distinction of race, gender, sexual orientation, religious beliefs, ethnicity, nationality, or the political philosophy of the Authors.

The Editor and his editing team of ECORFAN® Holdings will not disclose any information about Articles submitted to anyone other than the corresponding Author.

The Editor should make fair and impartial decisions and ensure a fair Double-Blind Review.

Responsibilities of the Editorial Board

The description of the peer review processes is made known by the Editorial Board in order that the Authors know what the evaluation criteria are and will always be willing to justify any controversy in the evaluation process. In case of Plagiarism Detection to the Article the Committee notifies the Authors for Violation to the Right of Scientific, Technological and Innovation Authorization.

Responsibilities of the Arbitration Committee

The Arbitrators undertake to notify about any unethical conduct by the Authors and to indicate all the information that may be reason to reject the publication of the Articles. In addition, they must undertake to keep confidential information related to the Articles they evaluate.

Any manuscript received for your arbitration must be treated as confidential, should not be displayed or discussed with other experts, except with the permission of the Editor.

The Arbitrators must be conducted objectively, any personal criticism of the Author is inappropriate.

The Arbitrators must express their points of view with clarity and with valid arguments that contribute to the Scientific, Technological and Innovation of the Author.

The Arbitrators should not evaluate manuscripts in which they have conflicts of interest and have been notified to the Editor before submitting the Article for Double-Blind Review.

Responsibilities of the Authors

Authors must guarantee that their articles are the product of their original work and that the data has been obtained ethically.

Authors must ensure that they have not been previously published or that they are not considered in another serial publication.

Authors must strictly follow the rules for the publication of Defined Articles by the Editorial Board.

The authors have requested that the text in all its forms be an unethical editorial behavior and is unacceptable, consequently, any manuscript that incurs in plagiarism is eliminated and not considered for publication.

Authors should cite publications that have been influential in the nature of the Article submitted to arbitration.

Information services

Indexation - Bases and Repositories

RESEARCH GATE (Germany)
GOOGLE SCHOLAR (Citation indices-Google)
MENDELEY (Bibliographic References Manager)
REDIB (Ibero-American Network of Innovation and Scientific Knowledge- CSIC)
HISPANA (Information and Bibliographic Orientation-Spain)

Publishing Services

Citation and Index Identification H
Management of Originality Format and Authorization
Testing Article with PLAGSCAN
Article Evaluation
Certificate of Double-Blind Review
Article Edition
Web layout
Indexing and Repository
ArticleTranslation
Article Publication
Certificate of Article
Service Billing

Editorial Policy and Management

69 Street. YongHe district, ZhongXin. Taipei-Taiwan. Phones: +52 1 55 6159 2296, +52 1 55 1260 0355, +52 1 55 6034 9181; Email: contact@ecorfan.org www.ecorfan.org

Journal Computational Simulation

2523 6865
ISSN 2523-6865

www.ecorfan.org